

MEASUREMENT OF INTERACTION FORCES BETWEEN  
MICROMETER-SIZED PARTICLES AND FLAT SURFACES USING AN  
ATOMIC FORCE MICROSCOPE

A Thesis

Submitted to the Faculty

of

Purdue University

by

Barrett Lee Gady

In Partial Fulfillment of the  
Requirements for the Degree

of

Doctor of Philosophy

August, 1996

This thesis is dedicated to my mother and father, and to my wife Wendy.

## ACKNOWLEDGMENTS

I would like to thank Professor Ron Reifenberger for his willingness to support my Ph.D research. In particular, I would like to thank him for the many insightful suggestions and the tacit knowledge which cannot be obtained through course work.

Special thanks also goes to Dr. Donald Rimai at Eastman Kodak for many helpful discussions regarding my research.

I would also like to thank Dr. David Schaefer for constructing the AFM used in performing my research. My colleagues Daniel Lovall and Seunghun Hong have provided a great deal of assistance through innumerable discussions. I am especially thankful to David Schleef who wrote some of the code used for analyzing the data.

I cannot overlook the mentors early on in my career, Dr. Alan Krauss and Dr. Dieter M. Gruen at Argonne National Laboratory. The experience I gained through research in their group has proven to be invaluable in my overall knowledge of experimental physics.

Finally, I would like to thank all of my family for their support during these studies. In particular I would like to acknowledge my wife Wendy for her support

and encouragement. She has taken on tremendous sacrifices and I will always be indebted to her for the unwavering commitment to our relationship through these difficult times.

This work was funded by the Division of Office Imaging Research and Development at Eastman Kodak.

## TABLE OF CONTENTS

	Page
LIST OF TABLES . . . . .	vii
LIST OF FIGURES . . . . .	ix
ABSTRACT . . . . .	xv
1. INTRODUCTION . . . . .	1
1.1 Introduction . . . . .	1
2. Long-Range Interaction Forces . . . . .	6
2.1 Van der Waals and Dispersion Forces . . . . .	6
2.1.1 Microscopic Model . . . . .	11
2.1.2 Macroscopic Model . . . . .	13
2.2 Electrostatic Interaction Model . . . . .	19
3. Principles of the Atomic Force Microscope . . . . .	31
3.1 Apparatus Design . . . . .	31
3.2 Lever Mechanics . . . . .	36
3.2.1 Cantilevers . . . . .	36
3.2.2 Force Detection . . . . .	39
3.2.3 Modeling a Forced Oscillating Lever . . . . .	48
4. Experimental . . . . .	54
4.1 Material Properties . . . . .	54
4.1.1 Electronic and Physical Properties of Polystyrene . . . . .	54
4.1.2 Electronic and Physical Properties of Highly-Oriented Py- rolytic Graphite . . . . .	59
4.2 Calibrating AFM Cantilevers . . . . .	64
4.3 Mounting micron spheres to cantilevers . . . . .	66
4.4 Force Measurement Technique . . . . .	69
4.5 Force Gradient Measurement Technique . . . . .	71
5. Measured Interaction between Polystyrene Spheres and HOPG Substrate	77
5.1 Theoretical Considerations . . . . .	77

	Page
5.2 Interaction Force Gradient vs. Sphere Radius . . . . .	83
5.3 Force and Force Gradient-Consistency Check . . . . .	88
5.4 Methanol Treatment-Charge Passivation . . . . .	89
5.5 Summary . . . . .	91
6. Contact Electrification . . . . .	100
6.1 Contact Electrification . . . . .	100
6.1.1 Metal-Metal Interactions . . . . .	105
6.1.2 Metal-Insulator Interactions . . . . .	108
6.1.3 Insulator-Insulator Interactions . . . . .	110
6.2 Charge Transfer Models . . . . .	110
6.2.1 Electronic Charge Transfer . . . . .	112
6.2.2 Ionic Charge Transfer . . . . .	118
6.2.3 Material Charge Transfer . . . . .	119
6.3 Charge Transfer Experiments . . . . .	120
7. Summary . . . . .	132
BIBLIOGRAPHY . . . . .	135
APPENDICES	
Appendix A: A sample of the C code which calculates the resonant frequency peak of the cantilever. . . . .	140
Appendix B: Subroutine for collecting frequency spectra. . . . .	144
Appendix C: Analysis code written in IDL. . . . .	147
VITA . . . . .	153

## LIST OF TABLES

Table	Page
2.1 Van der Waals interaction forces for various geometries as calculated using a microscopic model. . . . .	12
2.2 Macroscopic Lifshitz model used to calculate non-retarded van der Waals forces. [a] $\theta$ corresponds to the half-angle aperture of the cone.	18
2.3 Non-Retarded Hamaker Coefficients for two similar materials interacting across a vacuum. . . . .	20
2.4 Non-Retarded Hamaker Coefficients for two dissimilar materials interacting across a vacuum. . . . .	22
2.5 Parameters for both uniform and localized charge distributions. . .	22
2.6 Parameters for both uniform and localized charge distributions. . .	28
3.1 A comparison between two methods for calculating the spring constant of a cantilever. . . . .	40
3.2 Spring constants for typical cantilevers used in experiments as calculated using resonance frequency method. . . . .	40
3.3 Calculated and measured values for the jump to contact distance for a distribution of polystyrene spheres interacting with a HOPG substrate. . . . .	49
4.1 Physical and Electrical properties of Polystyrene. . . . .	55
4.2 Force of removal reference measurements between a 9 $\mu\text{m}$ polystyrene sphere and freshly cleaved HOPG surface. . . . .	63
5.1 Force gradient parameters for 3 $\mu\text{m}$ radius polystyrene sphere interacting with freshly cleaved HOPG surface. . . . .	86

Table	Page
5.2 Force gradient parameters for 6 $\mu\text{m}$ radius polystyrene sphere interacting with freshly cleaved HOPG surface. . . . .	87
5.3 Parameters for fitting data for the As-prepared polystyrene sphere.	90
5.4 Parameters for the Methanol treated polystyrene sphere. . . . .	92
6.1 Summary of the parameters used in fitting contact electrification data to model. . . . .	126

## LIST OF FIGURES

Figure		Page
2.1	Contributions to the van der Waals interaction. . . . .	7
2.2	Classical model for the dispersion interaction . . . . .	8
2.3	Macroscopic model for van der Waals interaction. . . . .	17
2.4	Electrostatic interaction due to contact electrification . . . . .	21
2.5	Contributions to the Interaction. . . . .	24
2.6	Electrostatic interaction due contact electrification . . . . .	26
2.7	Uniform charge distribution as a function of sphere radius. The charge density $\sigma$ remains fixed, while the radius ( $R = 3 \mu\text{m}$ ) is changed. . . . .	27
2.8	Localized charge distribution as a function of the effective region of contact. The charge density $\sigma$ of the charged patch region remains fixed, while $R_{eff} = 50 \text{ nm}$ is changed. . . . .	27
2.9	Interaction forces as a function of sphere size at a fixed separation of 2 nm. Interactions shown are van der Waals (solid line), localized electrostatic (dashed line), uniform electrostatic (dotted). . . . .	29
2.10	Interaction forces as a function of sphere size at a fixed separation of 5 nm. Interactions shown are van der Waals (solid line), localized electrostatic (dashed line), uniform electrostatic (dotted). . . . .	29
2.11	Interaction forces as a function of sphere size at a fixed separation of 10 nm. Interactions shown are van der Waals (solid line), localized electrostatic (dashed line), uniform electrostatic (dotted). . . . .	30
3.1	Atomic Force Microscope Design . . . . .	32

Figure	Page
3.2 AFM is enclosed in a UHV chamber capable of pumping down to a moderate vacuum. . . . .	34
3.3 Diagram illustrating the humidity sensor mounting in the chamber.	34
3.4 Circuit schematic for the humidity sensor. . . . .	35
3.5 Frequency to voltage converter circuit. . . . .	35
3.6 Humidity sensor calibration. . . . .	36
3.7 Typical cantilever geometry. . . . .	37
3.8 Deflection of cantilever due to tip-substrate interaction. . . . .	41
3.9 Variation of the cantilever deflection due to an attractive interaction force. The solid lines are the net interaction for varying spring stiffness. The spring constants are 0.2, 1.1, and 2.2 N/m. The interaction is due to a van der Waals and localized electrostatic force between a 3 $\mu\text{m}$ sphere and grounded plane (dashed line). The charge density is $\sim 10^{-4} \frac{\text{C}}{\text{m}^2}$ localized in a $\sim 100$ nm region. The equilibrium position with no forces present is 80 nm. The points marked by diamonds indicate the new equilibrium position for each spring in the presense of the force. . . . .	43
3.10 Jump to contact phenomenon. . . . .	44
3.11 The net interaction(solid lines) is a combination of the attractive interaction force (dashed line) and the spring restoring force. As the separation distance between the sphere and sample decreases, the net interaction force changes. The points indicated by diamonds show how the equilibrium position changes due to the interaction force as the tip-surface separation distance changes. The point indicated by the square shows where the equilibrium position is unstable and the jump to contact occurs. . . . .	45

Figure	Page
3.12 Jump to contact data (square) is plotted as a function of sphere radius. A comparison is made between the influence of a purely van der Waals (solid lines) and a van der Waals-Electrostatic (dashed line) interaction. Two van der Waals curves are shown to indicate the range in Hamaker values observed in our measurements. The parameters for the combined interaction curve are: $Q = 500$ electrons, $R_{\text{eff}} = a_{\text{JKR}}$ , and $H = 0.6$ eV. . . . .	50
3.13 Force curve measurement exhibiting a purely van der Waals interaction. The sphere radius is $3 \mu\text{m}$ and the spring constant is $2.1 \frac{\text{N}}{\text{m}}$ . . . . .	51
3.14 Force curve measurement exhibiting both van der Waals and electrostatic contributions. The sphere radius is $3 \mu\text{m}$ and the spring constant is $2.1 \frac{\text{N}}{\text{m}}$ . . . . .	51
4.1 Chemical Structure of Polystyrene. . . . .	55
4.2 Surface roughness effects of polystyrene spheres. . . . .	57
4.3 Donor-Acceptor levels in Insulators. . . . .	58
4.4 Three dimensional structure of highly oriented pyrolytic graphite. The interplanar spacing $d_o$ is $0.33538$ nm. The spacing between carbon atoms, $a_o$ is $0.1415$ nm. . . . .	61
4.5 Brillouin zone for three dimensional crystalline graphite. . . . .	61
4.6 Control Measurements on HOPG . . . . .	62
4.7 Procedure for performing resonance frequency measurement. . . . .	65
4.8 Voltage calibration. . . . .	66
4.9 The capillary pipettes are extruded to sub-micrometer tips in order to both apply glue, as well as to mount small particles. . . . .	74
4.10 Micromanipulator set-up used to perform sphere mounting. . . . .	75

Figure	Page
4.11 The process is as follows: a) Selection of sphere; b) Focus on cantilever to which sphere is to be mounted to; c) Bring sphere into range of the cantilever; d) Placement of sphere onto cantilever; e) Withdraw capillary whisker; f) Check the placement of sphere on cantilever. . . . .	76
5.1 The relevant parameters to describe triboelectric charging of the polystyrene sphere upon contact and removal from an atomically flat HOPG substrate. In (a) a sphere of radius $R$ approaches the HOPG substrate. Upon contact (b) the sphere deforms due to surface forces between the sphere and substrate, which cause a contact area to form with radius $a_o$ . While in contact, charge transfer between the grounded substrate and the sphere takes place. After separation (c), the excess charge remains localized at the bottom of the sphere over a region with radius $R_{\text{eff}} \simeq a_o$ . . . . .	80
5.2 Plots of the spatial dependence of the interaction force and interaction force gradient. In (a) and (b), the dashed line indicates the contribution of a van der Waals interaction alone. The other lines illustrate electrostatic contributions to the net interactions from either a uniform (dotted line) or localized (solid line) charge distribution. In (c) and (d), logarithmic plots of force and force gradients for a pure van der Waals interaction (dashed line), and for electrostatic contributions from either a uniform (dotted line) or localized (solid line) charge distribution. The plots emphasize the nature of the electrostatic contribution to the net interaction. The region enclosed by the dotted box shown in both plots indicates the experimental limit of our instrument. Regions labeled I and II separate the non-retarded and retarded limits of the van der Waals interaction. The absorption wavelength of polystyrene is given by $\chi$ . The parameters used in generating the plots are: $R = 3 \mu\text{m}$ ; $R_{\text{eff}} = 57 \text{ nm}$ ; $Q = 500$ electrons; and $H = 0.6 \text{ eV}$ . . . . .	84
5.3 The amplitude of the cantilever oscillation is given for two different values of $z_o$ . The solid lines are a best fit to the data using Eqn. 3.26. . . . .	95

Figure	Page
5.4 Data measuring the force gradient of the interaction force between a polystyrene sphere and an atomically flat HOPG substrate. In (a), a plot of $\log_{10} \left[ k \left( 1 - \left( \frac{\omega_o(z_o)}{\omega_\infty} \right)^2 \right) \right]$ vs $\log_{10} z_o$ for a 3 $\mu\text{m}$ radius sphere. The dashed line (see Table 1) is a fit to the experimental data. In (b), a plot of $\log_{10} \left[ k \left( 1 - \left( \frac{\omega_o(z_o)}{\omega_\infty} \right)^2 \right) \right]$ vs $\log_{10} z_o$ for a 6 $\mu\text{m}$ radius sphere. The dashed line (see Table 2) is a fit to the experimental data. . . . .	96
5.5 Data from a static force measurement (a) and a dynamic force gradient measurement (b) of a 3 $\mu\text{m}$ radius polystyrene sphere as a function of surface-to-surface separation from a flat HOPG substrate. The data is typical for an as-prepared sphere. The fits to the data are shown by the solid lines. The dashed line shows the contribution for a pure van der Waals interaction. The fitting parameters are summarized in Table 5.3. . . . .	97
5.6 Experimental procedure for measuring the interactions between the polystyrene sphere and HOPG substrate. . . . .	98
5.7 Typical data for the force (a) and force gradient (b) acting on a 3 $\mu\text{m}$ radius methanol-treated polystyrene sphere as a function of surface-to-surface separation from a flat HOPG substrate. The fits to the data for the methanol-treated sphere are shown by the solid lines. The dashed line indicates the contribution due to a pure van der Waals interaction. The dotted line represents the fit to the as-prepared polystyrene sphere. The fitting parameters are summarized in Table 5.4. . . . .	99
6.1 Maximum electric field under atmospheric conditions before Paschen breakdown occurs. . . . .	104
6.2 Maximum surface charge density under atmospheric conditions before Paschen breakdown occurs. . . . .	104
6.3 Energy level diagram for a metal-metal contact. . . . .	107
6.4 Energy level diagram for a metal-insulator contact. . . . .	109
6.5 Energy level diagram for an insulator-insulator contact. . . . .	111

Figure	Page
6.6 Electron transfer model for metal-insulator interaction assuming there is only one energy level for the acceptor states. . . . .	116
6.7 Localized states within the insulator which are initially below the Fermi level. The equilibrium condition causes band bending to occur resulting in excess charge in acceptor states. . . . .	116
6.8 Material transfer after sphere contacted a compliant substrate. . . .	120
6.9 The transfer of material may be detected from variations observed in the loading force curve . . . . .	125
6.10 Schematic illustration of the electron transfer model. Polystyrene has acceptor states which are accessible to electrons from HOPG near the Fermi level. The Fermi level for Au[111] is below the states in polystyrene and electrons cannot be transferred. . . . .	125
6.11 Representative plots of the measured force acting between a 5 $\mu\text{m}$ radius polystyrene sphere mounted on a cantilever and (a) a HOPG substrate and (b) a Au[111] substrate. The data were taken upon approach after the sphere was touched to a particular substrate and withdrawn. The long-range interaction observed after touching the HOPG substrate is consistent with the an electrostatic force produced by charges localized at the bottom of the polystyrene sphere. For the Au[111] substrate, a careful analysis of the force gradient data just before jump to contact indicates a van der Waals interaction is the dominant contribution to the net interaction force. Note the change in scale of the abscissa between the two sets of data. . . .	127
6.12 Contact electrification is observed for interactions between polystyrene and HOPG. Charge increases linearly with number of contacts between the sphere and substrate. Results for contact charging are shown for a 3 $\mu\text{m}$ (triangles) and 5 $\mu\text{m}$ (diamonds) radius polystyrene spheres. The rates at which charge increases are 2 electrons/contact and 14 electrons/contact. . . . .	129

## ABSTRACT

Gady, Barrett Lee. Ph.D., Purdue University, August, 1996. Measurement of the Interaction Forces between Micrometer-Sized Particles and Flat Surfaces using an Atomic Force Microscope. Major Professor: Ron Reifenberger.

The Atomic Force Microscope is used to directly measure the interaction forces between micrometer-sized spheres and atomically flat substrates. In particular, the interaction between micrometer-sized polystyrene spheres and highly oriented pyrolytic graphite is measured. The study provides important information about the relative contributions to the net interaction due to both van der Waals and electrostatic forces. The two techniques used are unique to scanning force microscopy. One method, referred to as the static mode of operation, is used to directly measure the interaction force as a function of surface to surface separation. The second method, referred to as the dynamic mode of operation, provides information about the force gradient. The information provided by these two methods is found to be consistent. The variation of the interaction force with the surface-to-surface separation between the sphere and plane is determined using both a static and a dynamic atomic force technique. The measured interactions is dominated at long-range by an electrostatic force arising from localized charges triboelectrically

produced on the sphere when it makes contact with the substrate. For small sphere-substrate separations, evidence for a van der Waals contribution to the interaction is observed. The data provide consistent estimates for both the Hamaker coefficient and the triboelectrically produced charge which can be measured to an accuracy of  $\pm 10$  electron charges.

## 1. INTRODUCTION

### 1.1 Introduction

Prior to the development of atomic force microscopy (AFM), a great deal of work had been done to model the interaction between macroscopic objects due to long-range van der Waals and electrostatic forces. [1, 2, 3] An AFM is basically a probe used to image features of a surface down to an atomic scale. The AFM is comprised of a flexible cantilever arm with a sharp tip. As this tip comes into close proximity to a surface, the arm will deflect due to interaction forces. The deflection experienced can be used as a feedback mechanism to map out features of the surface. This device has only been made available with the development of nanometer-scale resolution provided by piezo-electric materials.

The rapid development of the AFM has produced techniques capable of measuring nanonewton forces acting on a sharp tip as it approaches a substrate. Under normal circumstances, it is generally assumed that the attractive force between the tip and substrate is governed by the van der Waals interaction. Quantitative measurements of the interaction force between a sharp tip and flat substrate are inherently difficult to interpret because the exact geometry of the tip is often not known. Various attempts to directly measure the spatial dependence of the at-

tractive force between a tip and substrate have produced data that requires an action over a considerably greater range than expected if van der Waals forces are dominant. The appearance of this long-range force is often attributed to capillary effects due to unwanted contaminants. Recently, Burnham *et al.*[4] demonstrated that force measurements taken with a static cantilever approaching a surface can be fitted using a complicated electrostatic patch charge effect, providing an insight into the origin of the long-range force. Indeed, early attempts to study the van der Waals force between extended objects with dimensions greater than those considered here have emphasized the need to eliminate electrostatic forces.[5, 6, 7]

There is a tremendous amount of interest in a variety of fields to measure the interaction between microscopic spherical particles. Information regarding surface adhesion and chemical reactions are important in fields ranging from biochemistry to electrophotography. Because of the operational range of the AFM, it makes an ideal instrument for studying these macroscopic interactions to determine the actual contributions due to these interaction forces. Ignoring any contributions due to capillary forces, the interaction between an AFM probe and sample are composed of two independent contributions. At long range, (greater than a 10 nanometers) van der Waals and electrostatic forces are dominant. At short range (less than 1 nanometer), the interaction force becomes repulsive. The standard AFM modes of operation, contact and non-contact, exploit each of these regimes when imaging surfaces. In order to further understand how the AFM works, it is necessary to investigate the interactions between the probe and the sample. By

exploiting the ability of the AFM to measure force gradients in non-contact mode, a further understanding of the interaction between small particles will be obtained.

There are two basic models which describe the interactions between macroscopic objects due to long range van der Waals forces. The first, and most simplistic, is the microscopic model. This approach was initially discussed by researchers such as Derjaguin and Hamaker.[8, 1] It is based on a summation over the atomistic pair potentials of the two objects. Calculations for well-known geometries have already been tabulated for both non-retarded and retarded regimes.[9] Because the van der Waals interactions are mainly due to dispersive interactions, a simple pairwise additivity approach was determined to be insufficient. This classical approach completely ignores the radiation effects of nearest neighbor atoms.

Lifshitz developed a macroscopic model which avoids the problem of the non-additivity of the dispersion forces. With Lifshitz's approach it is only necessary to know properties such as the dielectric constants and permittivities for the materials. Later models improved on Lifshitz's original work, but the power-law dependencies for each geometrical configuration remained the same.[10, 11] The major difference between these classical and quantum mechanical models is the way in which Hamaker constants are calculated. Remarkably, the overall power-law dependence is identical regardless of which model is used.

Although there are a variety of models which discuss the interaction of macroscopic objects of various geometries, there are only a few experimental techniques for measuring these forces. The major difficulty in performing measurements is the

range over which van der Waals forces act ( $\sim 10^{-9}$  m) and their magnitude ( $\sim 10^{-9}$  N). The earliest experimental work was done by Derjaguin, and later by others such as Israelchivili and Tabor using a Surface Force Apparatus (SFA).[12, 13] Both found that their experimental results were consistent with the Hamaker and Lifshitz models, respectively. In both cases, however, the measurements are restricted to a crossed cylinder geometry.

The development of the atomic force microscope has opened another avenue for measuring long range interactions between a probe and surface. The AFM has already demonstrated versatility and flexibility with its range of operation. It has the capability of sub-nanometer resolution and sensitivity down to  $\sim 10^{-12}$  N. By using a simple oscillator model for the probe near a flat surface and assuming a purely van der Waals interaction, various researchers have demonstrated the AFM can be used to measure long range interactions.[14] This is the basic principle behind non-contact mode scanning. Also, by measuring shifts in the resonance frequency with displacement from a surface, the force gradient between the probe and surface can be measured. With this sensitivity to long range forces, it is possible to measure interactions for a variety of probe and surface geometry combinations. In this discussion, we consider a lever with a polystyrene sphere attached. The surface used in this study was highly oriented pyrolytic graphite (HOPG). According to both Hamaker and Lifshitz models the interaction force, and therefore the force gradient, will be governed by a unique power law.

Because the spheres are made of a dielectric material, the susceptibility to

triboelectric charging must also be accounted for by assuming an additional electrostatic force. In fact, it is not possible to measure pure van der Waals forces between micrometer sized polystyrene spheres and the highly oriented pyrolytic graphite (HOPG) surface because electrostatic effects dominate much of the interaction. The only way to fully understand the interaction forces which exist is to exploit both AFM measurement techniques.

The problem of electrostatic charge on materials is a pervasive issue in many scientific disciplines. The nature of how things charge has yet to be fully explained. Part of this study approaches the question of how and why certain materials acquire charge on the microscopic scale. In particular, this study focuses on the amount and distribution of charge acquired from metal/insulator contacts. Since the AFM is capable of measuring sub-nanonewton forces, it provides a unique method for investigating electrostatic interactions.

Chapter two will discuss the long-range forces which influence the interactions between the particles and flat surfaces. Chapter three will briefly describe the AFM apparatus used, and the physics behind the cantilever motion. Chapter four details the experimental procedure for measuring the interactions, as well as properties of the materials being studied. Chapter five presents experimental data for the interaction between micrometer-sized polystyrene spheres and HOPG substrates. Chapter six explains the concepts behind contact electrification, and describes experimental measurements of charge transfer between particles and surfaces. In chapter seven, a summary is made of the results of this study.

## 2. Long-Range Interaction Forces

### 2.1 Van der Waals and Dispersion Forces

The interaction of bodies with one another takes a variety of forms. The strength of the interaction depends highly on the range, physical, and chemical characteristics of the bodies. In order to understand the interaction forces between macroscopic objects, it is necessary to understand what governs the interactions between atoms and molecules. The strength of the force between objects also depends on the range over which they are separated. All objects experience an attraction due to gravitational force, however, it is too weak to explain intermolecular interactions. Another force which all atoms and molecules experience is the van der Waals force. This force is dominant for separations from one nanometer out to several hundred nanometers.

The discovery of this force came from van der Waals' study of real gases. In an attempt to explain why gases do not obey the equation of state for an ideal gas ( $PV=RT$ ), van der Waals came up with the relation,

$$\left(P + \frac{a}{V^2}\right)(V - b) = RT . \quad (2.1)$$

The first correction,  $\frac{a}{V^2}$ , describes an effect of attractive intermolecular force

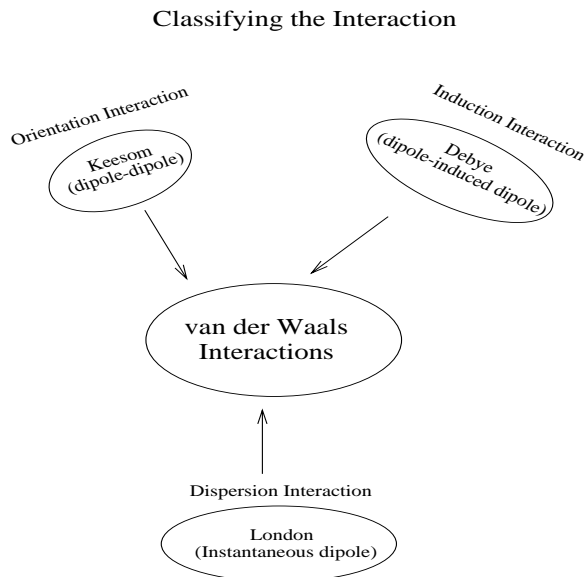


Figure 2.1

Contributions to the van der Waals interaction.

known as the van der Waals force. The second correction,  $b$ , accounts for the finite size of gas molecules. This early work led others to pursue a generalized force law which could explain intermolecular interactions.

The van der Waals force actually consists of three components (Keesom, Debye, and Dispersion forces) (see Fig. 2.1). The Keesom and Debye forces arise from interactions between fixed dipoles. The contributions of these two terms to the total van der Waals force depends on whether or not the interacting materials are polar. Dispersion forces are always present because they arise from the instantaneous dipole moments that occur from electrons orbiting their nuclei (see Fig. 2.2). Even though the van der Waals force is quantum mechanical in origin, classical arguments can be used to illustrate how these interactions arise. Consider

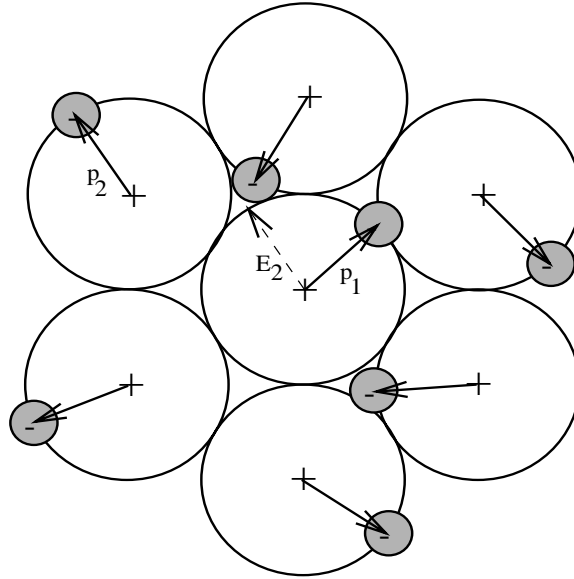


Figure 2.2

Classical model for the dispersion interaction

a dispersion interaction between two Bohr atoms:

At any instant in time, an atom will have a dipole  $p_1 = qa$  ( $a$ =Bohr radius,  $q$ =charge) which will create an electric field ( $E_2$ ) given by.

$$E_2 = \frac{p_1}{4\pi\epsilon_0 a^3} \quad (2.2)$$

A second atom will then have an induced dipole given by,

$$p_2 = \alpha E_2 \quad (2.3)$$

where  $\alpha$  is the polarizability of the atom or molecule.

$$\alpha = \frac{p_2}{E_2} = \frac{qa}{\frac{q}{4\pi\epsilon_0 a^2}} = 4\pi\epsilon_0 a^3 \quad (2.4)$$

The energy of the second dipole is

$$U = -p_2 E_2 \quad (2.5)$$

or,

$$U = -\frac{\alpha q^2 a^2}{(4\pi\epsilon_o)^2 R^6}. \quad (2.6)$$

By making a substitution using the relation for the Bohr radius ( $\nu$  is the orbiting frequency of the electron in a Bohr atom.)  $R$  is the separation between interacting molecules.

$$a = \frac{q^2}{2(4\pi\epsilon_o)h\nu}, \quad (2.7)$$

the energy relation can be expressed as

$$U = -\frac{2h\nu\alpha^2}{(4\pi\epsilon_o)^2 R^6}. \quad (2.8)$$

London made a similar calculation using quantum mechanics and found that the energy is given by[15]

$$U = -\frac{3}{4} \frac{\alpha^2 h\nu}{(4\pi\epsilon_o)^2 R^6} = -\frac{C}{R^6}. \quad (2.9)$$

The force is then given by

$$F = -\frac{dU}{dR} = -\frac{9}{2} \frac{\alpha^2 h\nu}{(4\pi\epsilon_o)^2 R^7} \quad (2.10)$$

which gives the same power-law dependence and agrees to within a numerical constant with the classical result.[15]

Models were developed to describe the interaction potential between atoms and molecules in order to describe the repulsive and attractive forces observed. These approaches were all empirical until London considered the combined influence of the Keesom, Debye, and dispersion interactions. It is interesting to note that these forces which seem to come from nowhere have a surprising strength. In the case of the dispersion energy, two atoms in contact have an energy of  $\sim 1kT$ . It is then not surprising that the interaction between macroscopic objects due to van der Waals forces may be quite large.

Casimir determined that the dispersion force experiences a retardation effect when the interacting atoms or molecules have a separation distance on the order of the characteristic absorption wavelength.[16] This retardation effect is due to the finite time required for the field transmitted from a fluctuating dipole to reach a neighboring atom and then return. When the distance the field travels is comparable to the period of the fluctuation, retardation takes effect. This decreases the power-law of the interaction by an order of magnitude. As the separation increases further, there is a gradual transition back to the non-retarded power-law dependence. A general expression for the van der Waals force between atoms and molecules is then,

$$F_{molecule}(z) = -\frac{C_{nr}}{z^7} - \frac{C_r}{z^8} \quad (2.11)$$

where  $C_{nr}$  and  $C_r$  are the non-retarded and retarded London coefficients.[15]

It should be noted here that retardation effects are not considered in this study. As will be shown later, the range where the retardation effect becomes dominant is shrouded by longer range electrostatic effects.

### 2.1.1 Microscopic Model

The existence of van der Waals forces between atoms and molecules was extended to macroscopic bodies with small separations. Hamaker applied London's model to calculate the interaction between two spheres and a sphere and flat plane.[1] By assuming that the van der Waals potential between atoms is additive, the interaction between the objects is a simple integration over their geometric shapes. This is known as the microscopic model because it is based on pairwise summation over the contributions from the individual atoms of each object. The net potential of the interaction is,

$$U_{microscopic} = \int_{object1} \int_{object2} \left( \frac{C_{nr}}{z^6} + \frac{C_r}{z^7} \right) d\Omega_1 d\Omega_2 \quad (2.12)$$

where  $\Omega_1$  and  $\Omega_2$  refer to the interacting bodies. The interaction force is then given by,

$$F_{microscopic} = -\frac{\partial U_{microscopic}}{\partial z} . \quad (2.13)$$

<b>Microscopic Model</b>		
Geometry	Non-retarded Force	Retarded Force
Cylinder-Plane	$\frac{H_{nr}r^2}{6\pi z^3}$	$\frac{\pi H_r r^2}{z^4}$
Sphere-Plane	$\frac{H_{nr}R}{6z^2}$	$\frac{2\pi H_r R}{3z^3}$
Plane-Plane (Force per unit area)	$\frac{H_{nr}}{6\pi z^3}$	$\frac{H_r}{z^4}$

Table 2.1

Van der Waals interaction forces for various geometries as calculated using a microscopic model.

Table 2.1 gives a list of interaction forces for common geometries. The cylinder-plane geometry refers to the face of the cylinder parallel to the plane of the half-space.

The two terms describing the interaction due to dispersion forces have individual coefficients which distinguish the components. Because Hamaker was one of the first to derive a theory for an interaction across an interface, the coefficients bear his name. The non-retarded Hamaker coefficient is associated with the interaction term in the range where maximum attraction occurs. The retarded Hamaker coefficient is associated with the interaction term in the range where the interaction is diminished by the effects of the fluctuating dipoles in the materials.

$$H_{nr} = \pi^2 C_{nr} \rho_1 \rho_2 \quad (2.14)$$

and

$$H_r = \frac{\pi C_r \rho_1 \rho_2}{10} \quad (2.15)$$

The Hamaker constants ( $H_{nr}, H_r$ ) are calculated from London coefficients ( $C_{nr}, C_r$ ) and atomic densities ( $\rho_1, \rho_2$ ). [1] Although this approach is oversimplified since it ignores the contributions of neighboring atoms, the overall result is consistent with more complete models derived using quantum theory. [3]

### 2.1.2 Macroscopic Model

The correct approach to determine the interaction is using a macroscopic model based on quantum field theory. Lifshitz was the first to consider the problem of two half spaces separated by vacuum using a continuum approach. [2] The continuum approach extends the idea of an interaction force due to individual fluctuating dipoles to an interaction force due to fluctuating electromagnetic fields occurring between the media. A later work by Dzyaloshinskii, Lifshitz, and Pitaevskii (DLP) generalized Lifshitz's original model to account for an interaction between two half spaces of dielectric constant  $\epsilon_1$  and  $\epsilon_2$  separated by a gap separation  $l$  and separated by a third medium with dielectric constant  $\epsilon_3$ . [10] These were the first models that determined the interaction force using macroscopic properties of the materials. The most important features of these models is that the same power-law dependencies are obtained and the Hamaker constants are determined from optical properties of the interacting materials. Due to the complexity of the DLP model, only the general expression for  $f_{DLP}$ , force per unit area between the two half spaces is

shown.

$$f_{DLP} = \frac{\hbar}{2\pi^2 c^3} \int_0^\infty \int_1^\infty dp d\xi p^2 \xi^3 \epsilon_3^{\frac{3}{2}} \left\{ \left[ \frac{(s_1 + p)(s_2 + p)}{(s_1 - p)(s_2 - p)} e^{\frac{2p\xi l \sqrt{\epsilon_3}}{c}} - 1 \right]^{-1} + \left[ \frac{(s_1 + p \frac{\epsilon_1}{\epsilon_3})(s_2 + p \frac{\epsilon_2}{\epsilon_3})}{(s_1 - p \frac{\epsilon_1}{\epsilon_3})(s_2 - p \frac{\epsilon_2}{\epsilon_3})} e^{\frac{2p\xi l \sqrt{\epsilon_3}}{c}} - 1 \right]^{-1} \right\} \quad (2.16)$$

$$s_1 = \sqrt{\frac{\epsilon_1}{\epsilon_3} - 1 + p^2} \quad (2.17)$$

$$s_2 = \sqrt{\frac{\epsilon_2}{\epsilon_3} - 1 + p^2} \quad (2.18)$$

The variables  $p$  and  $\xi$  are variables of integration related to the electromagnetic wave vectors.

In order to determine the value of the integral, it is necessary to know the dielectric behavior of the media over the entire electromagnetic spectrum. In most cases, it is impossible to know the complete spectral behavior so a functional relation which satisfactorily describes the absorption regions is used. Typically, the permittivity can be described by a function of the form,

$$\epsilon(\omega) = 1 + \frac{Const}{\omega_o^2 - \omega^2 + i\Delta\omega \cdot \omega} \quad (2.19)$$

where  $\omega_o$  is the frequency of the strongest absorption peak and  $\Delta\omega$  is the half width of the peak. Dielectric permittivities are modeled in this way are often rewritten as

$$\epsilon(\omega) = \epsilon'(\omega) + i\epsilon''(\omega) . \quad (2.20)$$

The permittivities in Eqn. 2.16 are functions of a complex frequency ( $\epsilon(i\omega)$ ). In order to calculate the force, the Kramers-Kronig relation

$$\epsilon(i\xi) = 1 + \frac{2}{\pi} \int_0^\infty \frac{\omega \epsilon''(\omega)}{\omega^2 + \xi^2} d\omega . \quad (2.21)$$

is used to evaluate the integral assuming the values for  $\epsilon''(\omega)$  are known for the materials.

Further simplification of the integral are made by looking at limiting cases of the separation distance between the half-spaces. For small separations (small compared to the absorption wavelengths of the dielectrics corresponding to the non-retarded regime),

$$f_{non-retarded} = \frac{\hbar}{8\pi^2 z^3} \int_0^\infty \sum_{n=1}^\infty \frac{1}{n^3} \left[ \frac{(\epsilon_1 - \epsilon_3)(\epsilon_2 - \epsilon_3)}{(\epsilon_1 + \epsilon_3)(\epsilon_2 + \epsilon_3)} \right]^n d\xi . \quad (2.22)$$

For large separations, the power-law dependence increases due to retardation effects,

$$f_{retarded} = \frac{\pi^2 \hbar c}{240 z^4 \sqrt{\epsilon_3(0)}} \left( \frac{(\epsilon_1(0) - \epsilon_3(0))(\epsilon_2(0) - \epsilon_3(0))}{(\epsilon_1(0) + \epsilon_3(0))(\epsilon_2(0) + \epsilon_3(0))} \right) \phi(\epsilon_1(0), \epsilon_2(0), \epsilon_3(0)) . \quad (2.23)$$

The function  $\phi(\epsilon_1(0), \epsilon_2(0), \epsilon_3(0))$  has a value between 1 and  $\frac{69}{2\pi^4}$  depending on the interacting materials.[17]

Other theories have been developed for interactions in different media and between dielectrics and metals. However, the only major difference between these macroscopic models and the microscopic models is the way in which the Hamaker constant is calculated. The power-law dependence for the various geometries are identical to the microscopic model for both the non-retarded and retarded regimes.

A model developed by Hartmann gives a general method for calculating the interaction due to van der Waals forces for various geometries and a flat surface.[11] This is of particular importance because of its applicability to atomic force microscopy. The interaction force between an AFM probe and substrate may be expressed by

$$F(d) = \int_d^\infty \frac{\partial f_{DLP}}{\partial z} G(z - d) dz \quad (2.24)$$

where the integrand consists of force gradient  $\frac{\partial f_{DLP}}{\partial z}$  found from Eqn. 2.16 and a geometric term  $G(z - d)$  that represents the cross-sectional area of the probe (see Fig. 2.3).

As in the derivation of the earlier models, the interaction force consists of a non-retarded and retarded regime which is defined by the characteristic absorption wavelength,  $\chi$ , for the interacting materials ( $d$  is the probe-substrate separation, and  $z$  is the coordinate variable for the probe.). As a result, the following restrictions are applied to the integration,

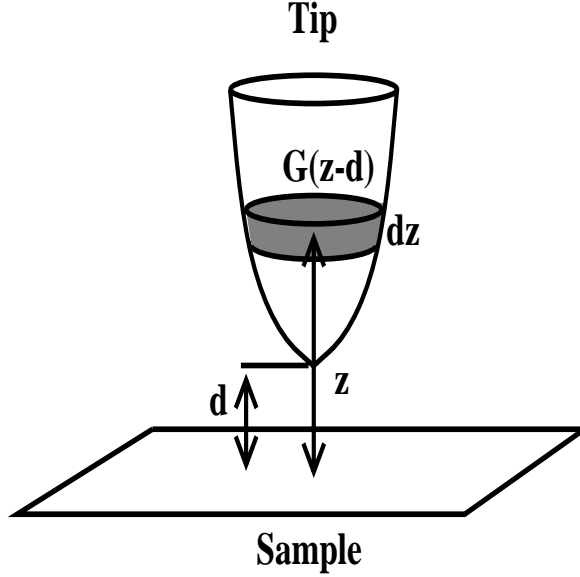


Figure 2.3

Macroscopic model for van der Waals interaction.

$$\frac{\partial f_{nr}(d > \chi)}{\partial z} = 0 \quad \text{and} \quad \frac{\partial f_r(d < \chi)}{\partial z} = 0 . \quad (2.25)$$

By knowing the actual geometry of the probe, two constants  $g_{nr}$  and  $g_r$  which depend solely on probe geometry, can be defined after integration. The net interaction force for the non-retarded and retarded limit can then be determined based on geometric parameters and dielectric properties of the materials. The general expressions for the interaction force is then,

$$F_{nr}(d) = \frac{g_{nr} H_{nr}}{d^n} \quad (2.26)$$

and,

$$F_r(d) = \frac{g_r H_r}{d^{n+1}} . \quad (2.27)$$

<b>Modified Macroscopic Model</b>	
Geometry	Non-Retarded Force
Cone-Plane	$\frac{H_{nr} \tan^2 \theta}{6z} [a]$
Sphere-Plane	$\frac{H_{nr} R}{6z^2}$
Plane-Plane (Force per unit area)	$\frac{H_{nr}}{6\pi z^3}$

Table 2.2

Macroscopic Lifshitz model used to calculate non-retarded van der Waals forces. [a]  $\theta$  corresponds to the half-angle aperture of the cone.

The Hamaker constants are now given by

$$H_{nr} = \frac{3\hbar}{4\pi} \int_0^\infty \sum_{n=1}^\infty \frac{1}{n^3} \left[ \frac{(\epsilon_1 - \epsilon_3)(\epsilon_2 - \epsilon_3)}{(\epsilon_1 + \epsilon_3)(\epsilon_2 + \epsilon_3)} \right]^n \quad (2.28)$$

and,

$$H_r \approx \frac{3\hbar c}{16\pi^2 \sqrt{\epsilon_3(0)}} \left( \frac{(\epsilon_1(0) - \epsilon_3(0))(\epsilon_2(0) - \epsilon_3(0))}{(\epsilon_1(0) + \epsilon_3(0))(\epsilon_2(0) + \epsilon_3(0))} \right) \phi(\epsilon_1(0), \epsilon_2(0), \epsilon_3(0)) . \quad (2.29)$$

Table 2.2 gives the results for the non-retarded limit for a few geometries.

In order to determine the macroscopic Hamaker constants the probe and sample material must be specified (metallic or dielectric) and the geometry of the probe must be known. Due to the complexity in calculating the macroscopic Hamaker constants for the interaction between different materials, a detailed treatment will not be discussed. As with the Lifshitz model, the results will vary depending on

the nature of the interacting materials. Metals and dielectrics will have different approximations for the permittivity relations. In many cases, detailed optical information is not known so the Hamaker constant may be estimated from the surface free energy,  $\gamma_{12}$ , and the combining relation for Hamaker constants.[18] For two different materials interacting across a vacuum, the Hamaker constant is often estimated from the interaction between identical materials ( $H_{11}$  and  $H_{22}$ )

$$H_{nr} \approx \sqrt{H_{11}H_{22}} . \quad (2.30)$$

In general, the strength of the van der Waals interactions between two materials may be categorized in the following way: metal-metal > metal-insulator > insulator-insulator. Some examples of the Hamaker coefficients for two similar and dissimilar materials are given in Tables 2.3 and 2.4.[19]

## 2.2 Electrostatic Interaction Model

Electrostatic interactions exist throughout nature. Since all matter has charge, it is important to understand what influence electrostatic forces have on objects. The electrostatic force is a long-range force which extends from nanometers out to infinity. The behavior of the force will depend on the amount and distribution of charge on the interacting objects. What will be considered in this section is the limiting cases for a charge distribution which can occur on a micrometer-sized dielectric sphere. The limiting cases are that the charge may be uniformly distributed over the entire sphere, or the charge is distributed nonuniformly over

<b>Hamaker Coefficients <math>H_{131}</math></b>	
Materials	$H_{nr}$
Au-Au	14.3 eV
Ag-Ag	11.7 eV
Cu-Cu	8.0 eV
Diamond-Diamond	8.6 eV
Si-Si	6.8 eV
$H_2O - H_2O$	1.4 eV
HOPG-HOPG	0.5 eV
Polystyrene-Polystyrene	1.9 eV

Table 2.3

Non-Retarded Hamaker Coefficients for two similar materials interacting across a vacuum.

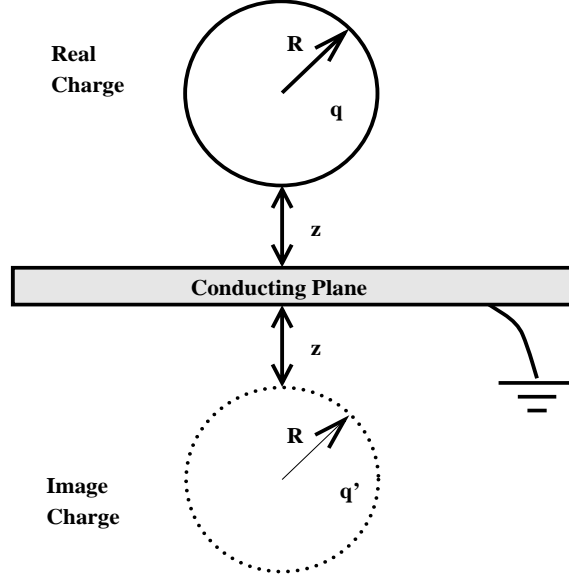


Figure 2.4

## Electrostatic interaction due to contact electrification

the sphere. Nominal values for both scenarios are given in Table 2.5.

In the case of a uniformly charged sphere near a grounded plane, the interaction may be calculated by a simple image charge method (see figure 2.4), where  $q$  and  $q'$  are the real and image charge. The interaction force due to this charge distribution is given by

$$F_{electrostatic}(z) = -\frac{q^2}{16\pi\epsilon_0(z+R)^2}. \quad (2.31)$$

The models describing uniform and localized charging are very similar. The main difference between them is the effective radius being considered. Let us first consider the case of a uniformly charged sphere of radius  $R$ , and charge  $q$  near a conducting surface. One important point to consider for a uniform charge

<b>Hamaker Coefficients <math>H_{132}</math></b>	
Materials	$H_{nr}$
Au-Cu	6.4 eV
Au-Diamond	6.1 eV
Au-Si	5.3 eV
Polystyrene-Graphite	1.0 eV
Au-Polystyrene	0.7 eV

Table 2.4

Non-Retarded Hamaker Coefficients for two dissimilar materials interacting across a vacuum.

<b>Electrostatic Model Parameters</b>		
Parameters	Uniform	Localized
$\sigma (\frac{C}{m^2})$	$\sim 10^{-5}$	$\sim 10^{-3}$
R ( $\mu\text{m}$ )	$\sim 3.$	$\sim 3.$
$R_{eff}$ (nm)	–	$\sim 50.$

Table 2.5

Parameters for both uniform and localized charge distributions.

distribution is that at separations much smaller than the dimensions of the sphere, the force will appear to remain relatively constant. Depending on the amount of charge distributed over the sphere, the electrostatic force may dominate over the van der Waals interaction.

The other possibility is that the charge may not be uniformly distributed over the sphere. For simplicity, assume that the primary region where the charge is localized is in a region where the sphere makes contact with the sample surface. Furthermore, suppose that the region may be approximated as spherical. The model for the electrostatic force of attraction will be identical to that of a uniformly charged sphere. The main point is that both the amount of charge and the effective region of charging differ from that of the model for a uniformly charged sphere. Again, we may ask what reasonable approximations can be made for the effective region of charge, as well as the amount of charge that can exist. The charge distribution is approximated by a spherical region using the effective radius,  $R_{eff}$ . An image charge distribution is created since the substrate is grounded and conductive. The resulting force is given by

$$F_{electrostatic}(z) = -\frac{q^2}{16\pi\epsilon_o(z + R_{eff})^2} . \quad (2.32)$$

An important point which will be discussed in detail is how charge is acquired. In particular, if the sphere makes contact with a surface, the region of contact can be determined using the Johnson-Kendall-Roberts (JKR) model for adhesion.[20]

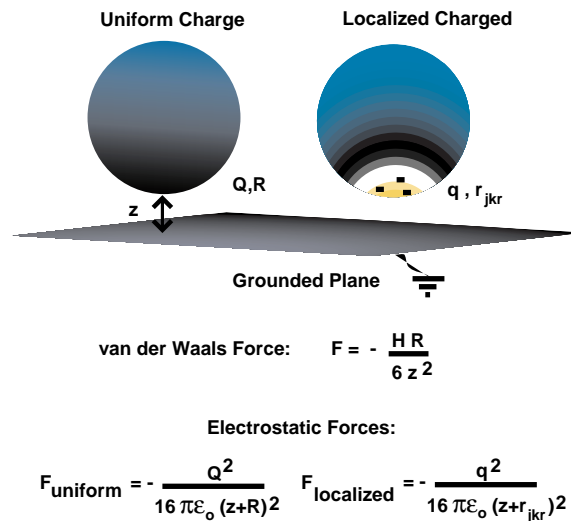


Figure 2.5

Contributions to the Interaction.

In this model, a radius of contact may be determined by knowing the surface energy of the interacting materials and the load applied to bring them into contact. The charged region can be estimated by a spherical region with an effective radius defined by the region of contact. The behavior of the electrostatic interaction for a sphere with a localized distribution of charge will be different than that for a uniformly charged sphere as shown in Fig. 2.5. Since the distribution of charge is not necessarily known *a priori*, having a technique which would determine the nature of the interaction would be quite useful. For a micron-sized sphere that may be charged, the AFM can provide such a method for discerning the nature of the charge distribution.

In order to define the origin of the localized charge, it is necessary to briefly

mention the JKR model for adhesion.[20] The model is used to predict the adhesion between elastic objects. Adhesion occurs because of the interfacial energy arising from the two bodies making contact. In order to pull the two objects apart, a finite amount of force is required as given in Eqn. 2.33

$$F_{adhesion} = -\frac{3}{2}\pi RW_{12} \quad (2.33)$$

The JKR model correctly predicts that when a sphere makes contact with a flat surface, a finite area of contact is formed with a radius  $a_{JKR}$  given by

$$a_{JKR} = \left( \frac{R}{K} \left[ F + 3\pi RW_{12} + \sqrt{6\pi RW_{12}F + (3\pi RW_{12})^2} \right] \right)^{\frac{1}{3}} \quad (2.34)$$

where  $K$  is the elastic moduli, and  $W_{12}$  is the surface energy per unit area

$$W_{12} \approx \sqrt{\gamma_1 \times \gamma_2} . \quad (2.35)$$

The surface energies of the interacting materials are  $\gamma_1$  and  $\gamma_2$ .

For dielectric materials such as polystyrene, it is not likely that the sample is electrically neutral. Determining the amount of charge and the charge distribution is usually difficult. The approach taken in what follows is to specify an appropriate electrostatic model which best fits the data. It is assumed that the polystyrene sphere is charged by contact-electrification when it comes into contact with the HOPG substrate. Based on the JKR theory of adhesion, a calculation of the contact area of the sphere with the substrate is made assuming zero load ( $F = 0$

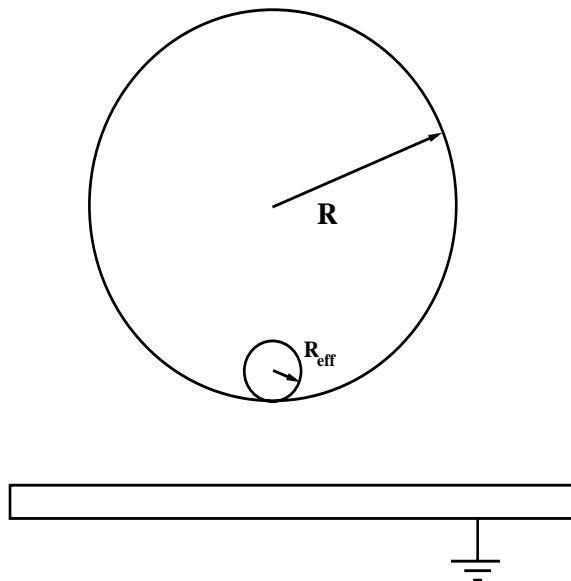


Figure 2.6

## Electrostatic interaction due contact electrification

in Eqn. 2.34).[21]

Using the area of contact calculated, an effective radius of contact ( $R_{\text{eff}} = a_{JKR}$ ) is determined. The most simplistic model is that charge is deposited in a spherical area estimated using the effective radius (Fig. 2.6).

The charge on the polystyrene sphere is determined from a fit to the actual data. While the model is simplistic, it does give a generalized picture of how an additional electrostatic force can influence the overall interaction between the polystyrene sphere and HOPG substrate. The two possible scenarios are that the sphere is either uniformly charged, or is non-uniformly charged. The resulting forces are plotted in Figs. 2.7 and 2.8.

It is interesting to consider which of the contributions would be the greatest for

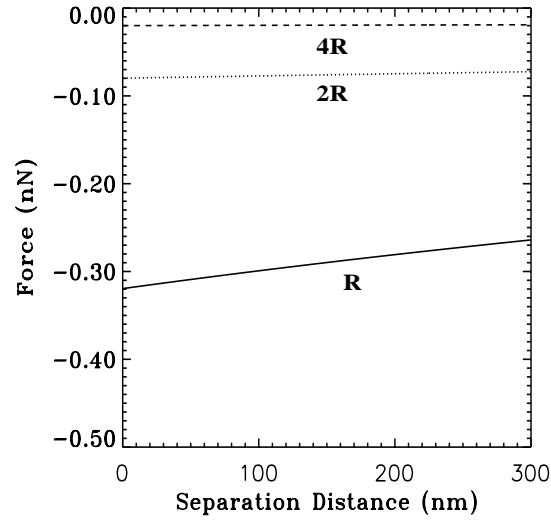


Figure 2.7

Uniform charge distribution as a function of sphere radius. The charge density  $\sigma$  remains fixed, while the radius ( $R = 3 \mu\text{m}$ ) is changed.

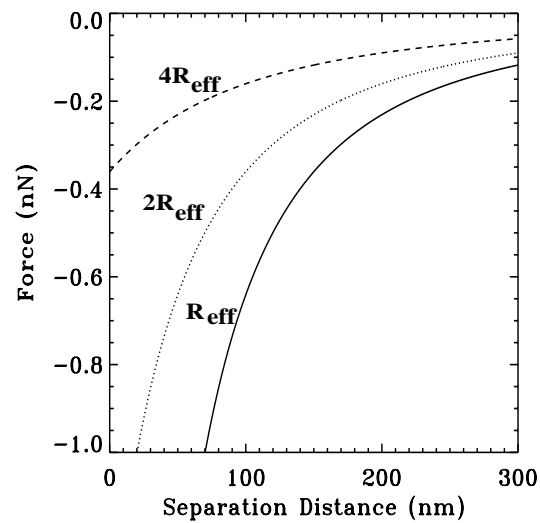


Figure 2.8

Localized charge distribution as a function of the effective region of contact. The charge density  $\sigma$  of the charged patch region remains fixed, while  $R_{eff} = 50 \text{ nm}$  is changed.

<b>Relative Contributions</b>			
Parameters	van der Waals	Uniform	Localized
H (eV)	1.	–	–
$\sigma \frac{C}{m^2}$	–	$\sim 10^{-5}$	$\sim 10^{-3}$
R ( $\mu\text{m}$ )	1.-10.	1.-10.	1.-10.
$R_{eff}$ (nm)	–	–	150.

Table 2.6

Parameters for both uniform and localized charge distributions.

a given sphere radius. This is especially important with micrometer-sized particles. As the particles decrease in size, a charge distribution may produce a long-range force much greater than that of a pure van der Waals interaction. This is illustrated in Figs. 2.9-2.11 where the magnitude of the contributing forces are plotted for varying sphere size at different separation distances. The dominant force will depend on the separation distance between the surface and the particle. At larger separations, the localized charge dominates the interaction. At smaller separations, the van der Waals force dominates the interaction. Table 2.6 gives the parameters used. The issue of the dominant interaction force will be addressed in more detail later.

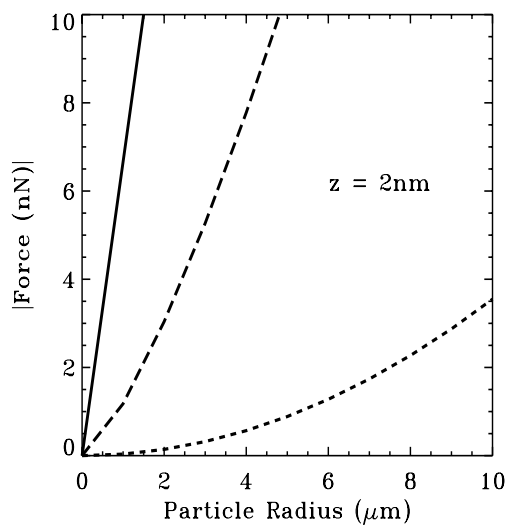


Figure 2.9

Interaction forces as a function of sphere size at a fixed separation of 2 nm. Interactions shown are van der Waals (solid line), localized electrostatic (dashed line), uniform electrostatic (dotted).

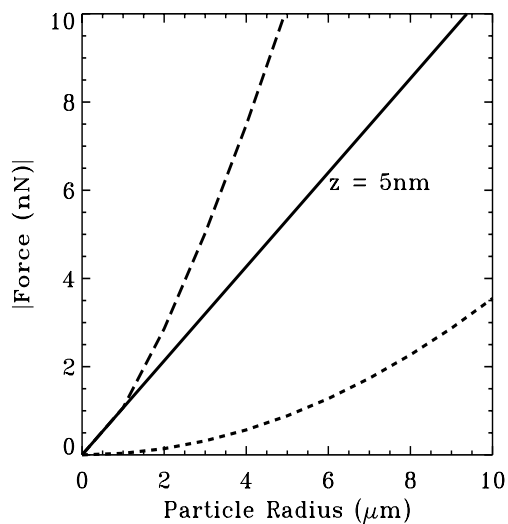


Figure 2.10

Interaction forces as a function of sphere size at a fixed separation of 5 nm. Interactions shown are van der Waals (solid line), localized electrostatic (dashed line), uniform electrostatic (dotted).

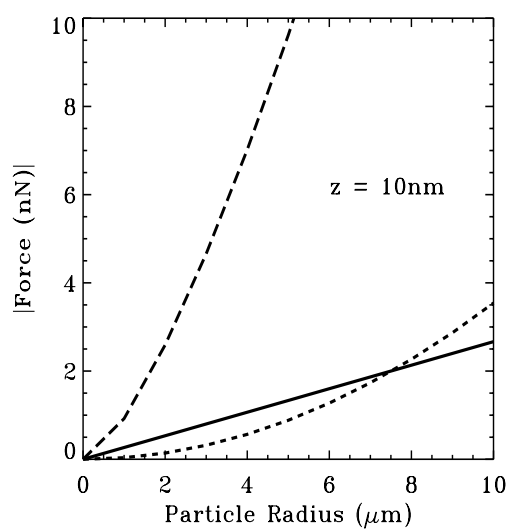


Figure 2.11

Interaction forces as a function of sphere size at a fixed separation of 10 nm. Interactions shown are van der Waals (solid line), localized electrostatic (dashed line), uniform electrostatic (dotted).

### 3. Principles of the Atomic Force Microscope

#### 3.1 Apparatus Design

The atomic force microscope used to measure interaction forces was originally built by D.M. Schaefer and described in further detail in his thesis.[22] This particular instrument can image surfaces in both contact and non-contact modes of operation. In order to perform interaction force measurements using this AFM, the same instrumentation is used as for these two imaging modes of operation. An illustration of the AFM apparatus is given in Fig. 3.1.

The main element of AFM operation is a lever arm which is deflected due to interaction forces between it and a sample. This deflection mechanism may be monitored by a variety of techniques.[23, 24, 25, 26, 27, 28] The technique used for this particular microscope is a laser deflection system with a position sensing detector (PSD). The position sensing detector (PSD) is a split photodiode detector. A beam is focused onto the AFM cantilever and the reflected beam is then monitored by the split photodiode detector. The motion of the cantilever is monitored by a Motorola 68030 CPU based computer which uses the detector signal as a feedback mechanism for scanning. Another unique feature of this AFM is a second laser/position sensing detector for the sample piezo tube. This second

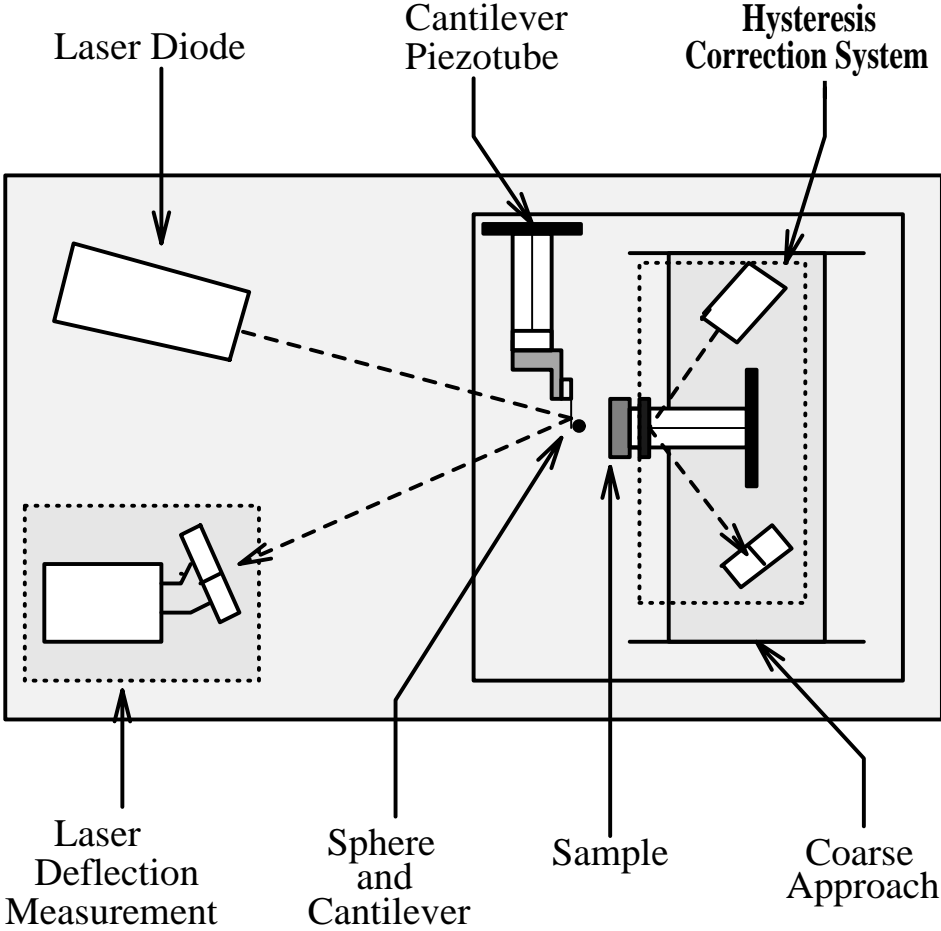


Figure 3.1

Atomic Force Microscope Design

detector allows for hysteresis correction in the tube motion. This is an important feature since the piezo tube expansion may become non-linear for large applied voltages.

In order to minimize mechanical vibration, the AFM has two isolation stages. The AFM instrument rests on a steel plate with a Viton O-ring spacer. Secondly, the AFM chamber sits on an air table to reduce vibrational effects of the building. This vibrational isolation is especially important to obtain sub-nanonewton force sensitivity. For this instrument, the sensitivity in measuring force and force gradients is  $\sim 10^{-11}$  N and  $\sim 10^{-4} \frac{N}{m}$ .

The entire AFM apparatus is enclosed in a UHV chamber. Although the AFM is not UHV compatible, the chamber allows for measurements at moderate vacuum or in a dry nitrogen environment. The chamber may be evacuated to less than 5 mTorr using two liquid nitrogen sorption pumps (See Fig. 3.2).

A humidity sensor was incorporated into the system in order to monitor atmospheric conditions within the chamber. It is mounted to the 8 inch flange used to seal the chamber. The sensor is comprised of a capacitor whose capacitance varies with changes in the relative humidity. The circuit diagram is shown in Fig. 3.4. The circuit outputs a proportional frequency which is converted to a voltage using a frequency to voltage circuit shown in Fig. 3.5. Calibration was done against a humidity sensor made by Omega Instruments (see Fig. 3.6). Although most measurements were performed at either ambient or moderate vacuum, the sensor could be used to measure levels ranging from 0-100% relative humidity (RH).

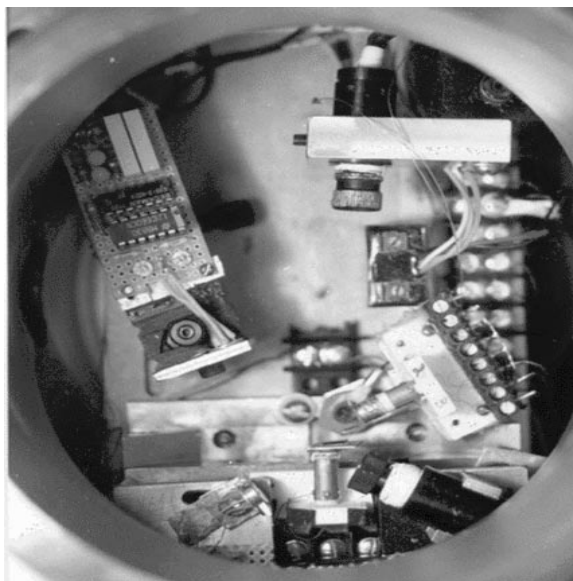


Figure 3.2

AFM is enclosed in a UHV chamber capable of pumping down to a moderate vacuum.

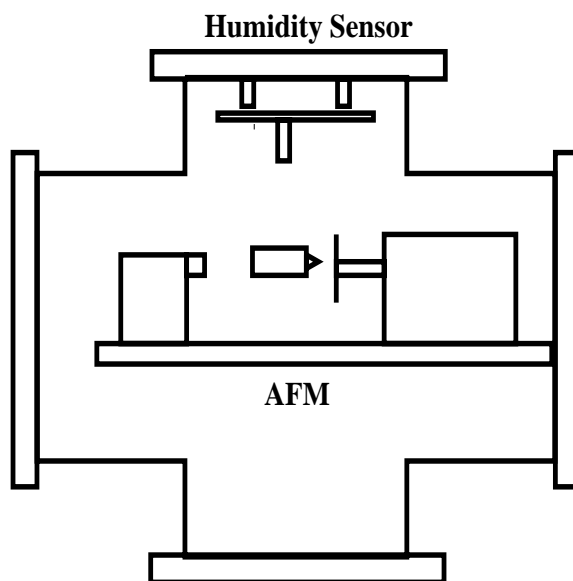


Figure 3.3

Diagram illustrating the humidity sensor mounting in the chamber.

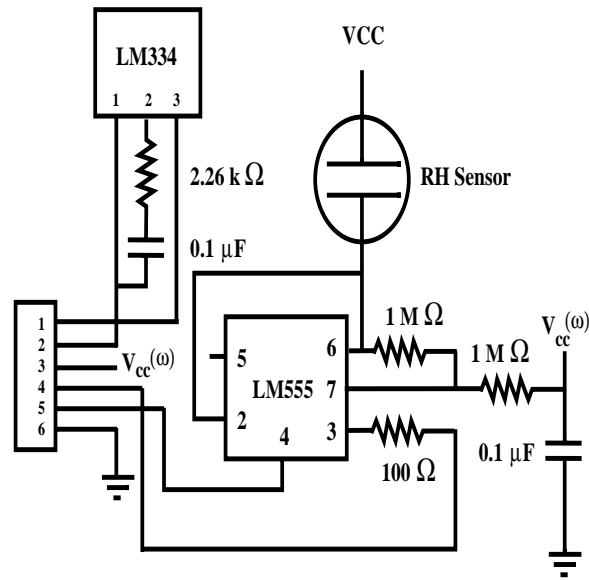


Figure 3.4

Circuit schematic for the humidity sensor.

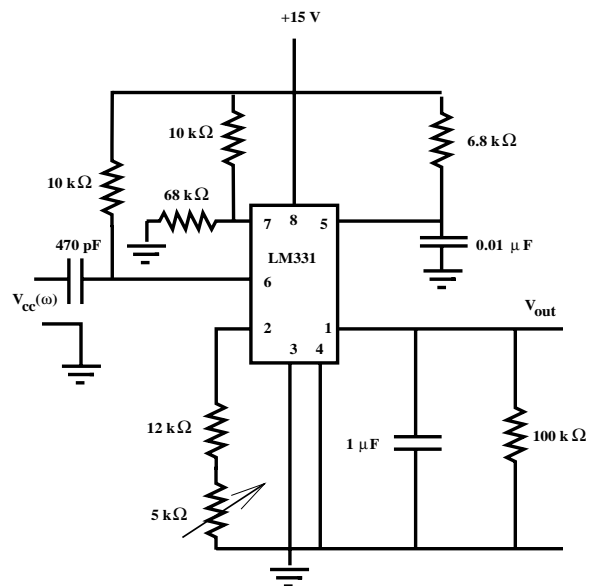


Figure 3.5

Frequency to voltage converter circuit.

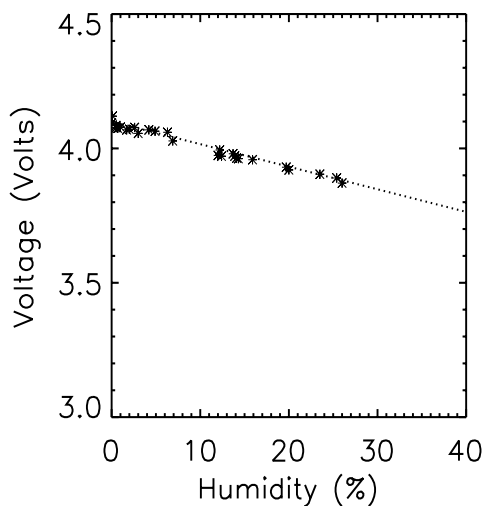


Figure 3.6

Humidity sensor calibration.

## 3.2 Lever Mechanics

### 3.2.1 Cantilevers

In order to make quantitative studies of the interaction force, the properties of the cantilevers used must fully be understood. The AFM cantilevers used in this work are commercially available, but their individual properties vary enough so that the characteristics of each cantilever must be considered. In order to measure the inter-atomic forces, it is necessary to select cantilevers which are suitable for measuring such forces. The most obvious property to determine is the cantilever's spring constant. The spring constant is extremely important because it defines the limits in resolution of the interaction forces. The more flexible the lever (lower spring constant), the more sensitive it will be to longer range forces. However,

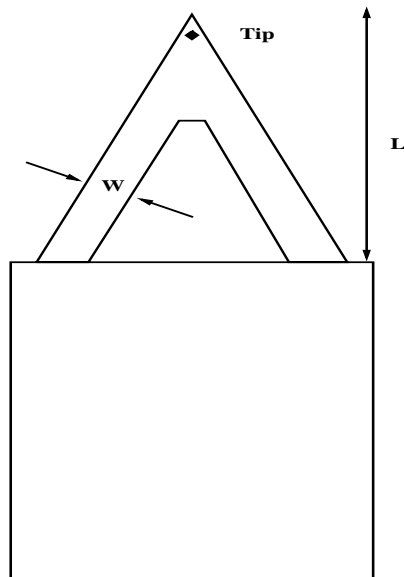


Figure 3.7

Typical cantilever geometry.

the trade-off is that a spring with a lower spring constant will be unable to probe interaction forces in close proximity to the surface. This feature is of critical importance when studying the interaction forces between micron-sized spheres and surfaces which are quite large on the scale of forces measured using the AFM.

To calculate the spring constant, one must consider both the geometry of the lever and its material properties. All the levers used in this work were silicon Ultralevers purchased from Park Scientific Instruments. The cantilevers have the V-shaped double arm (see Fig. 3.7), but the spring constant can be approximated to rectangular beams in parallel with an error of 16%. [29]

There are several approaches to determining the spring constant of the lever. All the methods were tried, but the most reliable method is the last to be discussed.

The standard approach is to measure the dimensions of the lever and by knowing the material properties, calculate the spring constant. This method is referred to as the geometric method. For a rectangular lever, the spring constant is defined as

$$k_{rect} = \frac{Ewt^3}{4l^3} . \quad (3.1)$$

where  $E$  is the elastic modulus,  $w$  is the width of the lever,  $t$  is the thickness, and  $l$  is the length of the lever. Approximating the V-shaped cantilever to two rectangular beams in parallel gives a spring constant

$$k_v = \frac{Ewt^3}{2l^3} . \quad (3.2)$$

An alternative method in determining the spring constant of the lever was proposed by Cleveland *et al.*[30] They describe a method in which known masses are attached to the levers. The change in the resonant frequency can be used to estimate  $k$  by

$$k = (2\pi^2) \frac{M}{\frac{1}{\nu_M^2} - \frac{1}{\nu_0^2}} . \quad (3.3)$$

where  $M$  is the added mass,  $\nu_M$  is the resonant frequency of the loaded lever, and  $\nu_0$  is the resonant frequency of the unloaded lever. While Eqn. 3.3 provides a highly accurate method to determine the spring constant of a cantilever, it can be quite tedious to perform this measurement because particle of known mass must be added.

A more direct method discussed by Cleveland *et al* is given by Eqn. 3.4,

$$k = 4\pi^3 l^3 w \sqrt{\frac{\rho^3}{E^3}} (\nu_0)^3 . \quad (3.4)$$

Equation 3.4 is referred to as the frequency method for determining the spring constant of a cantilever. The benefit obtained from this expression for the spring constant is that it is independent of the lever thickness. Because of the lithography process used in fabrication, the thicknesses of the levers are not always uniform. According to Eqn. 3.2, a slight variation in the thickness can have a dramatic effect on the spring constant since it has a cubic dependence. A comparison between both methods for determining the spring constant is made in Table 3.1.

In general, the resonance frequency measurement method is used to determine the spring constant of the cantilevers used in experiments. This technique is more reliable because it does not require knowing the thickness of the cantilever arms, which can be a large source of uncertainty. Table 3.2 lists a few cantilevers and their measured spring constants.

### 3.2.2 Force Detection

Once the spring constant of the lever is known, it is necessary to understand the behavior of the lever when measuring the interaction forces between it and a surface. According to Hooke's law, a spring will experience a displacement as a result of an applied force (see Fig. 3.8).

Spring Constant Calculation			
Parameters	Values	Geometric Tech. ( $\frac{N}{m}$ )	Frequency Tech. ( $\frac{N}{m}$ )
E (Pa)	$1.79 \times 10^{11}$	–	–
$\rho$ ( $\frac{kg}{m^3}$ )	2330.	–	–
$l$ ( $\mu\text{m}$ )	$160. \pm 2.$	5.9-6.4	2.3-2.5
$w$ ( $\mu\text{m}$ )	$35. \pm 2.$	5.8-6.5	2.3-2.6
$t$ ( $\mu\text{m}$ )	$2. \pm 0.5$	2.6-11.9	2.4-2.4
$\nu_{res}$ (Hz)	$80,000 \pm 5$	6.1-6.1	2.4-2.4

Table 3.1

A comparison between two methods for calculating the spring constant of a cantilever.

Measured Spring Constants			
Length ( $\mu\text{m}$ )	Width ( $\mu\text{m}$ )	Resonance Frequency (Hz)	Spring Constant ( $\frac{N}{m}$ )
$160. \pm 2.$	$32. \pm 2.$	$83,761. \pm 5.$	$2.5 \pm 0.3$
$151. \pm 2.$	$36. \pm 2.$	$75,821. \pm 5.$	$1.9 \pm 0.1$
$152. \pm 2.$	$36. \pm 2.$	$76,670. \pm 5.$	$1.9 \pm 0.1$
$155. \pm 2.$	$35. \pm 2.$	$78,590. \pm 5.$	$2.1 \pm 0.2$

Table 3.2

Spring constants for typical cantilevers used in experiments as calculated using resonance frequency method.

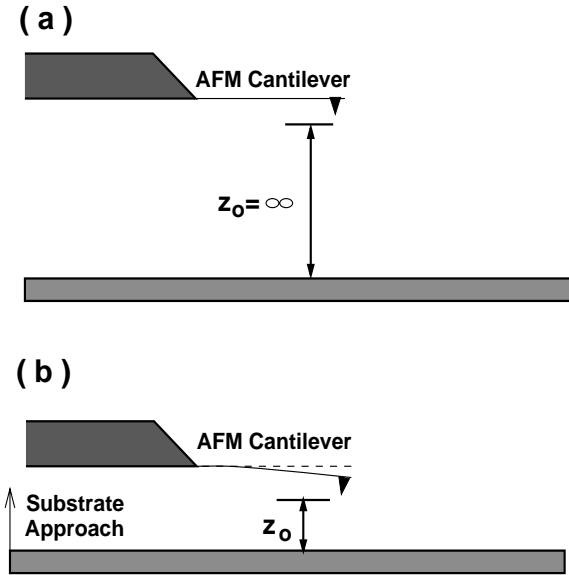


Figure 3.8

Deflection of cantilever due to tip-substrate interaction.

$$F_{applied} = k(z - z_0) \quad (3.5)$$

In the case of AFM cantilevers, the displacements are shown to be due to van der Waals and electrostatic forces.

It is important to consider how a cantilever deflects under the influence of an attractive interaction force. Figure 3.9 illustrates how deflection varies with spring constant for a van der Waals and localized electrostatic interaction between a  $3 \mu\text{m}$  radius sphere and flat surface. The spring constants illustrated in this figure range from  $0.2 \frac{\text{N}}{\text{m}}$  to  $2.0 \frac{\text{N}}{\text{m}}$ . The more flexible the cantilever, the further it deflects into the attractive field. A similar argument can be made if the interaction force is increased, rather than decreasing the spring constant. A stronger force field can

be achieved by decreasing the separation distance between the sphere mounted cantilever and surface. A larger force results in a greater deflection of the sphere-mounted cantilever toward the plane.

An important phenomenon with force measurements using the AFM cantilevers is the jump to contact (see Fig. 3.10). The cantilever experiences a nonuniform force field as the separation distance between the sample and surface decreases. The distance which the cantilever can move towards the sample without becoming unstable will depend on the geometry of the tip and the spring constant of the lever. This instability is defined as the point where the spring can no longer compensate for the interaction force with the surface. In order to determine the point of instability when the jump to contact occurs, it is necessary to know the interactions which the cantilever experiences. We will consider the effects of both van der Waals and electrostatic forces on this phenomena.

The mechanics for determining the jump-to-contact distance relies on two conditions. Both the net force and net force gradient between the cantilever and interaction fields must be balanced. These conditions are given by equations,

$$F_{net} = F_{spring} + F_{interaction} = 0 \quad (3.6)$$

and

$$F'_{net} = F'_{spring} + F'_{interaction} = 0 . \quad (3.7)$$

As we see in Figure 3.11, it is not sufficient to say the instability point occurs

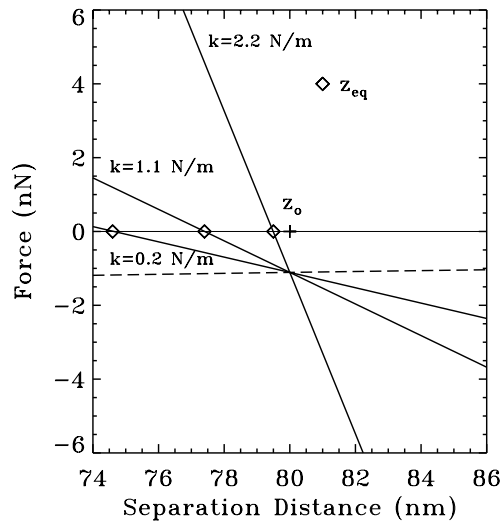


Figure 3.9

Variation of the cantilever deflection due to an attractive interaction force. The solid lines are the net interaction for varying spring stiffness. The spring constants are 0.2, 1.1, and 2.2 N/m. The interaction is due to a van der Waals and localized electrostatic force between a  $3 \mu\text{m}$  sphere and grounded plane (dashed line). The charge density is  $\sim 10^{-4} \frac{\text{C}}{\text{m}^2}$  localized in a  $\sim 100$  nm region. The equilibrium position with no forces present is 80 nm. The points marked by diamonds indicate the new equilibrium position for each spring in the presence of the force.

## Determining Jump-to-Contact

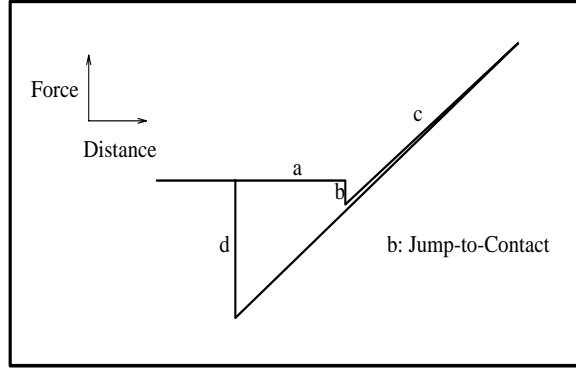


Figure 3.10

Jump to contact phenomenon.

when the net force gradient is unbalanced. The net force becomes unstable as the separation between the tip and sample decreases. At this critical point, the cantilever will deflect towards the surface to find an equilibrium position, but the point is unstable. As a result, the cantilever will jump into contact with the sample surface. The combination of these conditions determine the jump to contact distance.

If the interaction is purely van der Waals in origin, these conditions are then given by

$$F_{net} = k(z_o - z_{eq}) - \frac{HR}{6z_{eq}^2} = 0 \quad (3.8)$$

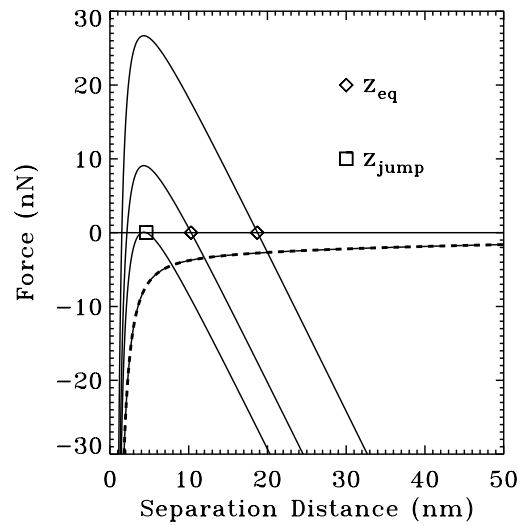


Figure 3.11

The net interaction (solid lines) is a combination of the attractive interaction force (dashed line) and the spring restoring force. As the separation distance between the sphere and sample decreases, the net interaction force changes. The points indicated by diamonds show how the equilibrium position changes due to the interaction force as the tip-surface separation distance changes. The point indicated by the square shows where the equilibrium position is unstable and the jump to contact occurs.

and

$$F'_{net} = \frac{\partial F}{\partial z_{eq}} = -k + \frac{HR}{3z_{eq}^3} = 0 . \quad (3.9)$$

The jump to contact distance,  $z_{jump}$ , is determined by solving for these two conditions. By substituting Eqn. 3.8 into Eqn. 3.9,

$$-k + \frac{2k(z_o - z_{eq})}{z_{eq}} = 0 . \quad (3.10)$$

An instability results when both conditions are satisfied at the point,

$$z_o = \frac{3}{2}z_{eq} = z_{jump} . \quad (3.11)$$

In order to determine the jump-to-contact distance, the solution to Eqn. 3.9 is substituted back into Eqn. 3.11.

$$z_{jump} = \frac{3}{2} \left( \frac{HR}{3k} \right)^{\frac{1}{3}} \quad (3.12)$$

This condition defines the separation limit below which no interaction can be measured. The jump-to-contact distance depends on the interaction forces between the sphere and surface. This distance is also important because the absolute separation distance between the sphere and the substrate is not known *a priori*. In order to quantitatively describe the interaction forces, it is important to know the absolute surface to surface separation between the sphere and substrate. Assuming that the interaction is purely due to van der Waals forces and that the the tip-substrate geometry is that of a sphere and plane, calculating the jump to contact distance is straightforward.

Another possibility is that the interaction force is not purely van der Waals in origin. As discussed in the previous section, an electrostatic term can arise due to contact charging with the substrate. According to the JKR model for adhesion, the particle will form a finite contact area with the surface. If this region of the dielectric sphere becomes charged, an electrostatic force between the sphere and surface must be accounted for. The interaction which arises can influence the jump to contact behavior, so it must be accounted for.

Accordingly, we have,

$$F_{net} = k(z - z_{eq}) - \frac{HR}{6z_{eq}^2} - \frac{Q^2}{16\pi\epsilon_o(z_{eq} + a_{jkr})^2} = 0 \quad (3.13)$$

and

$$F_{net}' = -k + \frac{HR}{3z_{eq}^3} + \frac{Q^2}{8\pi\epsilon_o(z_{eq} + a_{jkr})^3} = 0 . \quad (3.14)$$

The jump-to-contact distance may be determined by approximating that the contact radius is larger than the separation distance between the two surfaces just prior to the jump,

$$a_{jkr} \gg z . \quad (3.15)$$

The relations for force and force gradient then become,

$$F_{net} \approx k(z - z_{eq}) - \frac{HR}{6z_{eq}^2} - \frac{Q^2}{16\pi\epsilon_o(a_{jkr})^2} = 0 \quad (3.16)$$

and

$$F_{net}' \approx -k + \frac{HR}{3z_{eq}^3} + \frac{Q^2}{8\pi\epsilon_o(a_{jkr})^3} = 0 . \quad (3.17)$$

In which case,

$$z_{eq} \approx \frac{3}{2} \left( \frac{HR}{3(k - \frac{Q^2}{8\pi\epsilon_o a_{jkr}^3})} \right)^{\frac{1}{3}} . \quad (3.18)$$

Using Eqns. 3.12 and 3.18, the separation distance at which jump-to-contact occurs may be calculated. Typical values are given in Table 3.2 which are plotted in Fig. 3.12. A comparison can be made with experimentally measured jump-to-contact distances as shown in Figs. 3.13 and 3.14. The main point is that measuring the jump-to-contact distance gives additional information about the type of interaction which occurs between the sphere and surface. While a pure van der Waals interaction may result in a jump distance of approximately one nanometer for a bare lever, distances on the order of ten nanometers may occur for a charged insulating sphere such as polystyrene.

Due to the approximation, the electrostatic term may actually have a larger effect to the overall jump to contact distance. The effect of the electrostatic contribution will be dependent on the distribution and magnitude of charge.

### 3.2.3 Modeling a Forced Oscillating Lever

Another feature which is important to understand is the behavior of a cantilever when is driven by a sinusoidally varying force. The behavior of such a system will be modified in the presence of a force field which varies with distance. In the case

<b>Jump to contact distances</b>			
Radius	van der Waals (vdW)	vdW + Electrostatic	Measured
1 $\mu\text{m}$	4.4	4.6	–
2 $\mu\text{m}$	5.6	5.8	$4.9 \pm 2.0$
3 $\mu\text{m}$	6.4	6.6	$6.0 \pm 0.5$
4 $\mu\text{m}$	7.0	7.3	$6.1 \pm 0.6$
5 $\mu\text{m}$	7.6	7.9	$7.5 \pm 0.5$
6 $\mu\text{m}$	8.0	8.4	$8.2 \pm 0.7$

Table 3.3

Calculated and measured values for the jump to contact distance for a distribution of polystyrene spheres interacting with a HOPG substrate.

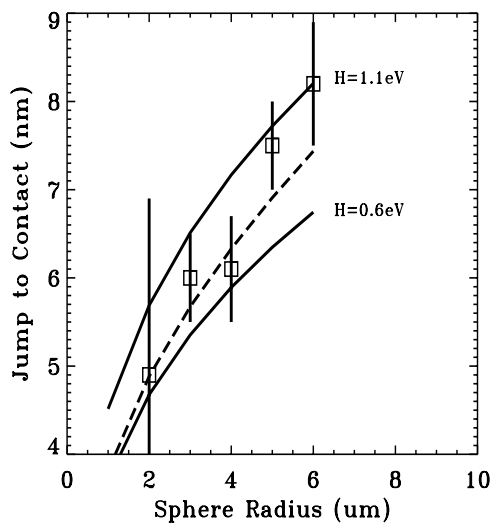


Figure 3.12

Jump to contact data (square) is plotted as a function of sphere radius. A comparison is made between the influence of a purely van der Waals (solid lines) and a van der Waals-Electrostatic (dashed line) interaction. Two van der Waals curves are shown to indicate the range in Hamaker values observed in our measurements. The parameters for the combined interaction curve are:  $Q = 500$  electrons,  $R_{\text{eff}} = a_{\text{JKR}}$ , and  $H = 0.6$  eV.

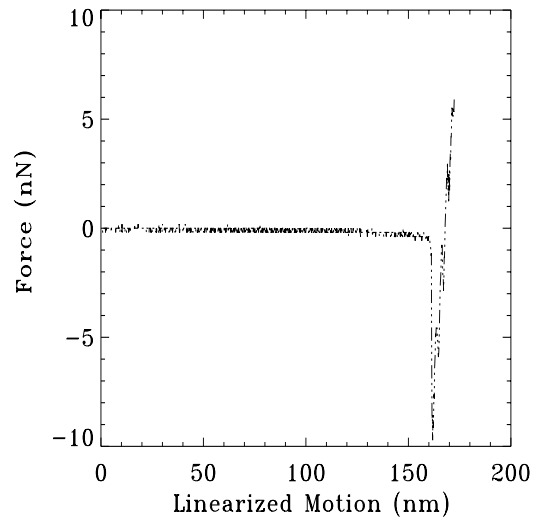


Figure 3.13

Force curve measurement exhibiting a purely van der Waals interaction. The sphere radius is  $3 \mu\text{m}$  and the spring constant is  $2.1 \frac{\text{N}}{\text{m}}$

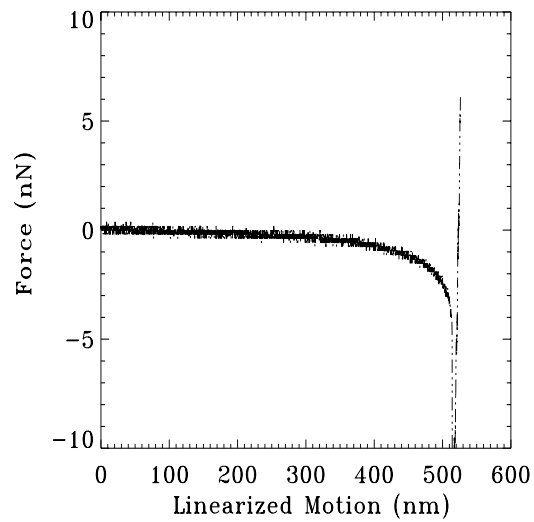


Figure 3.14

Force curve measurement exhibiting both van der Waals and electrostatic contributions. The sphere radius is  $3 \mu\text{m}$  and the spring constant is  $2.1 \frac{\text{N}}{\text{m}}$

of tip-substrate interactions, the motion of the vibrating lever will be modified by the interaction forces between them. By monitoring the vibration of the lever, the force gradient of the interaction can be determined. The equation of motion for the cantilever oscillating at an arbitrary position  $z_o$  from the surface is

$$m\ddot{z} + \gamma\dot{z} - k(z - z_o) + F_{interaction}(z) = F_d \cos(\omega t) . \quad (3.19)$$

A linear expansion can be made of the interaction force for the range of operation

$$F_{interaction} = F_{interaction}(z_o) + \left( \frac{\partial F_{interaction}}{\partial z} \right)_{z_o} (z - z_o) \quad (3.20)$$

so that the equation of motion can be reduced to the form,

$$m\ddot{z} + \gamma\dot{z} - k_{eff}(z - z_o) = F_d \cos(\omega t) + Const. \quad (3.21)$$

where,

$$k_{eff} = k - \left( \frac{\partial F_{interaction}}{\partial z} \right)_{z_o} . \quad (3.22)$$

Assuming that the solution to the equation has the form:

$$z(t) = Ae^{-i\omega t} \quad (3.23)$$

the oscillation amplitude is given by

$$A(\omega) = \frac{A_o}{\sqrt{(\omega^2 - \frac{k_{eff}}{m})^2 + (\frac{\gamma\omega}{m})^2}}. \quad (3.24)$$

Making the substitution

$$\omega_o(z)^2 = \frac{k_{eff}}{m}, \quad (3.25)$$

$$A(\omega) = \frac{A_o}{\sqrt{(\omega^2 - \omega_o(z)^2)^2 + (\frac{\gamma\omega}{m})^2}} \quad (3.26)$$

where the observed resonance frequency of the probe at an arbitrary position away from the surface is

$$\omega_o(z) = \omega_o \sqrt{1 - \frac{1}{m} \left( \frac{\partial F_{interaction}}{\partial z} \right)}. \quad (3.27)$$

This allows a first order approximation of the gradient of the interaction force to be determined by a measurement of the change in resonance frequency with position.

$$\frac{\partial F_{interaction}}{\partial z} = m(\omega_o^2 - \omega_o(z_o)^2) \quad (3.28)$$

or

$$\frac{\partial F_{interaction}}{\partial z} = k \left[ 1 - \left( \frac{\omega_o(z_o)}{\omega_o} \right)^2 \right]. \quad (3.29)$$

From this relation, a comparison can be made with the theoretical models.

## 4. Experimental

### 4.1 Material Properties

#### 4.1.1 Electronic and Physical Properties of Polystyrene

Polystyrene is a man-made polymer used widely in the formation of plastics. Of particular interest is its application to electrophotography. Micron-sized polystyrene particles are used as dry toner in the electrophotographic process. Having a basic understanding of how these particles adhere to a variety of substrates (such as paper) is important. For this reason, it is important to understand the chemical, physical, and electronic properties of polystyrene.

The basic chemical structure of polystyrene is given in Fig. 4.1. The actual molecular weight of polystyrene will vary depending on the fabrication process. The polystyrene used in this study has a molecular weight of  $70,000 \frac{\text{grams}}{\text{mol}}$ .

Table 4.1 gives some common properties

The bead formation process is patented and is, therefore, proprietary. The beads were formed in a process known as "limited coalescence". Essentially the monomer is dispersed in a non-polar solvent such as hexane and the polymer formed by blending in a certain amount of a chemical initiator which forms free radicals at the ends of the chain. There is also a certain amount of reaction terminator,

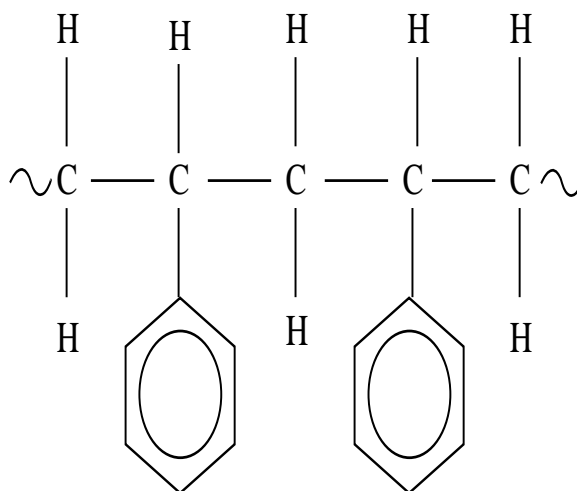


Figure 4.1

Chemical Structure of Polystyrene.

Typical Properties of Polystyrene	
Property	Value
Heat Capacity	$127.38 \frac{J}{mol \cdot K}$
Glass Transition Temperature	100 °C
Compressive Modulus	2550 MPa
Density	$1.04 \frac{g}{cm^3}$
Dielectric Constant	2.49-2.61
Hamaker Coefficient	1.9 eV

Table 4.1

Physical and Electrical properties of Polystyrene.

which will react with free radical ends to terminate the reaction. Obviously, the longer the chains, the fewer the chain ends available so the higher the probability that the terminator will stop the reaction. This limits the molecular weight of the polymer. The polymer solution is also dispersed in an aqueous medium and would, therefore, tend to coalesce into a large mass. However, by adding sub-micrometer particles such as silica, the tendency to coalesce is limited, hence the name. By varying the silica concentration, the size of the particles is controlled. The particles are then dried and the silica is removed by washing in a concentrated solution of KOH. They are then rinsed to neutral pH in distilled water and dried.

The spheres are very uniform, but are not atomically smooth. The asperity height as measured using an AFM is approximately 20 nm. Contact AFM scans have been made of the surface of the polystyrene spheres to better understand the morphology of the surface (See Fig. 4.2). It is clear that the actual structure of the surface can be rough, which would influence adhesive properties when the particle makes contact with other surfaces. In particular, the circular region outlined on the image indicates the theoretical contact area a spherical particle with radius of  $4\mu\text{m}$  would make with an HOPG surface. The regions outlined within the circle are the asperities which would actually make contact with the surface under zero load. It is clear that the true contact area can be significantly less than expected. This would result in adhesion forces smaller than expected.

The electronic properties are also important when discussing charge transfer later on. In the case of polymers, it is necessary to define donor/acceptor states.

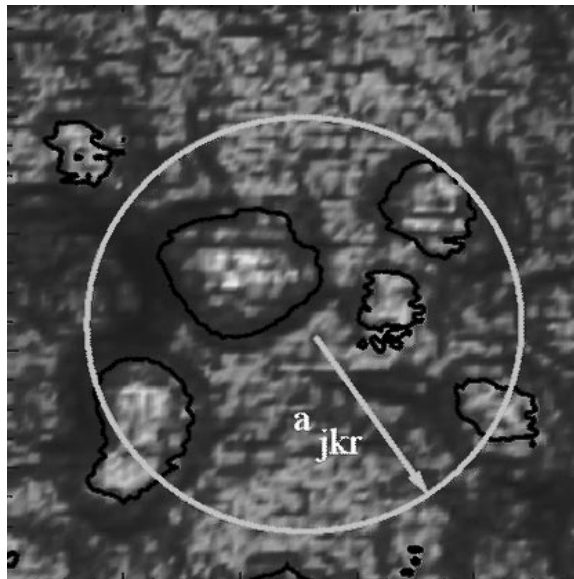


Figure 4.2

Surface roughness effects of polystyrene spheres.

The question which has yet to be clearly defined is whether charging occurs from trapped bulk or surface states. These states exist between the conduction band edge and valence band edge as shown in Figure 4.3. Polystyrene materials have approximately  $10^{21} - 10^{22}$  trapped states per cubic meter.

Polystyrene is a series of carbon and hydrogen bonds attached to benzene rings. The energy of an electron associated with an isolated benzene ring is nearly zero. If the benzene ring is attached to a carbon chain that is surrounded by other chains, the electron energy will be several electron volts below vacuum level. Due to the variety of chain combinations with benzene rings, a wide range of energy states will occur for a given form of polystyrene. While there is a band of donor/acceptor energy states, each individual state is localized such that electrons cannot be easily

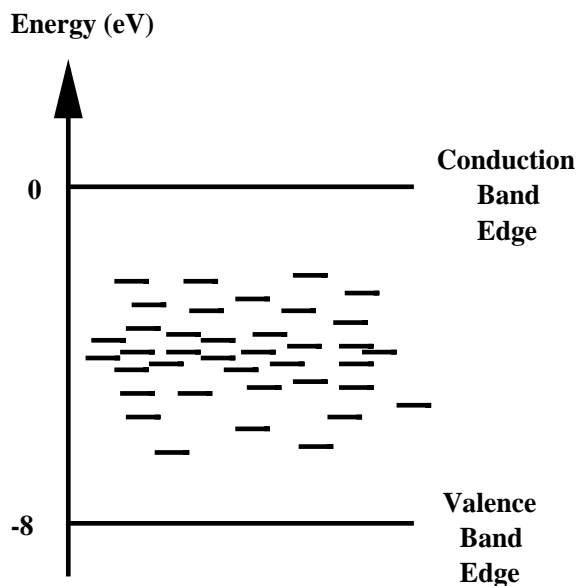


Figure 4.3

Donor-Acceptor levels in Insulators.

transferred. This electron localization is associated with the electron energy range on benzene rings. An electron on one benzene ring may not be transferred to a neighboring benzene ring because the energy of the neighboring orbital is different and cannot be achieved from thermal energy. Duke and Fabish discuss this model for a wide energy spread in polymers in greater detail.[31] For polystyrene, these bands of electron states occur at around 4 eV below the conduction band.

An important point to consider with polymers such as polystyrene is the formation of free radicals. They can arise from bond breaking through specific treatment of the polystyrene, or from contact with another surface. Free radicals may act as electron acceptors in contact electrification, but little experimental information is available.[32] This will be addressed to some extent in a later section.

#### 4.1.2 Electronic and Physical Properties of Highly-Oriented Pyrolytic Graphite

Elemental carbon occurs in many forms in nature. Of particular interest in this study is the graphite form of carbon. Recently developed processes allow for the fabrication of highly oriented pyrolytic graphite. The pyrolytic production of graphite is performed using carbonaceous vapors. In this process, a stream of gas is passed over a substrate which is heated to a high temperature. With these conditions, very pure carbon is deposited in a variety of structural forms. The forms of carbon deposited depends on the gas composition and pressure as well as the temperature and temperature gradients of the substrate. Under the appropriate conditions, the deposition will be of highly oriented carbon layers. This highly oriented form of graphite is reached by heating the pyrographite to temperatures ranging from 2800-3000 degrees centigrade. Layers may form into large slabs of pure and perfect single crystals. The crystalline-layered material is referred to as highly oriented pyrolytic graphite.[33] It is the closest in structure to perfect single-crystal graphite as shown in Fig. 4.4. The structure of graphite is that of a regular network of hexagons. X-ray studies indicate that mono-crystalline graphite forms parallel layers which are separated by  $d_o = 0.33538$  nm. The spacing between interplanar carbon atoms is  $a_o = 0.1415$  nm. These interplanar layers are structurally independent from one another and are easily cleaved to expose new layers. The stacking sequence of the layers can be either hexagonal with ABAB sequencing, or face-centered cubic with ABCABC sequencing. In this particular study, the graphite has ABAB sequencing.

Extensive studies have been made of the crystalline graphite band structure using a variety of methods.[34, 35]. The Brillouin zone of graphite is a regular hexahedron as shown in Figure 4.5.

The symmetry labels indicated as H,K,L,M, and  $\Gamma$ , are used to calculate the occupied and unoccupied bands. The details of such calculations can be found elsewhere.[34, 35] It is important to understand the band structure of HOPG. Only by understanding the band structure is it possible to determine the Fermi surface and which bands contribute to charge transfer.

It is easiest to consider a two dimensional graphite surface. In this case, there will be three valence bonds between an atom and its nearest neighbors due to the  $sp^2$  orbitals which are referred to as  $\sigma$ -bonds. The remaining orbital extends perpendicular to the basal planes, and is responsible for  $\pi$ -bonds. It is the  $\pi$ -bonding which allows charge transfer in HOPG, so conduction is highest perpendicular to the basal planes. The work function of HOPG has been reported to be between 4.5-4.9 eV.[33]

HOPG is useful in scanning probe microscopy because it has hexagonal periodicity which can be used for calibration of the system. In this study, HOPG provides an atomically smooth surface for making force and force gradient measurements with micrometer-sized polystyrene spheres. Also, because it is electrically conducting as well as chemically inert, it is an ideal substrate for performing long-range force and contact electrification measurements.

The reliability of the experimental apparatus is illustrated by adhesion mea-

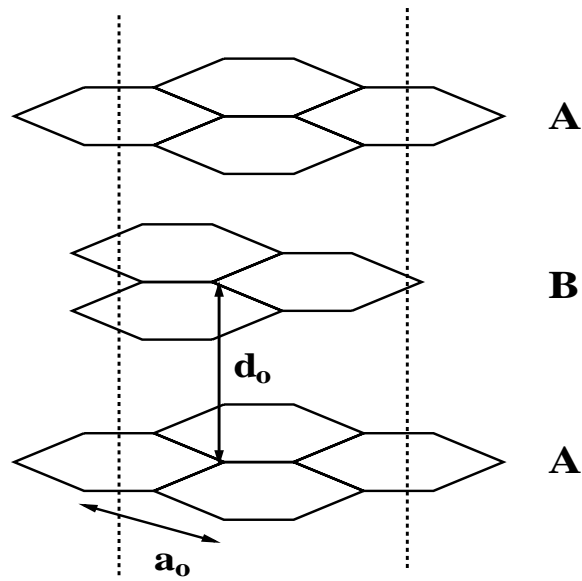


Figure 4.4

Three dimensional structure of highly oriented pyrolytic graphite. The interplanar spacing  $d_o$  is 0.33538 nm. The spacing between carbon atoms,  $a_o$  is 0.1415 nm.

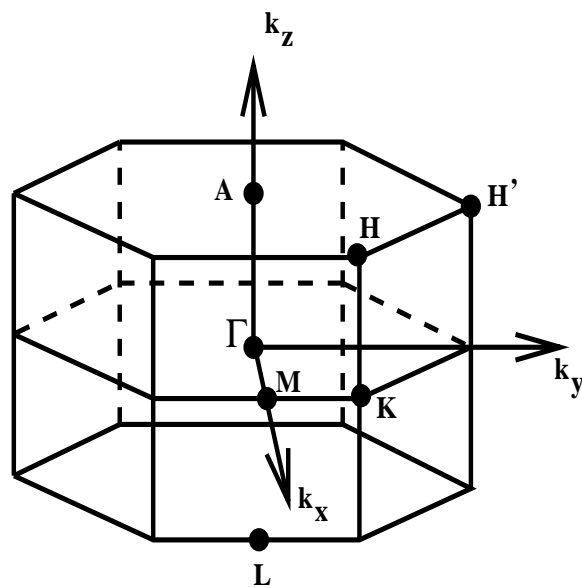


Figure 4.5

Brillouin zone for three dimensional crystalline graphite.

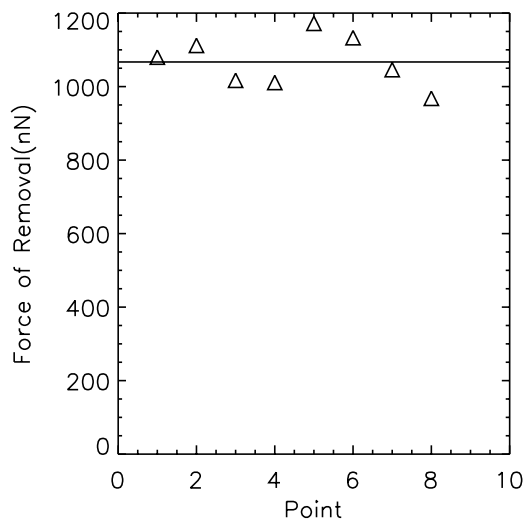


Figure 4.6

## Control Measurements on HOPG

measurements performed between a  $9\ \mu\text{m}$  diameter polystyrene sphere and freshly cleaved HOPG surface. Measurements at eight different locations on the surface were performed after purging the system with dry nitrogen several times at 8 different locations on the surface. As shown in Table 4.2, the results are very reproducible with little variation over the surface (see Figure 4.6). Based on the JKR model for adhesion (see Eqn. 2.32), the force of removal should be 2306 nN. This discrepancy is possibly due to the surface of the polystyrene being rough, which can reduce the actual contact area that is made with the HOPG surface as discussed in the previous section. The important point is that the measured values are consistent.

Table 1: Lift-Off Data		
Point	Removal Force (nN)	Uncertainty (nN)
1	1080.	9.
2	1112.	4.
3	1017.	7.
4	1172.	3.
5	1011.	10.
6	1133.	5.
7	1046.	11.
8	968.	6.

Table 4.2

Force of removal reference measurements between a 9  $\mu\text{m}$  polystyrene sphere and freshly cleaved HOPG surface.

## 4.2 Calibrating AFM Cantilevers

To determine quantitative information about the interaction force between a sphere and flat surface, it is necessary to know the spring constant of the cantilever. As discussed earlier, there are two methods which can be used to calculate the spring constant of the lever. One method, outlined by Sarid [36] and discussed earlier, uses the geometry of the lever and the elastic modulus to calculate the spring constant. The second method entails the measurement of the resonant frequency of the cantilever.[30] The second method does not require that the thickness of the lever be known, a quantity which can be difficult to measure accurately. The latter method has a higher degree of accuracy because the resonant frequency can be more easily measured than the thickness of a cantilever. Figure 4.7 shows a schematic of the procedure used in performing the resonant frequency measurement.

A lock-in amplifier is used to compare the amplitude of the reference signal with the response of the oscillating lever. As the frequency is ramped through resonance, the output from the lock-in indicates at what frequency resonance occurs. The measurements are performed under low vacuum ( $\sim 10$  mTorr) to minimize atmospheric effects to the resonance peak.[37] This technique gives a sensitivity of less than a Hertz in frequency measurement.

In addition to the spring constant, it is also necessary to calibrate the deflection signal measured by the photodiode for a known displacement. This gives the appropriate calibration required to determine the lever deflection in nanometers which

## AFM CONFIGURATION

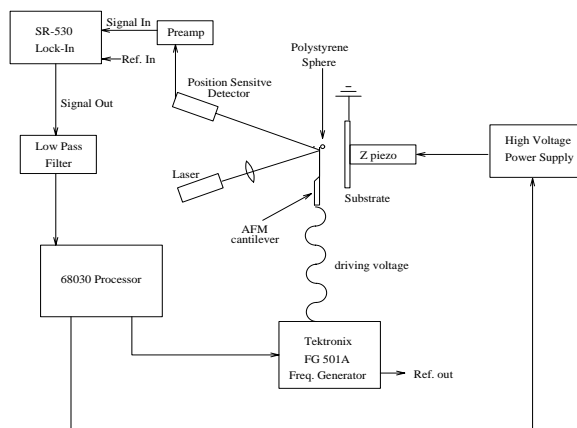


Figure 4.7

Procedure for performing resonance frequency measurement.

is important when performing quantitative measurements. A sapphire substrate is pressed against the cantilever to perform this calibration. Since sapphire has a larger elastic modulus than silicon, it is assumed that the cantilever will undergo an elastic compression. Since the sample piezo is already calibrated, the voltage response of the detector measuring the lever deflection can be interpolated to a displacement in nanometers (see Fig. 4.8). The piezo tube is already calibrated in x, y, and z directions. The z calibration constant is  $4.65 \frac{nm}{V}$ . Another critical parameter to know is that the analog signal is converted to a digital signal using a 16 bit D/A board. The input voltage which can be read is  $\pm 10V$ . This corresponds to a resolution of  $0.305 \frac{mV}{step}$ . Using these two important conversions along with the voltage calibration constant, the data may be converted into nanometers as shown

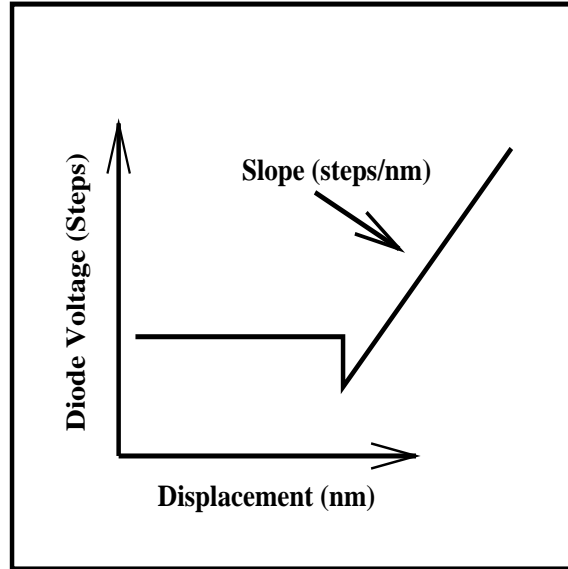


Figure 4.8

Voltage calibration.

below. The *slope* referred to in Eqn.4.1 is that of the raw photodiode data plotted versus applied sample tube voltage.

$$Data(nm) = Data(steps) \times (Z - gain) \times (slope \frac{V}{steps}) \times (4.65 \frac{nm}{V}) \quad (4.1)$$

Once the deflection data has been converted to nanometers, multiplying by the spring constant of the cantilever will give the force.

### 4.3 Mounting micron spheres to cantilevers

In order to mount micrometer sized spheres to the AFM cantilevers it is necessary to overcome several obstacles. Two major considerations are sphere manipulation and adhesion of the sphere to the cantilever. In order to select spheres in

the micrometer size range, it is necessary to use a high powered optical microscope with a large focal length. The large focal length is required to allow sufficient working space to select and mount spheres to cantilevers.

Several methods were developed to select micron-sized objects. The most successful methods involved the fabrication of fine needle-like probes made either by etching tungsten wire or glass capillary pipettes. In the case of tungsten wire, sub-micrometer tips were made using etching techniques identical to those used in making FEM and STM tips. The second method is to take 2mm o.d. glass capillary tubes and extrude sub-micron tips from them using a fine propane torch. The capillary whiskers are shown in Figure 4.9. Care must be taken to clean the capillary whiskers or tungsten probes with distilled water and acetone in order to remove any microscopic contaminants or glue.

To fix a micron-sized object to the end of the cantilever, a proper adhesive material must be selected. The characteristics required are that it be viscous enough to ensure the glue does not encapsulate the object mounted, and secondly, that the glue has a slow curing time. The two bonding agents used were a 24 hour cure epoxy (Miller-Stephenson Epoxy 907) and Norland 68 UV cure glue. Another method for mounting polystyrene spheres was to heat the spheres above the glass transition temperature of polystyrene. This method proved to be unreliable because the spheres would either form a weak bond or would undergo plastic flow.

The first step in the mounting process is to use a probe to apply a small amount of adhesive to the cantilever. A micromanipulator stage (Goodfellow Technology)

is used to bring the probe into proximity to the cantilever under the microscope (see Figure 4.10). The manipulator allows one to apply the adhesive in a controlled manner. Once this step is performed, a second probe is used to select the micron-sized object of interest. Micrometer-sized material appears powder-like in bulk amounts. A small sample is placed on a glass slide which is cleaned using methanol and de-ionized water. The glass slide is tapped several times to remove excess material and form an even distribution over a region of the glass slide. The glass slide is then placed under the microscope to select a particular size sphere. A video camera and monitor are hooked to the microscope to give an overall magnification of a  $1000\times$ . A second probe is placed on the micromanipulator to select the spherical particle. Once a particle with the correct size and shape is chosen, the probe is brought directly above the micron-sized object and is picked up by capillary forces. With the object still on the probe, the cantilever is placed back under the microscope. The probe is then lowered over the desired location on the cantilever to where the object is then transferred. Because the area to which glue is applied is small (typically  $\sim 1 \mu\text{m}^2$ ) there is no bleeding over the mounted object. The entire mounting process is shown in Figures 4.11 (a-f). The entire process typically takes approximately 15-30 minutes.

To determine the accuracy of the mounting, the stage on which the cantilever is held can be rotated so different perspectives may be viewed. The choice of glue and manipulation technique allows for the removal of the object if an adequate orientation is not achieved. Once an object is mounted sufficiently, the glue is

cured. In the case of the UV cure glue, the cantilever is placed under a UV lamp for 30 minutes. If the epoxy is chosen, the glue is allowed to cure for a 24 hour period. Once the curing has finished, the particle is checked to determine if it is secure using a clean probe. This is done by using the probe to press on the sphere until a small cantilever deflection is observed.

#### 4.4 Force Measurement Technique

The atomic force microscope (AFM) operates in the regime where both van der Waals and electrostatic forces are dominant. It is because of this feature that the AFM has become such a useful tool for imaging the surface of materials not accessible by scanning tunneling microscopy.

As has been described previously, the AFM can image surfaces by monitoring the deflection of the cantilever due to the interaction forces between the cantilever's tip and the sample surface. Since the radius of curvature of the tip is typically on the order of a 10 nm, the dominant interaction is from van der Waals forces. The van der Waals interaction will dominate over electrostatic because on this size scale, the charge which can be maintained does not produce as large a force of attraction. It has previously been shown that the van der Waals forces for such macroscopic objects are geometry-dependent. If the tip is taken to have a parabolic shape, the expected interaction will follow a  $\frac{1}{z^3}$  power law dependence with a flat surface. By changing the geometry of the tip, the behavior of the interaction force will change. If a sphere is mounted on the end of the lever, it will become the

effective tip. As found in Table 2.2, the power law dependence would then become  $\frac{1}{z^2}$ . Another point to consider is that with the spheres used in this study, this size is dramatically larger than the bare tips initially on the cantilevers. The result is that along with van der Waals forces, electrostatic forces can become a significant contribution to the resulting interaction force.

The process in making a static force measurement is to monitor the deflection of the cantilever. It has already been discussed how the cantilever acts as a spring. Under the influence of an interacting force, the spring will deflect so as to oppose this change as described by Hooke's law. By monitoring this deflection as a function of tip to surface separation, the net force as a function of separation distance can be measured.

The ability of measuring forces in this way has two fundamental limitations. The first limitation is the sensitivity of the cantilevers. The cantilever's spring constant defines the amount of deflection which will occur as a result of a force. It is ideal to select levers which have minimal sensitivity to thermal or vibrational noise. However, this also will set a limitation as to the forces which can be directly measured. Van der Waals forces may act over long ranges (1-100 nm), but the detection of the cantilever's deflection may occur near the second limiting factor known as the jump-to-contact phenomena.

An intrinsic difficulty with making force measurements with the AFM cantilevers is that they will experience a phenomena known as the jump to contact. The jump to contact occurs when the interaction forces acting between the tip and

surface become large enough that the levers displacement in response to the force becomes unstable. As a result, the lever will jump into contact with the surface. The separation at which point this occurs will depend on the tip-surface geometry and the material properties of the tip and surface as discussed in an earlier section.

These two limitations make it difficult to measure pure van der Waals forces. As a result, a more sensitive technique is required to measure the interactions between the tip and surface. This second technique discussed in the following section, measures the interaction force gradient. Not only does it provide a higher degree of sensitivity to the interactions, but it also gives an independent check to the results provided by the force sensing technique.

#### 4.5 Force Gradient Measurement Technique

In addition to measuring forces directly, the AFM can be used to detect the interaction force gradient between the tip and surface. This feature is beneficial for determining the validity of the force measured. Not only does this provide a second interaction measurement technique, it is also provides more sensitivity. In fact, this dynamic mode of operation gives enough sensitivity to observe the transition between electrostatic and van der Waals interactions. So while the van der Waals force between micrometer-size spheres and flat substrates is difficult to measure directly using an AFM, the measurement of the force gradient allows for its detection.

The interaction force gradient between the tip and surface can be determined

directly using the dynamic mode of AFM operation. From Eqn. 3.29 it is possible to measure the force gradient as a function of surface to surface separation distance by monitoring the shift in frequency. As explained in an earlier section, the shift in frequency is caused by the influence of the interaction force, resulting in an effective spring constant of the lever. Figure 4.7 illustrates how this shift in frequency is monitored. Using a function generator, a sine wave is used to oscillate the cantilever. The frequency is swept about the known resonance as a function of surface-surface separation. The oscillation of the lever is kept below a nanometer. The procedure is identical to the technique used to measure the resonance frequency of the cantilever. The only difference is that the measurement is performed as a function of separation distance from the sample. The benefit over an amplitude modulation technique is that the interaction force gradient is not interpolated from the amplitude equation. Also, because the measurement is of a frequency, a high degree of precision and resolution is obtained. This is accomplished by fitting the frequency data to Eqn. 3.26 which yields sub-Hertz resolution of the resonance frequency. The program used to perform the fit is found in Appendix A. Although a fit is only performed to first order, there is little disagreement with theoretical predictions.

As in the case of measuring the interaction force, the total separation distance between the sphere and surface is not known *a priori*. The jump to contact distance is necessary in this measurement to define the absolute surface to surface separation distance between the tip and substrate. Since the cantilever is driven with a

sinusoidal oscillation amplitude of under a nanometer, there is a finite uncertainty in the total separation distance. Although this driving amplitude decreases with the separation distance, the zero reference point is only known to within  $\pm 0.5$  nm. With this information, the force gradient can also be determined as a function of position.

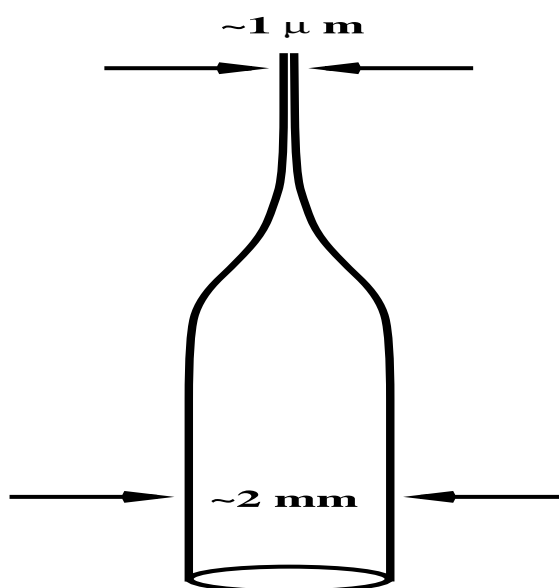


Figure 4.9

The capillary pipettes are extruded to sub-micrometer tips in order to both apply glue, as well as to mount small particles.

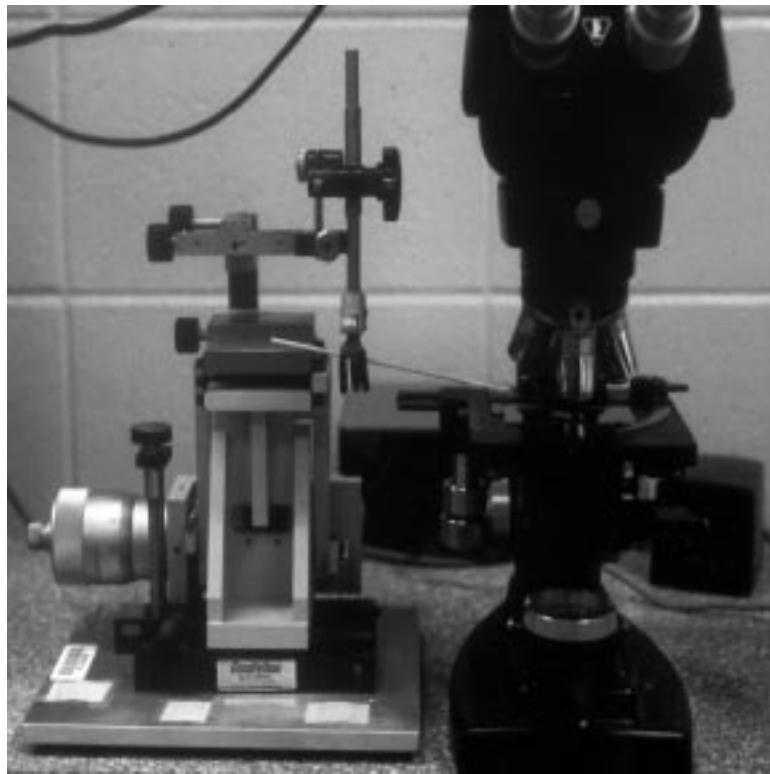


Figure 4.10

Micromanipulator set-up used to perform sphere mounting.

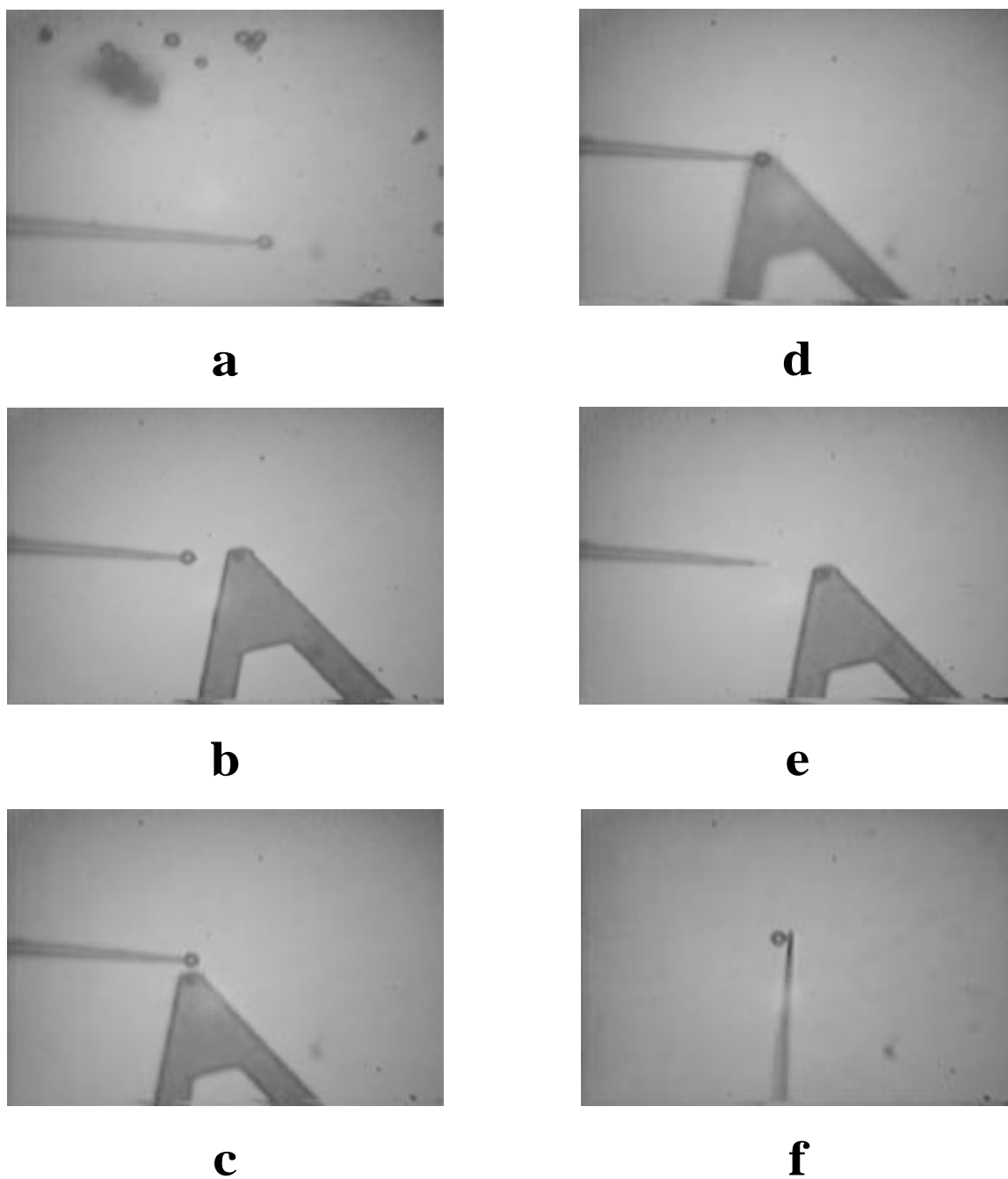


Figure 4.11

The process is as follows: a) Selection of sphere; b) Focus on cantilever to which sphere is to be mounted to; c) Bring sphere into range of the cantilever; d) Placement of sphere onto cantilever; e) Withdraw capillary whisker; f) Check the placement of sphere on cantilever.

## 5. Measured Interaction between Polystyrene Spheres and HOPG Substrate

### 5.1 Theoretical Considerations

The interaction force and force gradient between a micron-size polystyrene sphere and an atomically flat highly oriented pyrolytic graphite substrate has been analyzed as a function of surface-to-surface separation distance  $z_o$ . The two techniques used to measure the force (static mode) and force gradient (dynamic mode) will be discussed in the following sections. Both measurements give important information about the interaction between the particle and surface. The static mode measurement offers explicit information about the interaction force, while the dynamic mode measurement provides information about the interaction force gradient. While the force gradient is not a physically important quantity, the parameters required to fit this data should be consistent with parameters used to fit force measurement data. Dynamic mode measurements also provide a higher degree of sensitivity to the interaction.

As will be discussed in a later section, the force gradient measurement provides a highly sensitive technique to measure the long-range interactions between the particle and surface. Initial attempts to use an amplitude modulation technique[38] in which the cantilever was driven at a frequency  $\omega$  just off the resonance frequency

$\omega_\infty$ , were abandoned in favor of the frequency measurement technique,[14] which provides a direct method for calculating the interaction force gradient.

$$\frac{\partial F_{inter}}{\partial z} = k \left[ 1 - \left( \frac{\omega_o(z_o)}{\omega_\infty} \right)^2 \right]. \quad (5.1)$$

From this relation, a comparison of the inferred  $\frac{\partial F_{inter}}{\partial z}$  can be made to theoretical models.

Initially, attempts were made to fit the force and force gradient data using only a van der Waals interaction. All fits were found to have too short a range and were incapable of fitting the data at large separation distances. As a consequence, other forces were examined, and ultimately a combination of forces were required to accurately describe the data. As a result of this analysis, it was concluded that for small separations ( $z \leq 30$  nm), a van der Waals interaction between a sphere and a flat plane, described by

$$F_{vdw} = -\frac{HR}{6z_o^2}, \quad (5.2)$$

$$\frac{\partial F_{vdw}}{\partial z} = \frac{HR}{3z_o^3}, \quad (5.3)$$

fits the data quite well. Here, H is the Hamaker constant, R is the sphere radius, and  $z_o$  is the surface-to- surface separation distance.

For larger separations, a long-range electrostatic force is required to understand

the data. The origin of this electrostatic force is twofold. First, there are charges trapped around the perimeter of the polystyrene sphere. The surface charge density  $\sigma$  for these charges is  $\sim 10^{-9} \frac{\text{C}}{\text{cm}^2}$  as determined from independent Faraday cage measurements of the trapped charge on an ensemble of polystyrene spheres. A second contribution is the trapped charge that is likely to form on the bottom of the insulating polystyrene sphere when it jumps-to-contact with the substrate during the course of our measurements. It is interesting to further discuss the distribution of this charge, which is triboelectrically generated during the jump-to-contact of the sphere to the substrate.

When the sphere is in contact with the substrate, charge is free to flow in order to minimize the contact potential difference. In addition, the sphere deforms due to surface forces and touches the substrate over a finite area. The radius  $a_o$  of this contact area can be estimated from the Johnson-Kendall-Roberts (JKR) theory, which analyzes the elastic deformation of a spherical object resting on a flat substrate.[20] This model has been successfully applied to studies of the deformation of micron-size spheres resting on substrates.[39, 40] A well-known prediction of the JKR theory relates the radius of the contact at zero applied load,  $a_o$ , to the elastic properties of the sphere by

$$a_o = \left( \frac{6\pi R^2 W}{K} \right)^{\frac{1}{3}}, \quad (5.4)$$

where  $R$  is the sphere's radius,  $W$  is the work of adhesion given by

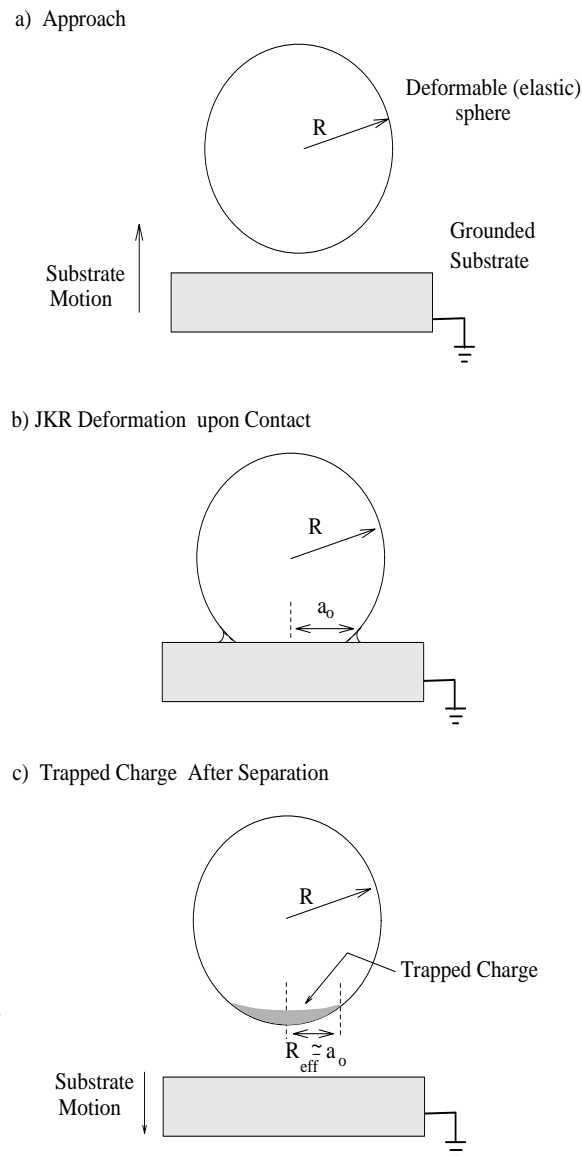


Figure 5.1

The relevant parameters to describe triboelectric charging of the polystyrene sphere upon contact and removal from an atomically flat HOPG substrate. In (a) a sphere of radius  $R$  approaches the HOPG substrate. Upon contact (b) the sphere deforms due to surface forces between the sphere and substrate, which cause a contact area to form with radius  $a_0$ . While in contact, charge transfer between the grounded substrate and the sphere takes place. After separation (c), the excess charge remains localized at the bottom of the sphere over a region with radius  $R_{\text{eff}} \simeq a_0$ .

$$W = \gamma_{\text{ps}} + \gamma_{\text{HOPG}} - \gamma_{12} \quad , \quad (5.5)$$

where  $\gamma_{12} \simeq 2\sqrt{\gamma_{\text{ps}}\gamma_{\text{HOPG}}}$  and  $\gamma_{\text{ps}}$  and  $\gamma_{\text{HOPG}}$  are the surface-free energies of polystyrene and HOPG, respectively. The parameter  $K$  includes the elastic properties of the sphere and substrate and is given by

$$K = \frac{4}{3} \left( \frac{1 - \nu_{\text{ps}}^2}{E_{\text{ps}}} + \frac{1 - \nu_{\text{HOPG}}^2}{E_{\text{HOPG}}} \right)^{-1} . \quad (5.6)$$

Here,  $\nu_{\text{ps}}$  and  $\nu_{\text{HOPG}}$  are the Poisson ratios of polystyrene and HOPG, respectively, and  $E_{\text{HOPG}}$  and  $E_{\text{ps}}$  are the Young's moduli for HOPG and for polystyrene. Values for these quantities can be found in the literature.[41]

The electrostatic force between a grounded plane and a charge distributed over a sphere of radius  $R$  is discussed by Smythe.[42] For the case of a sphere of radius  $R$  at a potential  $V$ , whose center is located a distance  $(z + R)$  from a grounded, conducting substrate, the force is given by

$$F_{\text{el}} = -2\pi\epsilon_0 a_0^2 V^2 \left[ \frac{1}{2(z + R)^2} + \frac{8R(R + z)}{[4(R + z)^2 - R^2]^2} + \dots \right] . \quad (5.7)$$

The first term in this equation describes the force between a grounded conducting plane and a uniform charge distribution frozen in place on a sphere. The higher order terms describe polarization effects that result when the sphere is moved closer to the plane. If the charges are trapped, as is the case here, only the first term is required. The potential of the sphere can be related to the charge  $Q$  on the sphere

in the usual way, using the capacitance  $C$  of a sphere of radius  $R$  whose center is suspended a distance of  $R + z$  above the plane

$$C = \frac{Q}{V} = 4\pi\epsilon_o R[1 + r + \dots], \quad (5.8)$$

where  $r = R/2(R + z)$ . Combining Eqns. 5.6 and 5.7 and taking the derivative provides an analytical expression for the force gradient due to electrostatics.

Attempts to fit the data using a uniform charge distribution trapped around the perimeter of the entire sphere produces a force gradient too small to fit the data. This result follows because, for the spheres used in this study,  $R \gg z_o$ . This led us to consider triboelectrically produced charges trapped at the bottom of the sphere. In this regard, it was assumed that upon jump-to-contact of the sphere to the substrate, a region of the sphere of radius  $\sim a_o$  (see Eqn. 5.4) makes contact with the substrate and becomes locally charged. Upon withdrawal, this charge resides in a spherical region of size  $R_{eff}$  where  $R_{eff} \simeq a_o$ . This charge remains trapped at the bottom of the sphere in the vicinity of the contact region. This situation is illustrated schematically in Fig. 5.1. Under these circumstances, the electrostatic force is determined by modeling the trapped charge as a spherically symmetric distribution of radius  $R_{eff} \simeq a_o$ .

Representative plots of the dependence of these forces for a  $3 \mu\text{m}$  radius sphere are given in Fig. 5.2. In this figure, the force and force gradient are plotted as a function of separation for three limiting cases: (i) van der Waals interaction

(no electrostatic contribution), (ii) uniformly charged sphere plus van der Waals contribution, and (iii) a localized charge density located at bottom of sphere plus a van der Waals contribution. For the case of a uniformly charged sphere, the constant force resulting for surface-to-surface separations greater than  $\sim 200$  nm would be nulled out during the initial alignment of the cantilever when far from the substrate. Measurements of the interaction force may contain contributions from all three of these cases and a linear superposition must then be performed to best fit the data. In this case, the well-defined power law dependence of the van der Waals contribution for small surface-to-surface separations is a valuable signature for determining the cross-over from an electrostatic interaction.

The determination of the best parameters to fit the data is facilitated by the fact that Eqn. 5.2 is dominant for small sphere-substrate separations, while Eqn. 5.7 is important for larger values of  $z$ . We find no need to include retardation effects in this discussion because optical absorption measurements on polystyrene show a strong absorption around 300 nm. This wavelength defines the transition region between retarded and nonretarded van der Waals interactions; however, the electrostatic interaction dominates in this transitional region.

## 5.2 Interaction Force Gradient vs. Sphere Radius

Experiments were performed to determine if the interactions scale correctly with sphere radius as specified by the proposed model describing the interaction. While the interaction is due to a combination of van der Waals and electrostatic

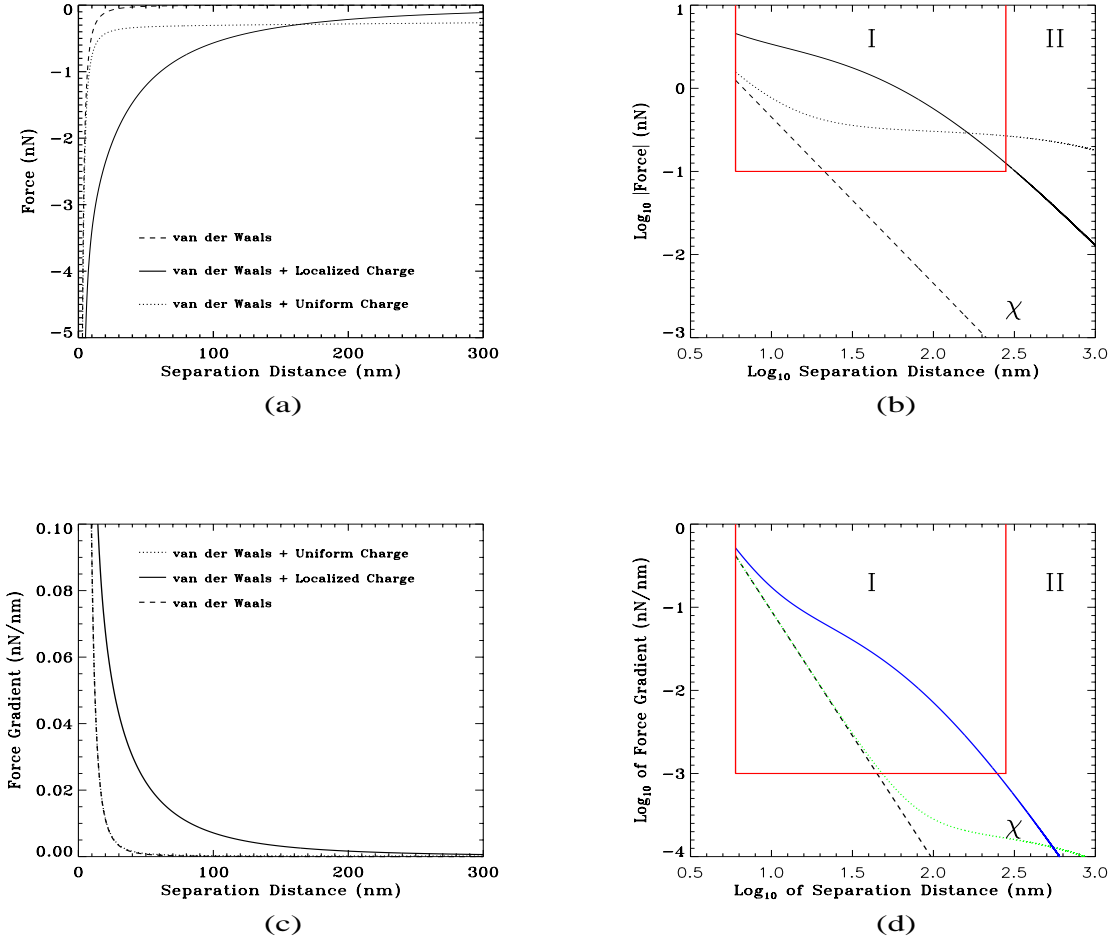


Figure 5.2

Plots of the spatial dependence of the interaction force and interaction force gradient. In (a) and (b), the dashed line indicates the contribution of a van der Waals interaction alone. The other lines illustrate electrostatic contributions to the net interactions from either a uniform (dotted line) or localized (solid line) charge distribution. In (c) and (d), logarithmic plots of force and force gradients for a pure van der Waals interaction (dashed line), and for electrostatic contributions from either a uniform (dotted line) or localized (solid line) charge distribution. The plots emphasize the nature of the electrostatic contribution to the net interaction. The region enclosed by the dotted box shown in both plots indicates the experimental limit of our instrument. Regions labeled I and II separate the non-retarded and retarded limits of the van der Waals interaction. The absorption wavelength of polystyrene is given by  $\chi$ . The parameters used in generating the plots are:  $R = 3 \mu\text{m}$ ;  $R_{\text{eff}} = 57 \text{ nm}$ ;  $Q = 500$  electrons; and  $H = 0.6 \text{ eV}$ .

forces, the measured interactions should scale with radius at short range ( $\leq 30$  nm). Measurements were performed using the dynamic mode of operation because of the increased sensitivity of this technique.

As described in the previous section, the dynamic mode of operation measures force gradients by monitoring the shift in the resonant frequency of the cantilever. The resonant frequency (and oscillation amplitude) decrease as the interaction between the sphere and surface increases. Representative data showing this shift in frequency and reduction in oscillation amplitude are shown in Fig. 5.3.

Fitting Eqn. 3.26 to this data, it is possible to accurately determine  $\omega_o(z)$  and to calculate  $k \left[ 1 - \left( \frac{\omega_o(z_o)}{\omega_\infty} \right)^2 \right]$ . The logarithm of this quantity is plotted in Fig. 5.4 (a) and (b) for 3 and 6  $\mu\text{m}$  radius polystyrene spheres as a function of the sphere-substrate separation distance  $z_o$ .

The fits to the experimental data are shown by the dashed lines in Figs. 5.4 (a) and (b). The parameters  $Q$ ,  $R_{eff}$ , and  $H$  were adjusted until reasonable agreement with the data was obtained. The parameters determined in this way are given in Tables 5.1 and 5.2.

Based on the models used, there is good agreement between expected and fitted values for each parameter. The value used for the Hamaker coefficient for each sphere agrees closely with the expected value determined using the modified Lifshitz model for the van der Waals interaction between polystyrene and graphite.[43] The radius of each sphere as measured using a  $1000\times$  optical microscope is consistent with the values used when fitting the data for each sphere. A factor of two

<b>3 <math>\mu\text{m}</math> radius Sphere</b>		
Parameters	Expected Values	Fitted Values
H	1.1 eV*	1.0 eV
R	3.0 $\mu\text{m}$	3.0 $\mu\text{m}$
$R_{eff}$	160nm <sup>†</sup>	80 nm
Q		400 e <sup>-</sup> 's
$\sigma$	$\sim 10^{-9} \frac{C}{cm^2}$ <sup>‡</sup>	$8 \times 10^{-8} \frac{C}{cm^2}$

\* Interactions between polystyrene and graphite.[43]

<sup>†</sup> Contact radius based on JKR Model.

<sup>‡</sup> Faraday cage measurement of charge on an ensemble of polystyrene spheres.[44]

Table 5.1

Force gradient parameters for 3  $\mu\text{m}$  radius polystyrene sphere interacting with freshly cleaved HOPG surface.

<b>6 <math>\mu\text{m}</math> radius Sphere</b>		
Parameters	Expected Values	Fitted Values
H	1.1 eV*	1.0 eV
R	5.5 $\mu\text{m}$	6.0 $\mu\text{m}$
$R_{eff}$	270nm <sup>†</sup>	140 nm
Q		700 $e^-$ 's
$\sigma$	$\sim 10^{-9} \frac{C}{cm^2}$ <sup>‡</sup>	$5 \times 10^{-8} \frac{C}{cm^2}$

\* Interactions between polystyrene and graphite.[43]

<sup>†</sup> Contact radius based on JKR Model.

<sup>‡</sup> Faraday cage measurement of charge on an ensemble of polystyrene spheres.[44]

Table 5.2

Force gradient parameters for 6  $\mu\text{m}$  radius polystyrene sphere interacting with freshly cleaved HOPG surface.

discrepancy exists between the expected and fitted values for the effective radius presumably because the JKR model does not account for such factors as surface roughness. The discrepancies between expected and fitted charge distributions,  $\sigma$ , occur because the Faraday cage measurement values are an average over a large ensemble of polystyrene spheres.

### 5.3 Force and Force Gradient-Consistency Check

Interaction measurements were performed using the two AFM techniques previously described. Measuring both the interaction force and interaction force gradient provides a self consistent check of the parameters used in the proposed model. In this study, we revisit the interaction forces acting between an individual insulating spherical particle and a grounded, conducting substrate using two independent techniques. In this way we are better able to assess the reliability of previous results. Furthermore, we are able to better characterize the electrostatic contribution to the interaction, allowing quantitative estimates on the charge transfer between the sphere and substrate.

Typical experimental data taken on an as-prepared sphere are shown in Figure 5.5 (a) (force) and Figure 5.5(b) (force gradient). The long range variation of the interaction force exhibiting significant variations over distances of  $\sim 200$  nm, (see Figure 5.5(a)) supports the model of a localized charge located at the bottom of the sphere. The origin of the charge is a matter of considerable interest. It may arise from the mounting procedure during which the sphere is manipulated by the

tip of a sharp glass fiber. It is also possible that the charge is produced during the coarse approach stage of the experiment. This procedure inevitably produces a few contacts between the sphere and HOPG substrate until the coarse positioning is properly adjusted to allow data acquisition. As shown below, we present data which supports the latter of these two possibilities.

This data was fit using the theoretical model described above. The parameters  $Q$ ,  $R_{eff}$ , and  $H$  were adjusted until agreement with the data was obtained. The adjustment of the charge  $Q$  was somewhat constrained by the fact that charge densities significantly greater than  $\sim 3 \times 10^{-8}$  C/cm<sup>2</sup> will produce electric fields which initiate breakdown due to field emission. The parameters determined in this way are summarized in Table 5.3. Because the localized charge is dominant, we were unable to assess at this time the contribution from any uniform charge distributed throughout the sphere.

It is worthwhile to have an independent estimate for  $R_{eff}$ . To do this, we rely on an estimate of the contact radius  $a_o$  that an elastic sphere of radius  $R$  makes when in contact with a flat plane. Although such considerations neglect the surface roughness of the sphere, they provide an upper limit for  $R_{eff}$ . The surface charge density  $\sigma$  is then estimated from  $Q/(\pi R_{eff}^2)$ . As discussed in the previous section, the JKR model for adhesion can be used to determine this area of contact.

#### 5.4 Methanol Treatment-Charge Passivation

The objective of the experiment was to minimize the electrostatic interaction

<b>As-prepared Sphere</b>			
Parameters	Model	$F'_{interaction}$	$F_{interaction}$
H (eV)	1.1	$0.6 \pm 0.1$	$0.6 \pm 0.1$
R ( $\mu\text{m}$ )	3.0	3.0	3.0
$R_{eff}(nm)$	160 <sup>†</sup>	$58 \pm 4$	$52 \pm 7$
Q ( $e^-$ 's)		$500 \pm 40$	$535 \pm 10$
$\sigma$ ( $\frac{C}{cm^2}$ )	$\sim 10^{-9\ddagger}$	$(19 \pm 3) \times 10^{-8}$	$(25 \pm 4) \times 10^{-8}$

\* Interactions between polystyrene and graphite.[43]

<sup>†</sup> Contact radius based on JKR Model.[20]

<sup>‡</sup> Faraday cage measurement of charge on an ensemble of polystyrene spheres.[44]

Table 5.3

Parameters for fitting data for the As-prepared polystyrene sphere.

between the micrometer-sized polystyrene sphere and HOPG substrate. An illustration of the experimental procedure is found in Fig. 5.6.

We have found that a rapid change in charge can be produced by intentionally discharging the polystyrene sphere by soaking it in a stream of methanol. Typical data obtained after subjecting a sphere to this procedure is shown in Fig. 5.7 (a) (static) and Fig. 5.7 (b) (force gradient). A consequence of this treatment is the reduction in the charge acquired by the sphere. From Fig. 5.7 (b), it is clear that the van der Waals force becomes more important for small separations, a result expected as the amount of charge on the sphere is reduced. The parameters required to fit this data are given in Table 5.4.

At the present time it is not clear what effect the methanol rinse has on the polystyrene sphere. It could passivate the surface, producing a thicker barrier layer upon contact, thereby reducing the charge transfer. It is also possible that the rinse is effective in removing damaged polymer from the sphere's surface, thereby reducing the amount of charged polymer transferred from the sphere to the substrate. More work is required before this effect is better understood.

## 5.5 Summary

To better understand such phenomena as particle adhesion, it is useful to characterize the nature of the interaction forces acting on individual particles. We described the results of experiments that have been designed to quantitatively investigate the transition between a long-range electrostatic and van der Waals

<b>Methanol-treated Sphere</b>			
Parameters	Model	$F'_{interaction}$	$F_{interaction}$
H (eV)	1.1	$0.6 \pm 0.1$	$0.6 \pm 0.1$
R ( $\mu\text{m}$ )	3.0	3.0	3.0
$R_{eff}(nm)$	160 <sup>†</sup>	$58 \pm 4$	$52 \pm 7$
Q ( $e^-$ 's)		$260 \pm 20$	$260 \pm 10$
$\sigma$ ( $\frac{C}{cm^2}$ )	$\sim 10^{-9\ddagger}$	$(10 \pm 1.4) \times 10^{-8}$	$(12 \pm 2) \times 10^{-8}$

\* Interactions between polystyrene and graphite.[43]

<sup>†</sup> Contact radius based on JKR Model.[20]

<sup>‡</sup> Faraday cage measurement of charge on an ensemble of polystyrene spheres.[44]

Table 5.4

Parameters for the Methanol treated polystyrene sphere.

force. We show that by attaching a micrometer-size polystyrene sphere to an AFM cantilever, ambiguities in the geometry of the two objects under study can be eliminated, resulting in data that can be quantitatively interpreted using standard models for interaction forces. We show that the interaction force gradient measured under moderate vacuum conditions can be quantitatively understood in terms of two contributions: for large sphere-substrate separations, a simple electrostatic interaction suffices to adequately explain the data, while for smaller separations, the data is well described by the van der Waals force appropriate for a sphere above a flat plane.

Two independent techniques are used to measure the interaction between a micrometer-sized polystyrene sphere mounted on an atomic force microscope cantilever and an atomically flat highly-oriented pyrolytic graphite substrate. Measurements indicate that the spheres are charged by means of contact electrification. The measured interaction force is dominated by an electrostatic contribution due to localized charges triboelectrically produced on a sphere in the region making contact with the substrate. For small sphere-substrate separations, a van der Waals force becomes comparable to the electrostatic force. Results from both static and dynamic atomic force techniques show consistent results for both Hamaker coefficient and the triboelectrically produced charge which can be measured to an accuracy of  $\pm 10$  electrons.

Using the dynamic mode of operation to measure the force gradient, the net interaction between the sphere and plane was found to have two contributions.

For  $z_o \geq 30$  nm, an electrostatic force due to charges trapped on the polystyrene sphere dominates the force gradient. For  $z_o \leq 30$  nm, a van der Waals interaction, characteristic of a sphere near a flat plane, is observed. This technique was also used to verify that the data scaled correctly with the sphere radius according to the proposed model. Additionally, the static mode of operation provide a means to measure the interaction force directly. This technique provided an independent check to the force gradient measurements. The parameters used to fit the data for each method were consistent with one another. Fits to the data were in good agreement with theoretical expectations, and allow estimates of the surface charge density triboelectrically produced on the sphere's surface.

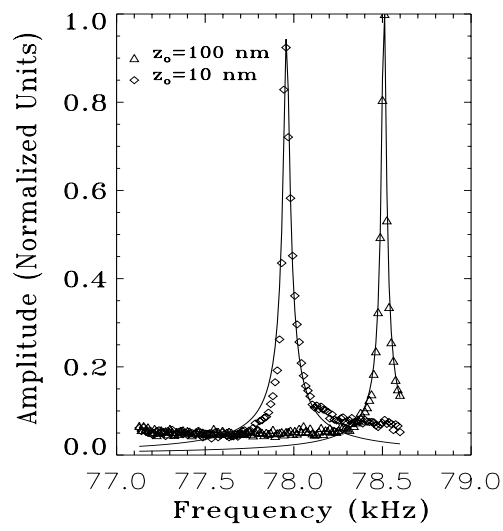


Figure 5.3

The amplitude of the cantilever oscillation is given for two different values of  $z_0$ . The solid lines are a best fit to the data using Eqn. 3.26.

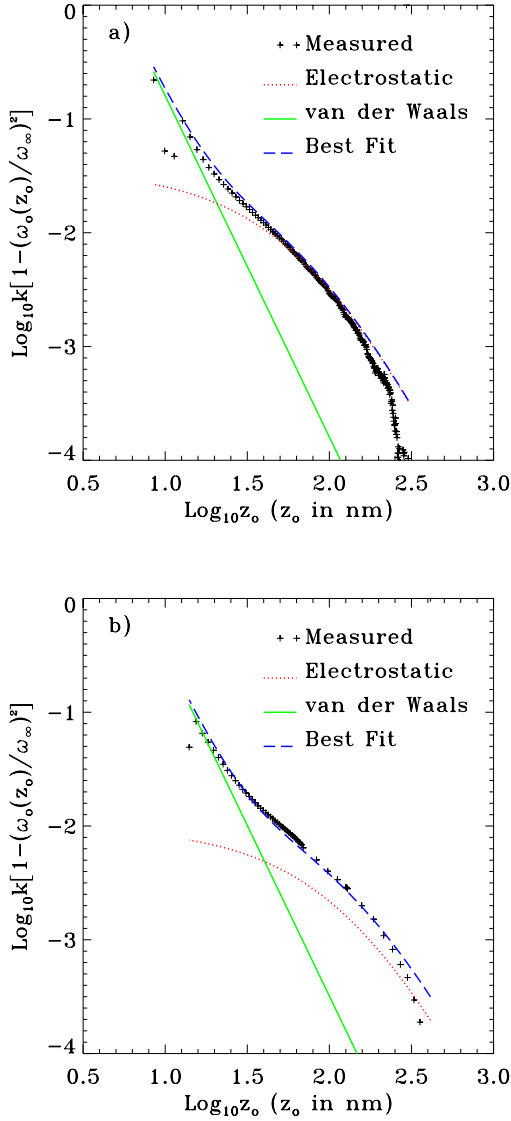


Figure 5.4

Data measuring the force gradient of the interaction force between a polystyrene sphere and an atomically flat HOPG substrate. In (a), a plot of  $\log_{10} \left[ k \left( 1 - \left( \frac{\omega_o(z_o)}{\omega_\infty} \right)^2 \right) \right]$  vs  $\log_{10} z_o$  for a 3  $\mu\text{m}$  radius sphere. The dashed line (see Table 1) is a fit to the experimental data. In (b), a plot of  $\log_{10} \left[ k \left( 1 - \left( \frac{\omega_o(z_o)}{\omega_\infty} \right)^2 \right) \right]$  vs  $\log_{10} z_o$  for a 6  $\mu\text{m}$  radius sphere. The dashed line (see Table 2) is a fit to the experimental data.

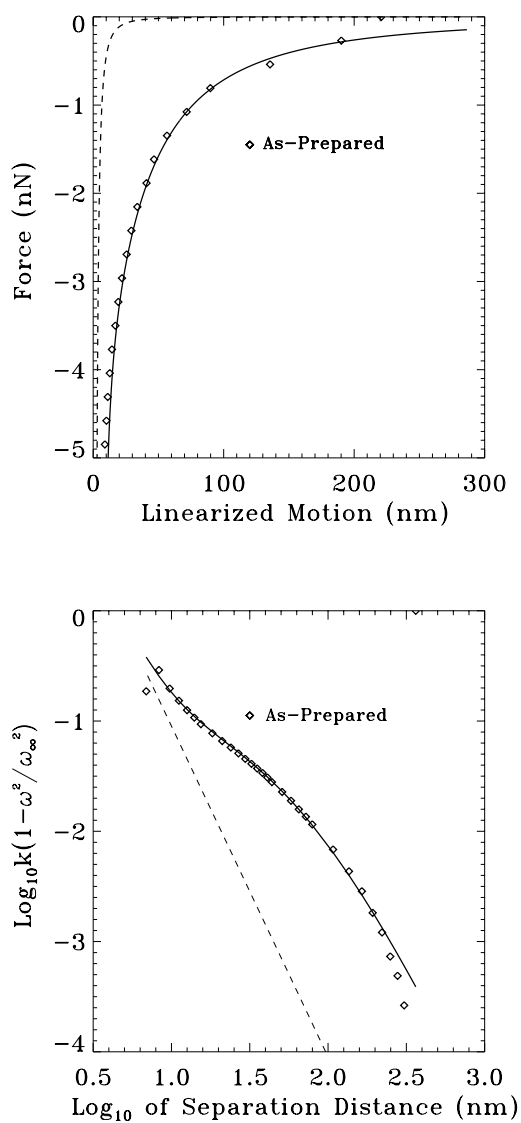


Figure 5.5

Data from a static force measurement (a) and a dynamic force gradient measurement (b) of a  $3 \mu\text{m}$  radius polystyrene sphere as a function of surface-to-surface separation from a flat HOPG substrate. The data is typical for an as-prepared sphere. The fits to the data are shown by the solid lines. The dashed line shows the contribution for a pure van der Waals interaction. The fitting parameters are summarized in Table 5.3.

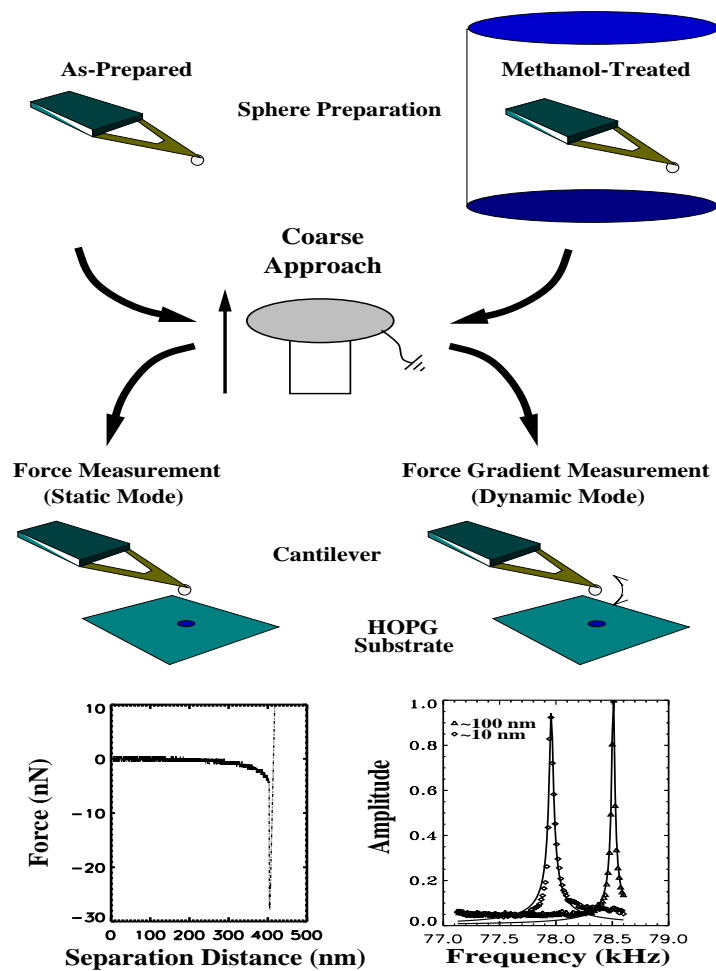


Figure 5.6

Experimental procedure for measuring the interactions between the polystyrene sphere and HOPG substrate.

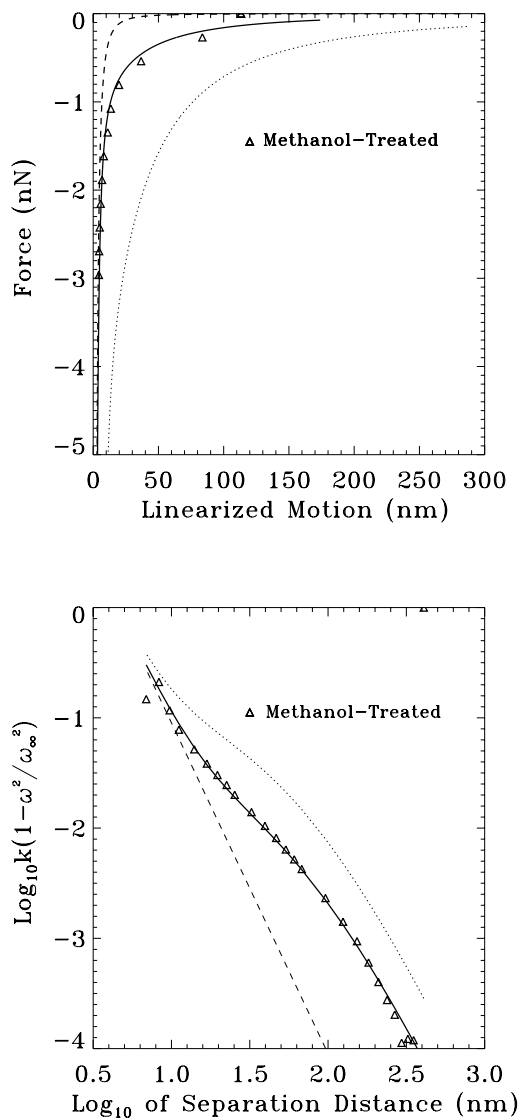


Figure 5.7

Typical data for the force (a) and force gradient (b) acting on a  $3 \mu\text{m}$  radius methanol-treated polystyrene sphere as a function of surface-to-surface separation from a flat HOPG substrate. The fits to the data for the methanol-treated sphere are shown by the solid lines. The dashed line indicates the contribution due to a pure van der Waals interaction. The dotted line represents the fit to the as-prepared polystyrene sphere. The fitting parameters are summarized in Table 5.4.

## 6. Contact Electrification

### 6.1 Contact Electrification

The nature in which materials charge is an important problem in a variety of fields. Understanding how materials obtain charge is a difficult task, and it requires more than a basic knowledge of electrostatics. To date, there is no unified model which can explain how and why some materials charge while others do not. Some of the difficulty lies in the fact that experimental evidence indicates that you can charge materials in a variety of ways such as: point contact, rubbing, rolling, and heating.

The phenomena of charging two objects dates back at least 2500 years. Rubbing a piece of amber created an invisible force which would attract pieces of matter. While the observance of the phenomena of charging is not new, new techniques of measurement are the focus in this study. In particular, there is a great difficulty in quantifying the charge on microscopic objects. This is of tremendous importance in fields ranging from electrophotography to medicine. It is important to understand why materials charge, as well as how to measure the charge. The atomic force microscope can be used to perform such measurements. Not only can the AFM provide information about long-range attractive forces, it can also

provide information about how these interactions effect the adhesive properties between materials. Measurement of charge transfer should also include the region over which the charge is spread. Charge density information is useful in determining whether or not back-tunneling of charge occurs when the two materials are separated. It is, however, difficult to know exactly the contact area between two bodies. There are models such as the JKR model for adhesion from which contact areas can be determined, but this assumes ideally smooth surfaces. This study focuses primarily on the charging phenomena resulting from contact electrification. In particular, the interaction between a spherical particle and atomically smooth surface will be considered. As will be shown later, contact electrification not only depends on the type of materials making contact, but also the geometry of the interacting materials.

There are several preliminary issues to outline in order to better understand the process of contact electrification. One of the main perspectives is to understand what is physically possible in a measurement. There are experimental limits to the nature and amount of charge which one will expect in charging micrometer-sized objects. Before discussing the details of the actual measurements, the experimental limitations will be considered.

The hypothesis being made is that a micrometer-sized dielectric sphere may become charged when making contact with a conductive surface. The charge on this particle may be determined by measuring the long-range interaction force between the grounded conductive surface and itself. Based on the dimensions of

the particle, and the experimental conditions of the measurement, it is possible to determine the maximum charge densities sustainable on the particle before electrostatic breakdown occurs. This breakdown, known as the Paschen limit, will set a restriction on the charging which can occur on the particle. This limit is of fundamental importance when considering the charging of microscopic particles.

Discharging will depend on several conditions such as: the atmospheric conditions; the geometry; the electric field between particle and surface; mean free path between collisions of gas molecules; and the separation distance between the materials. All of these conditions can have a dramatic influence on the amount of charge which can be sustained. For these experiments, we consider the limitations for a spherical geometry. For an isolated sphere of radius  $R$ , the breakdown field producing corona discharge can be determined from the derived relation,

$$E_{breakdown} = 37R^{-0.3} \times 10^6 \frac{V}{m} \quad (6.1)$$

with the radius given in centimeters.[45] The relation given by Eqn.6.1 is for standard atmospheric conditions. Figure 6.1 indicates the maximum field which can be permanently maintained as a function of the radius of micrometer-sized spheres. This can also be interpreted as a maximum sustainable charge density of

$$\sigma_{breakdown} = 10R^{-0.3} \times 10^{-9} \frac{C}{cm^2} \quad (6.2)$$

as shown in Figure 6.2. Since the normal operating conditions of our measure-

ments are at moderate vacuum levels of  $10^{-3}$  Torr, these breakdown limits will be substantially higher.

It is important to note that discharge is initiated by stray ions which might exist in the atmosphere, or from cosmic rays. It follows that by reducing the pressure and the volume in which the field exists, higher fields can be sustained. Because these measurements are performed for small separation distances between the sphere and conductive surface, there is a small likelihood for discharge to occur due to ionization. This is easy to show. For instance, if we consider that a typical sphere has a radius of  $\sim 5 \mu\text{m}$ , and a separation distance of 10 nm from the surface, an estimate of the number of ions which pass through the space of separation can be determined. There are approximately 15 ion pairs per  $\text{cm}^3$  under normal atmospheric conditions. Only 2 ion pairs per  $\text{cm}^3$  are due to cosmic rays. The region of interest is that where the field due to contact electrification would arise. Based on the JKR model for adhesion, a typical contact radius is approximately  $\sim 100$  nm in diameter. Using a cylindrical approximation, the effective volume is then  $10000\pi \text{ nm}^3$  for separation distance mentioned previously. We conclude that for such a small volume, there is only a minute likelihood of ionization because of the mean free path between collisions. A typical mean free path between collisions in normal atmosphere is of the order of a few centimeters. At moderate vacuum levels ( $10^{-3}$  Torr), the mean free path between gas molecule collisions is on the order of meters. Thus, the mean free path for collision is much larger than the separation between the particle and surface where ionization can occur.

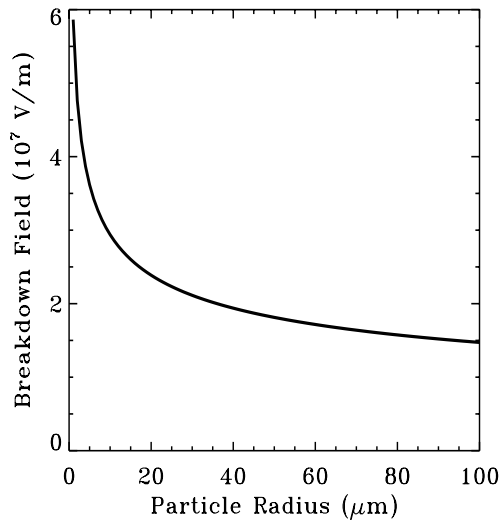


Figure 6.1

Maximum electric field under atmospheric conditions before Paschen breakdown occurs.

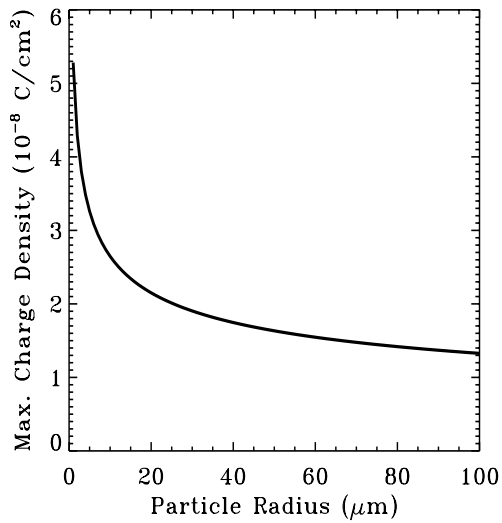


Figure 6.2

Maximum surface charge density under atmospheric conditions before Paschen breakdown occurs.

There are three main classifications to contact electrification: metal-metal contact, metal-insulator contact, and insulator-insulator contact. While metal-insulator contacts are the primary interest of this study, it is important to look at the other classifications as well. More detailed descriptions of these interactions may be found elsewhere.[32, 45, 46] The basic principal behind all these processes, however, is that the two interacting systems reach a thermodynamic equilibrium through charge transfer between allowable energy levels of the materials.

### 6.1.1 Metal-Metal Interactions

It is important to begin our review of contact electrification between metals for two reasons. The first is that there is a general agreement about the mechanisms for charge transfer between metals. The second reason is that the concept of thermodynamic equilibrium is the basis for which contact charging is described between insulators.

Charge transfer occurs between metals, but the amount of charge transferred may not be very noticeable. An obvious reason is that metals are very good conductors of charge. Unlike insulators, the method of charging does not seem to influence the total charge which can be acquired between metals. In spite of the difficulty in charging metals, the mechanisms for charging them are well-understood.

The theory of contact electrification between metals is based on achieving thermodynamic equilibrium between the two contacting materials. The equilibrium

condition is that the Fermi level becomes constant across the two metals. To achieve this, it is necessary for electrons from one material to be transferred by tunneling to the other material. This tunneling will occur when the separation between the two metals is sufficiently small for the electrons to tunnel through the barrier. If the metals are dissimilar, the charge transfer is governed by the differences in their Fermi energies, or equivalently, their work functions. Typical values for work functions of metals lie in the range of 3 to 5 eV.

The behavior of dissimilar metals coming into contact is shown in Figure 6.3. In order to achieve the equilibrium condition for dissimilar metals, a contact potential is created. The contact potential is given by,

$$V_c = \frac{(\phi_2 - \phi_1)}{e} \quad (6.3)$$

where  $e$  is the charge on an electron and  $\phi_{1,2}$  are work functions of the two materials. An electric field is produced at the interface due to this contact potential.

When a contact potential arises from the two metals in contact, an effective capacitance is formed. As the metals are separated, the contact potential and effective capacitance will change so as to maintain a thermodynamic equilibrium. The principle condition of interest is when the materials have been separated. As the materials are separated, electrons will tunnel across the gap to maintain  $V_c$ . Charge flows back readily between metals, so the overall charge will be small. Harper has calculated the charge on two metal spheres after separation to be

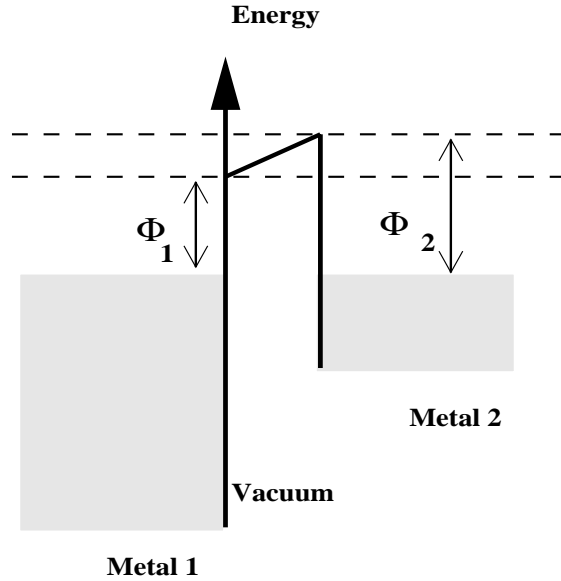


Figure 6.3

Energy level diagram for a metal-metal contact.

$$Q_o = C_o V_c . \quad (6.4)$$

In general, for metal-metal interactions contact electrification is defined by the contact potential  $V_c$  and capacitance  $C_o$  which depends on the geometry and surface roughness of the contacting bodies.

This field will cause an attractive force to result between the materials as they are separated. With metals, back tunneling can occur leading to a reduction in any charge at the interface due to the contact. Metal conductivity will act to minimize the effect contact electrification will have on the long-range attractive interactions, as well as adhesion.

Surface roughness has also been shown to influence contact electrification be-

tween metals. Since the capacitance between the materials is dependent on their geometry, any asperities will affect the charge on the materials.

### 6.1.2 Metal-Insulator Interactions

The interaction between metals and insulators is of particular interest in this study. The type of insulators relevant to this study are polystyrene and glass. Unlike metal-metal interactions, the mechanisms behind contact charging of insulators are not as thoroughly understood. Several researchers have performed experiments using bulk materials to measure charge transfer.[47, 32, 48, 49, 50, 31] Unfortunately, there has been little work done to understand the effects of contact electrification to small particles. There is evidence that the charging of an insulator is strongly correlated to the work function of the metal it is contacting.[32] In this case, the charging agent would be the result of electron transfer rather than ion transfer. Typical charge densities measured for metal-insulator charging range from  $10^{-6} \frac{C}{m^2}$  to  $10^{-3} \frac{C}{m^2}$  for various materials and measurement conditions.

The focus of this study is with metal-insulator interactions. There are two ways in which charge may be transferred. One method is that electrons may pass from the metal to empty states in the insulator. The second method is that electrons may pass from occupied insulator states into the metal. Insulators may have several types of electron states: Bloch states of the conduction and valence bands; intrinsic localized surface states; localized states due to impurities.

It is best to consider the charge transfer by looking at the energy levels for a

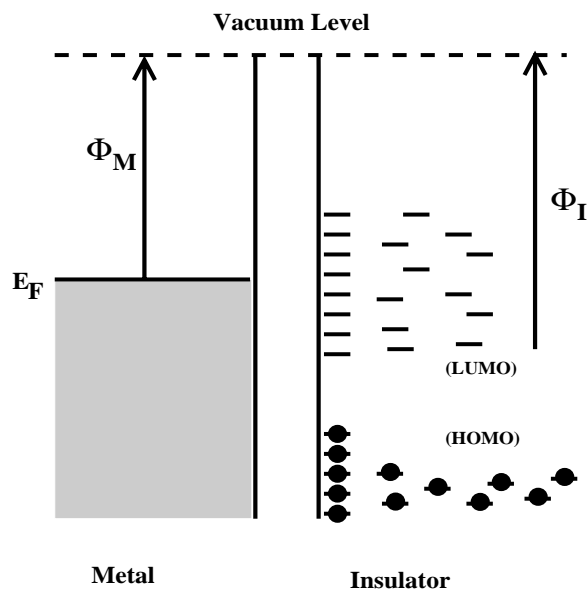


Figure 6.4

Energy level diagram for a metal-insulator contact.

metal-insulator contact as shown in Figure 6.4. Polymers have states in which they can either accept or donate charge. These states are referred to as highest occupied molecular orbitals (HOMO) and lowest unoccupied molecular orbitals (LUMO). These levels will vary depending on the polymer, as do work functions for metals. The electron states may also be localized, as is the case with polystyrene. The sign of the charge acquired by the material will depend on where the donor/acceptor states lie relative to the Fermi surface of the metal it makes contact with.

As discussed in the previous section, metals have work functions ranging from approximately 3 to 5 eV. Polymers have HOMO levels approximately 9 eV below vacuum level, and have LUMO levels a few electron volts below vacuum. Charging is still observed for metal-polymer contact, although it appears there are no energy

states which charge can be transferred between the materials. This has led several researchers to conclude that contact electrification may be controlled through the existence of surface states in the polymer.[51, 47]

An important point to remember is that most theories explain any transferred charge in terms of thermodynamic equilibrium being achieved. For metal-insulator contacts, this is not likely, especially if charging continues after several contacts. As we have discussed, insulators are not amenable to discussion in terms of a Fermi energy. Instead, they have a series of donor/acceptor states which will be filled or emptied.

### 6.1.3 Insulator-Insulator Interactions

Due to the complexities involving the study the electronic properties of polymers, contact charging will be only be mentioned in passing. As discussed in the previous section, charge transfer will occur as long as there are allowable states for electrons to tunnel into. In the case of insulators, the donor/acceptor states should be within less than 1 eV at separations of under a nanometer. Conceptually, contact electrification between two insulators will be dependent on their density of states. Figure 6.5 indicates qualitatively how charging may occur between polymers. A more detailed discussion can be found elsewhere.[52]

## 6.2 Charge Transfer Models

The mechanisms of charge transfer between materials has remained a subject of great debate. There exists three main models for describing the charge trans-

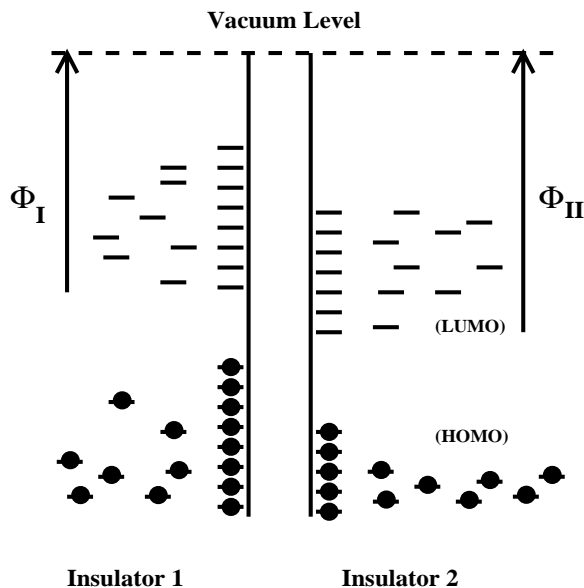


Figure 6.5

Energy level diagram for an insulator-insulator contact.

fer mechanism: electron transfer, ion transfer, and material transfer.[45, 32]. The phenomena of charging is dependent on the materials, their preparation, and the process by which they are charged. It is apparent that charging of objects can be produced by many methods. The process considered in this study is that of contact electrification. In many cases, there are several processes which act together in generating charge. By constraining the process from charging by friction or heating, it is hoped that more can be understood about contact charging.

The most commonly observed process of charging is by rubbing two insulating materials together. A familiar example is that of rubbing glass with silk. In this situation, the glass rod will become charged positively while the silk becomes negatively charged. This triboelectrification process can become extremely complex

depending on how the rubbing is carried out. In this simple example, it has been reported by Shaw that applying varying pressures to the rubbing will result in changes in the sign of charging on both the glass and silk.[53] Those who have performed triboelectrification measurements are familiar with the capricious nature of charging. It can be concluded that the way in which materials are brought into contact is just as important as the properties of the materials when measuring charge.

### 6.2.1 Electronic Charge Transfer

The premise for the electron charge transfer model is when two surfaces come into contact, electrons from one material may tunnel into the other material. The issue of whether or not one of the materials will become charged depends on whether or not allowable electron states exist in a material. The main interest of this study is contact electrification between metals and polymers.

As stated in the previous section, most charging models are based on the principle that thermodynamic equilibrium is achieved between the contacting materials. In other words, the Fermi level in both bodies must be the same throughout. For insulators such as polymers, a Fermi level cannot be defined. This is because polymers will persist in a non-equilibrium condition indefinitely. When contact is made, electrons can be transferred. Assuming that equilibrium could occur, a dipole arises from this charge transfer which results in a contact potential. The potential formed from the field will raise the Fermi level of the insulator to that

in the metal. Calculating the amount of charge transferred is complex, and a more thorough treatment can be found elsewhere.[45]. Instead, a more qualitative discussion of the process is outlined here. The objective is to determine the mechanisms which best explain how the charging occurs for contact electrification.

Let us first consider the transfer of charge between metal and insulator planes. We assume that the Fermi level of the metal is above that in the insulator initially (see Fig.6.6). In this case, electrons will move from the metal to insulator.

Our condition of thermodynamic equilibrium is met when the Fermi level is constant throughout both materials. Poisson's equation must also be satisfied for the charge density in the insulator,

$$\frac{\partial^2 V}{\partial x^2} = -\frac{\rho}{\kappa \epsilon_o} . \quad (6.5)$$

Using Fermi-Dirac statistics, the charge density of the insulator may be determined based on the density of states. Suppose that the polymer has empty trap states (acceptor-like in this discussion)  $N_A$  per unit volume above the Fermi level. In addition, assume that these states all lie at the same energy level  $E_A$  (see Fig.6.6).

Then the charge density for the insulator in contact with the metal will be

$$\rho = -N_A e e^{-\frac{E_A - eV(z)}{kT}} . \quad (6.6)$$

The expression  $eV(z)$  refers to the energy of a trap a distance  $z$  from the surface.

The surface charge density,  $\sigma$ , is determined by solving for the boundary condition given by Eqn. 6.5,

$$\sigma = -\kappa\epsilon_o \left( \frac{\partial V}{\partial x} \right)_{x=0} . \quad (6.7)$$

Knowing the potential difference at contact with the surface ( $z = 0$ ) is  $V = V_c$ ,

$$\sigma \approx - \left( 2\kappa\epsilon_o N_A kT e^{-\frac{E_A}{kT}} \right)^{\frac{1}{2}} e^{\frac{eV_c}{2kT}} . \quad (6.8)$$

This charge density is typically very small due to the low population of states that exist above the Fermi level. The density of charge will be far greater if the insulator has empty states below the Fermi level of the metal prior to contact. After contact, most states near the surface of the insulator in the region of contact would become filled. Unfortunately this model is oversimplified based on experimental findings of Davies which indicate that nylon can charge either positively or negatively.[54] The only way this can be explained is if there were levels which were partially full and partially empty.

If we consider the condition of states below the Fermi level in the metal prior to contact being empty, the charge density will be different. Upon contact with the metal, the Fermi level of the insulator will have to increase by an amount  $eV_c$  in order for the equilibrium condition to be satisfied. The states near the surface of the insulator will become full, and  $\rho = -N_A e$  in the charged layer of thickness  $z_o$ . The boundary conditions for Eqn.6.5 are that  $V = 0$ , and  $\frac{\partial V}{\partial z} = 0$  at  $z = z_o$ .

The solution is then,

$$V = \frac{N_A e}{\kappa \epsilon_o} (z - z_o)^2 . \quad (6.9)$$

From Figure 6.7, the potential difference across the layer of charge is then defined as  $V_c - \frac{E_A}{e}$ . The second term is much smaller than the contact potential at the interface ( $z = 0$ ). Thus, the charge density given by  $\sigma = N_A e z_o$  where

$$z_o = \left( \frac{2\kappa\epsilon_o V_c}{N_A e} \right)^{\frac{1}{2}} \quad (6.10)$$

is then

$$\sigma = - (2\kappa\epsilon_o N_A e V_c)^{\frac{1}{2}} . \quad (6.11)$$

An analogous argument may be made for donor states that would empty electrons into the metal. The important point to keep in mind is that it is necessary to have both donor and acceptor levels to fully explain the charging behavior in polymers. If the Fermi level of the metal lies below that of the insulator, it will take up electrons when it makes contact. Likewise, if the Fermi level of the metal lies above that of the insulator, electrons will be given up to the states in the insulator. Which states are filled will depend on the relative location of the donor/acceptor levels.

While these models yield results which can determine the sign of the charge which arises from contact electrification, they do not explain the behavior which

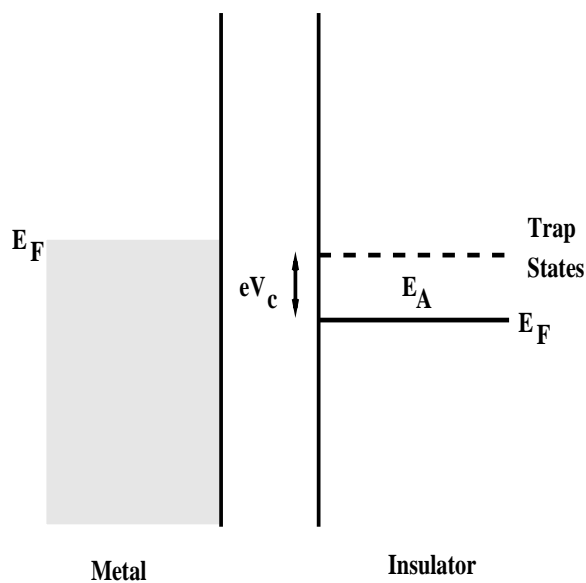


Figure 6.6

Electron transfer model for metal-insulator interaction assuming there is only one energy level for the acceptor states.

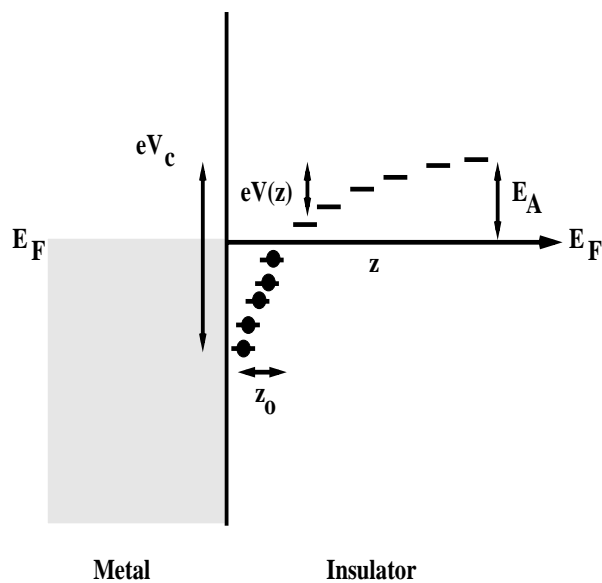


Figure 6.7

Localized states within the insulator which are initially below the Fermi level. The equilibrium condition causes band bending to occur resulting in excess charge in acceptor states.

is experimentally observed. Measured contact charging indicates a linear relationship between the work function of the metal and the charge density. A possible explanation is that the model assumes that the insulator state is at a discrete level. It is more likely that the states are spread over a range in energy. If we assume that the distribution is uniform and the total number of states is  $N_o$ ,

$$\rho = N_o e^2 V . \quad (6.12)$$

Then the condition given by Eqn.6.5 yields a solution for the potential after contact of

$$V = V_c e^{-\frac{\phi}{\alpha}} \quad (6.13)$$

$$\alpha = \left( \frac{\kappa \epsilon_o}{N_o e^2} \right)^{\frac{1}{2}} \quad (6.14)$$

The charge density is then given by

$$\sigma = \left( N_o e^2 \kappa \epsilon_o \right)^{\frac{1}{2}} V_c . \quad (6.15)$$

A charge density may be estimated from Eqn.6.15 and assuming  $\kappa \approx 3$ ,  $N_o \approx 10^{22} m^{-3}$ , and  $V_c \sim 1V$ . These values give a  $\sigma \sim 10^{-4} \frac{C}{m^2}$  which is the same magnitude observed in our measurements. While we do not measure a contact potential, according to this model, we would expect the charging to scale with work functions. As indicated by Eqn. 6.3 for metal interactions, the contact po-

tential is proportional to the work functions of the metals. Although this may not be exactly the case for insulators, it does provide a qualitative understanding of contact electrification. In the case of insulators, charge transfer will depend on the location of donor/acceptor levels in each material.

### 6.2.2 Ionic Charge Transfer

Another method in which charging might occur is through ion transfer. In the case of polymers, it is quite possible that ionic material is present due to the process in which the material is prepared. This model assumes that a known concentration of ions are contained in at least one of the materials. The type of charge will depend on the molecular salt or ionomer present within the organic material. The ion model is similar to the electron transfer model in that it does not account for the path or the kinetics of the exchange. The main points of this model are: the charge results from the transfer of ions across the contact interface; only ions in the surface region of the particle and surface it contacts are available for transfer; the ions will reach an equilibrium condition between the two surfaces which is governed by the polymer-ion interactions; and the initial conditions are that the surface compositions are known.

The formalism of the model is outlined by Diaz, but it parallels the electron transfer model except for the charging agent.[49] Where it differs is that it accounts for the chemical nature of the interacting materials. The model is very dependent on the ion mobility between materials, as well as the environment.

A key point which must be considered is that ion transfer should be independent of the actual interacting materials. If ions exist on the polystyrene beads due to their preparation, they should transfer to the substrates used in the interaction measurements. As will be shown in the following section, this was not observed to occur.

### 6.2.3 Material Charge Transfer

When two surfaces come into contact, it is possible that material can be transferred. The transferred material may be either fugitive particulates contaminating the surfaces, or part of the surface material itself. Contamination on surfaces is always prevalent. Most common contributors are water if surfaces are exposed under ambient conditions, or residual material from a fabrication process. If the contacting materials are compliant, it is possible that the pressure at contact is enough to cause the transfer due to adhesion. Figure 6.8 shows a dramatic illustration of material transfer between a compliant substrate and a polystyrene sphere. Various methods can be used to treat surfaces in order to remove or prevent contamination.

One of the unique features of the AFM is that it has a tremendous amount of sensitivity to variations in sphere-sample interactions. By looking at loading/unloading curves taken using the AFM, one can determine physical properties of the interacting surfaces. Material transferred from the surface being studied to the sphere mounted on the cantilever may influence the jump-to-contact phenomena. The double jump to contact indicated in Fig. 6.9 illustrates how the

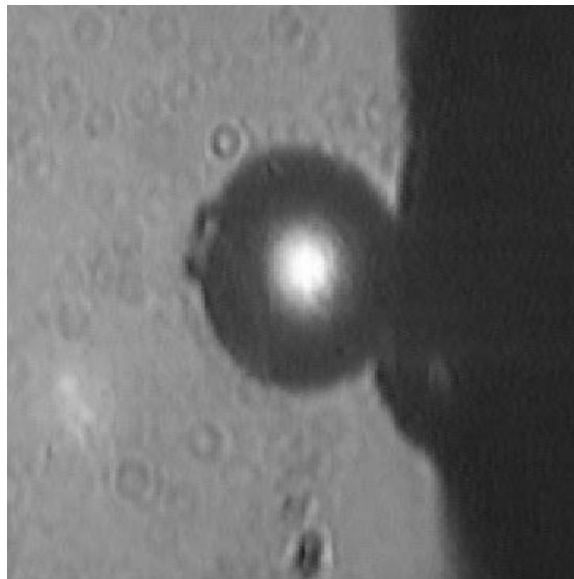


Figure 6.8

Material transfer after sphere contacted a compliant substrate.

interaction may be sensitive to minute traces of intermediate material. While it may be difficult to quantify the mass associated with the contaminant, information about cross contamination can be recorded in this way. Also, by studying the actual shape of the loading/unloading curve will also provide information such as the elastic properties of material transferred.

### 6.3 Charge Transfer Experiments

Contact electrification measurements were performed between micrometer-sized spheres made of polystyrene and flat substrates of freshly cleaved highly oriented pyrolytic graphite and a  $0.2 \mu\text{m}$  thick Au[111] film grown on mica using AFM techniques. It was discovered that polystyrene/HOPG interactions exhibited the largest electrostatic charging effects. We conclude that the observed contact

electrification is due to electronic charge transfer between the materials rather than from ionic or material transfer. It was also determined from force measurements that the amount of charge increased linearly with the number of contacts made with the substrate.

The attachment of micrometer-size spheres to atomic force microscope (AFM) cantilevers to study the force of interaction between the sphere and a nearby substrate has received widespread interest since 1991.[55] One distinct advantage of this approach is that by using a probe of known geometry, comparison between experimental force curves and theoretical expectations become possible. The published work in this area has focussed on two issues. One is the measurement of the surface force between a sphere and a substrate immersed in a liquid. To address this issue, measurement of forces between a variety of spheres and substrates immersed in a liquid medium have been reported.[56, 57, 58, 59, 60, 61, 62, 63] Another broad issue centers around a quantitative measurement of the adhesion between small micrometer-size particles and substrates. In this arena, the ability of an AFM-related technique to quantitatively measure lift-off forces in an ambient or controlled atmosphere is particularly appealing, since concerns about surface energies, surface asperities, and the influence of applied electric fields can be addressed.[64, 65, 66, 21, 67]

Recently, in an attempt to better understand the origin of adhesion forces, quantitative studies of the surface force interaction as a function of particle-substrate separation have been reported.[68, 69] Two AFM techniques are used

to measure the interaction force and force gradient between a spherical particle and flat surface. These measurements have shown that two contributions to the interaction force are dominant: (i) a contribution due to a surface triboelectrically charged in patches[70] and (ii) a contribution due to the van der Waals force.[1] The sensitivity of the technique to *both* van der Waals and electrostatic forces allows for the study of contact electrification between materials. This approach provides sensitivity to charge variations of  $\sim 10$  electrons and relies on fitting data with three parameters:  $H$ , the Hamaker constant;  $R_{eff}$ , the contact radius formed between the particle and substrate; and  $Q$ , the charge transferred between the particle and substrate.

These prior measurements, made using an atomically flat substrate, highly-oriented pyrolytic graphite (HOPG) and polystyrene spheres, indicated that for small surface-to-surface separations, the van der Waals contribution dominates over that due to the localized charge. The origin of the surface charge distribution was not explicitly addressed. The purpose of this study was to investigate further the charging of the polystyrene sphere.

The AFM used is a home-built system based on an optical beam detection technique.[37] The analysis of the interaction force or force gradient data can be found elsewhere.[68] Using these techniques, it is possible to detect charging of micrometer-size polystyrene spheres when they come into contact with substrates. If charging occurs from contact with the substrate, these techniques may be used to determine the amount and distribution of charge using simple models.

In this study, measurements of the interaction force and force gradient were performed in a moderate vacuum ( $\sim 10$  mTorr) after purging the stainless steel vacuum chamber housing our AFM system with dry nitrogen. Contact electrification studies were made by attaching  $\sim 5 \mu\text{m}$  radius polystyrene spheres to AFM cantilevers and touching them to different atomically flat substrates. The two substrates were highly-oriented pyrolytic graphite (HOPG) and a  $0.2 \mu\text{m}$  thick Au[111] film evaporated on a mica substrate. During the course of data acquisition, several contacts were made with the substrate using an applied load of approximately 10 nN and fixed contact time of approximately 1 second.

Since the spherical particles are small, and loads of less than 100nN are applied, only a small region of contact is made. According to the Johnson, Kendall, Roberts (JKR) model for adhesion,[20] micrometer-size spheres form contact areas typically on the order of  $\pi R_{eff}^2 \simeq 10^4 \text{ nm}^2$ . [68] For the studies reported below, the pressure applied to the contact region is smaller than the elastic limit of the materials, so significant distortion is not likely to occur. For the materials used, the pressure applied during contact is approximately 10 MPa. The elastic modulus of polystyrene, Au, and HOPG are 3000 MPa, 80 GPa, and 17 GPa, respectively.

In order to further investigate charging effects, two different substrates were carefully chosen for study. Both substrates must be conducting in order to use an image force to describe the electrostatic interaction. From a standard triboelectric series, it is known that polystyrene touched to graphite should produce a large charge separation, while for polystyrene on Au, the charge transfer should be

minimal. The physical basis for this observation is based on the location in energy of charge traps located in polystyrene. Polystyrene has a band of acceptor states located between 3.5 and 5.0 eV below the vacuum level. For Au, ( $\phi \simeq 5.3$  eV), the Fermi energy is below the acceptor states in the polystyrene and one would not expect charge transfer to occur at room temperature. On the other hand, for HOPG, with a work function of  $4.7 \pm 0.2$  eV,[34, 33, 71] charge transfer to the acceptor states can occur. A schematic energy diagram for the two substrates studied here is given in Fig. 6.10.

The experiment was performed by first touching the sphere to the substrate. This served two purposes. First, it allowed for any charge transfer between the substrate and sphere. Second, it provided a z-calibration when the surface-to-surface separation was equal to zero. The experimental force curves obtained upon approaching the substrate *after* touching a polystyrene sphere (nominal radius of 5  $\mu\text{m}$ ) to either the HOPG and Au substrate show a distinct difference. For the case of polystyrene on HOPG, a long range force consistent with charge localized at the point of touching is observed. For polystyrene on Au[111], no long-range electrostatic force is detected and force gradient measurements show a predominately van der Waals interaction. Representative force curves are shown in Fig.6.11.

The data were further analyzed and the amount of charge transferred on contact was determined by fitting the measured force gradient data using an interaction force model discussed previously.[68, 69] The amount of charge required to fit the data for the two cases studied was considerably different. The results are

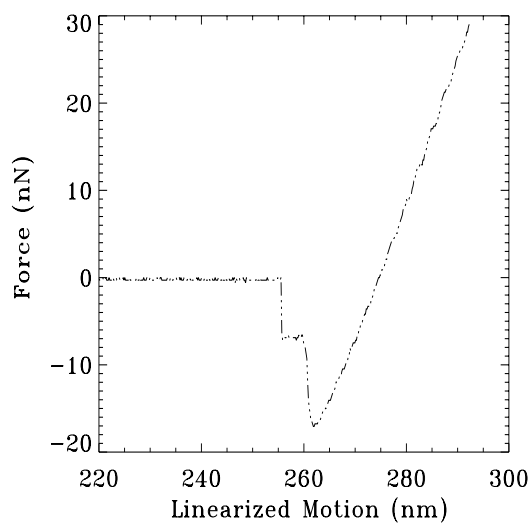


Figure 6.9

The transfer of material may be detected from variations observed in the loading force curve

### Electron Transfer Model

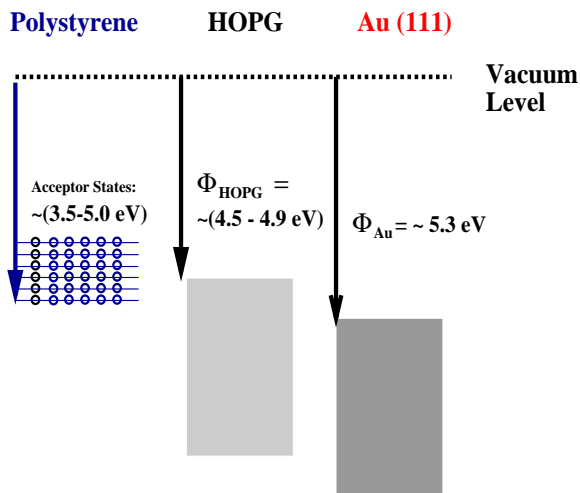


Figure 6.10

Schematic illustration of the electron transfer model. Polystyrene has acceptor states which are accessible to electrons from HOPG near the Fermi level. The Fermi level for Au[111] is below the states in polystyrene and electrons cannot be transferred.

<b>Fitting Parameters: Force-Gradient Data</b>		
Parameters	PS/HOPG	PS/Au
H (eV)	0.6	0.04
R ( $\mu\text{m}$ )	4.5	5.0
$R_{eff}(nm)$	$70 \pm 4$	$50 \pm 7$
Q ( $e^-$ 's)	$300 \pm 40$	$55 \pm 10$

Table 6.1

Summary of the parameters used in fitting contact electrification data to model.

summarized in Table 6.1.

One conclusion reached from this experiment is that a minimal contact electrification results for the polystyrene/Au system. It was determined that multiple contacts between the polystyrene and Au substrate showed no significant change in the interaction force. From the force measurements, there is no significant charging even after 70 contacts with the Au substrate. While force gradient data requires a small amount of charge to fit the data (see Table 6.1), the value does not change with multiple contacts. The predominant interaction force is a van der Waals interaction.

This behavior can be contrasted to the polystyrene/HOPG system which exhibited continued charging after every contact. By fitting data from force measurements after consecutive contacts with the substrate, an estimate of the amount

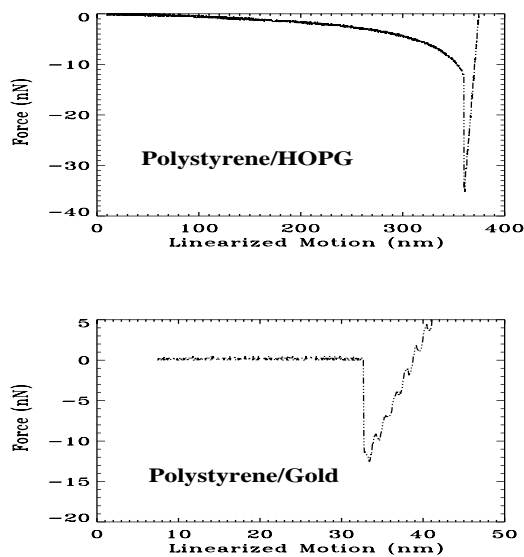


Figure 6.11

Representative plots of the measured force acting between a  $5 \mu\text{m}$  radius polystyrene sphere mounted on a cantilever and (a) a HOPG substrate and (b) a Au[111] substrate. The data were taken upon approach after the sphere was touched to a particular substrate and withdrawn. The long-range interaction observed after touching the HOPG substrate is consistent with the an electrostatic force produced by charges localized at the bottom of the polystyrene sphere. For the Au[111] substrate, a careful analysis of the force gradient data just before jump to contact indicates a van der Waals interaction is the dominant contribution to the net interaction force. Note the change in scale of the abscissa between the two sets of data.

of charge per contact can be determined. While tribo-charging can be observed for any polystyrene sphere/HOPG interaction, the rate of charging seems to vary. In general, the charging observed is linear, with a rate varying from  $\sim 2$  to  $\sim 20$  electrons per contact. Figure 6.12 illustrates this effect for a  $3 \mu\text{m}$  and  $5 \mu\text{m}$  radius polystyrene sphere.

One further check was made to test whether these results might be anomalous. After touching a polystyrene sphere to Au, the Au substrate was replaced by a freshly cleaved substrate of HOPG. Subsequent measurements indicated that contact electrification did occur after the first contact of the polystyrene sphere with the HOPG substrate.

The precise mechanism of charge transfer between two different materials has remained a subject of debate. There are three models for describing the charge transfer mechanism: electron transfer, ion transfer, and material transfer.[45, 47, 49, 48]. For the well characterized experiment performed here, it is possible to discuss which mechanism is most likely responsible for the charge transfer observed.

It is unlikely that the transfer of fugitive material is responsible since the particles were cleaned with high purity methanol and the substrates were freshly prepared prior to measurements. In addition, the effect of a material transfer would be apparent from distortions to the loading and unloading curves taken during force measurements. None were observed.

It is possible that charge transfer results from existing ions in the polystyrene material. However, the data obtained here do not support the ion transfer model

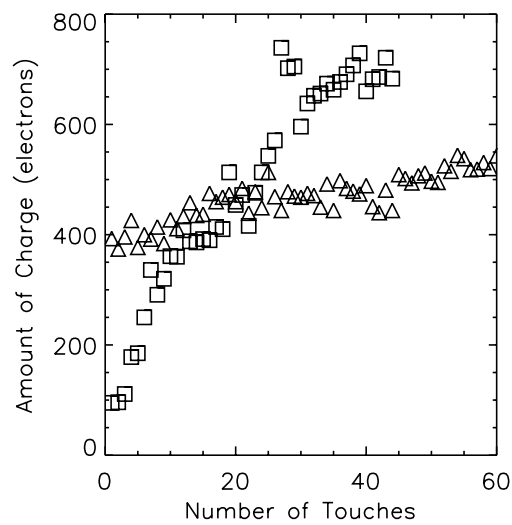


Figure 6.12

Contact electrification is observed for interactions between polystyrene and HOPG. Charge increases linearly with number of contacts between the sphere and substrate. Results for contact charging are shown for a  $3\ \mu\text{m}$  (triangles) and  $5\ \mu\text{m}$  (diamonds) radius polystyrene spheres. The rates at which charge increases are 2 electrons/contact and 14 electrons/contact.

for several reasons. First, the ionic model is inconsistent with the increase in charge as a function of contact to the HOPG substrate but not to Au. If ion transfer from the polystyrene sphere to the substrate is occurring, it should be observed for both substrates. Also, since the experiments are performed in a moderate vacuum environment after purging with dry nitrogen, the effect of an absorbed water layer is not a significant factor. If the assumption that the observed charging is due to ions distributed on the surface due to sample preparation, one might expect to measure a uniform charge distribution over the sphere. Such a charge distribution is not consistent with our force gradient measurements. It can be concluded that for the systems studied here, the transfer of ions between sphere and substrate is not significant.

To summarize, measurement of the force gradient for each system studied clearly shows a dramatic difference in the force gradient governing the sphere-substrate interaction. For the polystyrene-HOPG system, the behavior is dominated by a localized electrostatic force. Alternately, the polystyrene-Au system indicates a behavior dominated by a van der Waals interaction, with little contribution from charging. From these results, it is reasonable to conclude that the charging is consistent with electron transfer into trap states in the insulating polystyrene sphere upon contact with HOPG. Most of the states appear to fill upon initial contact with the substrate. Because the region of contact spans only a few hundred nanometers, neither the ion nor material transfer model can explain the amount of charge acquired. If charging occurred because of ions or material trans-

fer, one would expect charging to occur independently of the interacting materials. We observed, however, that charging occurs between the polystyrene sphere and HOPG substrate, but not between the polystyrene sphere and Au[111] film.

In conclusion, using AFM techniques to investigate the force of interaction between micrometer-size spheres and substrates, we have studied some fundamental processes related to triboelectrification. Such studies are useful because they provide further insight into the factors influencing adhesion of small particles to substrates. The techniques described are generally useful for further studies of frictional charging provided well characterized, micrometer-size objects of known shape and composition are used.

## 7. Summary

Micrometer-sized particles have been attached to atomic force microscope (AFM) cantilevers in order to measure the forces governing particle adhesion. Particle adhesion is of significant importance in a variety of fields ranging from medicine to electrophotography. Understanding the mechanisms responsible for these interactions is necessary in order to tune the properties of particle adhesion. The AFM provides a unique approach to understanding the forces which govern surface adhesion. It has been determined that the adhesion between such objects is significantly influenced by their material properties, size, and geometry. In particular, the interaction forces responsible for adhesion are found to be both van der Waals and electrostatic in origin. Prior, to the invention of the AFM, measuring the interaction forces between individual, micrometer-sized objects was not possible. Since the development of surface probe microscopy, there has been a tremendous growth in interest in studying the adhesion forces.

The two modes of operation developed (static and dynamic) have provided important information about the interaction forces for a dielectric sphere-conducting plane geometry. In this study, it was shown that the interaction forces are dominant over different ranges. A non-retarded van der Waals force is required to

explain the behavior of the interaction for separations of under 30nm. For larger separations, a localized electrostatic force is dominant. Prior to this investigation, no truly quantitative understanding was made of the actual forces governing the interaction between individual micrometer particles and flat surfaces. In recent years, many researchers have mounted small particles to AFM levers to measure interactions with materials in liquids, but no comprehensive study had been made in a moderate vacuum environment. In addition, there have been no measurements performed to determine the relative contributions to the interaction force between an individual particle and surface.

The AFM techniques which have been developed also provide a means to study contact electrification between individual micrometer particles and surfaces. While some work has been done investigating triboelectrification of bulk materials, there is no universal theory explaining charge transfer between all materials. The only interactions which are thoroughly understood are between metals. Measurements performed between polystyrene spheres and two surfaces (highly oriented pyrolytic graphite (HOPG) and Au[111]) are consistent with the electron transfer model for contact electrification. This gives further evidence of the validity of the AFM techniques.

In summary, the investigations performed on micrometer polystyrene spheres and flat surfaces have provided a further understanding of the mechanisms governing particle adhesion and contact electrification. It opens new avenues of research in the field of small particle adhesion. The techniques described provide a unique

method of measuring the adhesion between particles and surfaces, and the interaction forces which influence adhesion.

## BIBLIOGRAPHY

## BIBLIOGRAPHY

1. H.C. Hamaker, *Physica* **4** **58**, 1058 (1937).
2. E. M. Lifshitz, *JETP* **2**, 73 (1956).
3. D. Langbein, *J. Phys. Chem. Solids* **32**, 1657 (1971).
4. N. A. Burnham, R. J. Colton, and H. M. Pollock, *Phys. Rev. Lett.* **69**, 144 (1992).
5. B.V. Derjaguin, I.I. Abrikosova, and E.M. Lifshitz, *Quart. Rev. Chem. Soc. (London)* **10**, 295 (1956).
6. W. Black, J.G.V. De Jongh, T.G. Overbeek, and M.J. Sparnaay, *Trans. Far. Soc.* **56**, 1597 (1960).
7. S. Hunklinger, H. Geisselmann, and W. Arnold, *Rev. Sci. Instrum.* **43**, 584 (1972).
8. B.V. Derjaguin, *Kolloid Zeits* **69**, 155 (1934).
9. J.N. Israelachvili and D. Tabor, Van der waals forces: Theory and experiment, in *Progress in Surface and Membrane Science, Vol. 7*, edited by J.F. Danielli, M.D. Rosenberg, and D.A. Cadenhead, pages 2–53, Academic Press, New York, 1973.
10. I. E. Dzyaloshinskii, E. M. Lifshitz, and L. P. Pitaevskii, *JETP* **37**, 161 (1960).
11. U. Hartmann, *Phys. Rev. B* **42**, 1541 (1990).
12. B. V. Derjaguin, Y. I. Rabinovich, and N. V. Churaev, *Nature* **272**, 313 (1978).
13. J. N. Israelachvili and D. Tabor, *Proc. R. Soc. Lond. A.* **331**, 19 (1972).

14. W.A. Ducker, R.F. Cook, and D.R. Clarke, *J. Appl. Phys.* **67**, 4045 (1990).
15. F. London, *Trans. Faraday Soc.* **33**, 8 (1937).
16. H.B.G. Casimir and D. Polder, *Phys. Rev.* **73**, 360 (1948).
17. J.N. Israelachvili and D. Tabor, *Proc. R. Soc. London* **A311**, 19 (1972).
18. J.N. Israelachvili, *Intermolecular and Surface Forces, 2nd ed.*, Academic Press, San Diego, 1992.
19. J. Visser, *Surf. Colloid Sci.* **8**, 3 (1976).
20. K.L. Johnson, K. Kendall, and A.D. Roberts, *Proc. R. Soc. London* **A324**, 301 (1971).
21. D.M. Schaefer, M. Carpenter, B. Gady, R. Reifenberger, L.P. DeMejo, and D.S. Rimai, *J. Adhesion Sci. Technol.* **9**, 1049 (1995).
22. D. Schaefer, R. Reifenberger, and R.P. Andres, unpublished.
23. G. Binnig, C.F. Quate, and Ch. Gerber, *Phys. Rev. Lett.* **56**, 930 (1986).
24. D. Sarid, D. Iams, V. Weissenberger, and L.S. Bell, *Optics Letters* **13**, 12 (1988).
25. Y. Martin, C.C. Williams, and H.K. Wickramasinghe, *J. Appl. Phys.* **61**, 4723 (1987).
26. D. Rugar, H.J. Mamin, R. Erlandsson, J.E. Stern, and B.D. Terris, *Rev. Sci. Instrum.* **59**, 2337 (1988).
27. R. Erlandsson, J.E. Stern, B.D. Terris, H.J. Mamin, and D. Rugar, *Rev. Sci. Instrum.* **59**, 2337 (1988).
28. C. A. Putman, B. G. De Groot, N. F. Van Hulst, and J. Greve, *J. Appl. Phys.* **72**, 6 (1992).
29. J. E. Sader, *Rev. Sci. Instrum.* **66**, 4583 (1995).
30. J.P. Cleveland, S. Manne, D. Bocek, and P.K. Hansma, *Rev. Sci. Instrum.* **64**, 403 (1993).

31. C. B. Duke and T. J. Fabish, *Physical Review Letters* **37**, 1075 (1976).
32. J. Lowell and A.C. Rose-Innes, *Adv. Phys.* **29**, 947 (1980).
33. W. N. Reynolds, *Physical Properties of Graphite*, Elsevier Publishing Co. Ltd., 1968.
34. H. Zabel and S. A. Solin, *Graphite Intercalation Compounds II*, Springer-Verlag, 1992.
35. N. B. Brandt, *SEMIMETALS*, North-Holland Publishing Co., 1988.
36. Dror Sarid, *Scanning Force Microscopy*, Oxford University Press, 1991.
37. David M. Schaefer, PhD thesis, Purdue University, 1993.
38. Y. Martin, C.C. Williams, and Wickramasinghem H.K., *Journal of Applied Physics* **61**, 4723 (1987).
39. D.S. Rimai, L.P. DeMejo, and R.C. Bowen, *J. Appl. Phys.* **68**, 6234 (1990).
40. D. S. Rimai, L. P. DeMejo, W.B. Vreeland, R. C. Bowen, S.R. Gaboury, and M.W. Urban, *J. Appl. Phys.* **71**, 2253 (1992).
41. D.W. van Krevelen, *Properties of Polymers*, Elsevier, New York, 1976.
42. W.R. Smythe, *Static and Dynamic Electricity*, McGraw Hill, New York, 1939.
43. H. Krupp, *Adv. Colloid Interface Sci.* **3**, 137 (1972).
44. D. Rimai, private communication.
45. W.R. Harper, *Contact and Frictional Electrification*, Oxford Press, London, 1967.
46. Li-Huang Lee, *Fundamentals of Adhesion*, Plenum Press, 1992.
47. D. A. Hays, *J. Chem. Phys.* **61**, 1455 (1974).
48. J. H. Anderson, *Journal of Imaging Science and Technology* **38**, 378 (1994).
49. A. F. Diaz and D. Fenzel-Alexander, *Langmuir* **9**, 1009 (1993).

50. M. H. Davis, *American Journal of Physics* **37**, 26 (1969).
51. H. Bauser, *Dechema Monographs* **72**, 11 (1974).
52. C. B. Duke and T. J. Fabish, *Physical Review Letters* **37**, [A (1976)].
53. P. E. Shaw, *Proc. Phys. Soc.* **39**, 449 (1927).
54. D. K. Davies, *J. Phys. D* **2**, 1533 (1969).
55. W.A. Ducker, T.J. Senden, and R.M. Pashley, *Nature* **353**, 239 (1991).
56. W.A. Ducker, T.J. Senden, and R.M. Pashley, *Langmuir* **8**, 1831 (1992).
57. I. Larson, C.J. Drummond, D.Y.C. Chan, and F. Grieser, *J. Am. Chem. Soc.* **115**, 11885 (1993).
58. T.J. Senden and W. A. Ducker, *Langmuir* **10**, 1003 (1994).
59. S. Biggs and P. Mulvaney, *J. Chem. Phys.* **100**, 8501 (1994).
60. W.A. Ducker, Z. Xu, and J.N. Israelachvili, *Langmuir* **10**, 3279 (1994).
61. H-J. Butt, *J. Coll. Interface Sci.* **166**, 109 (1994).
62. S. Biggs, *Langmuir* **11**, 156 (1995).
63. I. Larson, C.J. Drummond, D.Y.C. Chan, and F. Grieser, *J. Phys. Chem.* **99**, 2114 (1995).
64. D.M. Schaefer, M. Carpenter, R. Reifenberger, L.P. DeMejo, and D.S. Rimai, *J. Adhesion Sci. Technol.* **8**, 197 (1994).
65. M.L. Ott and H.A. Mizes, *Colloids Surf. A* **87**, 245 (1994).
66. H.A. Mizes, *J. Adhesion Sci. Technol.* **8**, 937 ((1994)).
67. H.A. Mizes, Surface roughness and particle adhesion, in *Advances in Particle Adhesion*, edited by D.S. Rimai and L.H. Sharpe, pages 155–65, Gordon and Breach, The Netherlands, 1996.
68. B. Gady, D. Schleef, R. Reifenberger, L.P. DeMejo, and D.S. Rimai, *Phys. Rev. B* **53**, 8065 (1996).

69. B. Gady, R. Reifenberger, D.S. Rimai, and L.P. Demjo, *Langmuir* **XX**, (submitted) (1997).
70. D.A. Hays, Adhesion of charged particles, in *Fundamentals of Adhesion and Interfaces*, edited by D.S. Rimai, L.P. DeMejo, and K.L. Mittal, pages 61–71, VSP, Utrecht, 1995.
71. A. R. Ubbelohde and F. A. Lewis, *Graphite And Its Crystal Compounds*, Oxford University Press, 1960.

## APPENDICES

Appendix A: A sample of the C code which calculates the resonant frequency

peak of the cantilever.

```

#include <stdio.h>
#include <math.h>

int spec[10000];

double res(int *spec,int nspec,double *w0,double *q,double *g);
int getint(FILE *it);
int getshort(FILE *it);

double freq_start,freq_step,a,b;
void main(int argc,char **argv)
{
double w,w0,q,G,sig;
int tnum=-1;
int hys;
int i,j,nspec,mark,fnum=0;
char fn[20],s[100];
FILE *it;

i=1;
while(i<argc){
if(*argv[i]=='-')switch(argv[i][1]){
case 'c':
sscanf(argv[i+1],"%d",&tnum);
i+=2;
break;
default:
puts("unknown switch");
i++;
}
else fnum=i++;
}
if(!fnum){
printf("spec filename\n");
exit(0);
}
sprintf(fn,"%s.log",argv[fnum]);
it=fopen(fn,"r");
if(!it){
puts("cannot open log file");
exit(0);
}
fgets(s,100,it);

```

```

sscanf(s,"%lf",&a);
fgets(s,100,it);
sscanf(s,"%lf",&freq_start);
fgets(s,100,it);
sscanf(s,"%lf",&freq_step);
fgets(s,100,it);
sscanf(s,"%lf",&b);
#ifdef DEBUG
printf("%f %f %f %f\n",a,freq_start,freq_step,b);
#endif
fclose(it);
it=fopen(argv[fnum],"r");
if(!it){
puts("cannot open file");
exit(0);
}
freq_step=1.*freq_step;
j=0;
G=0.0;
while(!feof(it)){
mark=getint(it);
nspec=getint(it);
#ifdef DEBUG
printf("%d %d\n",mark,nspec);
#endif
hys=getint(it);
for(i=0;i<nspec;i++){
spec[i]=getshort(it)&0x7fff;
if(tnum<0 || tnum==j){
G=w0=q=0.0;
sig=res(spec,nspec,&w0,&q,&G);
if(tnum<0){
printf("%d %d %d %f %f %f %f\n",j,mark,hys,sig,w0,q,G);
}else{
for(i=0;i<nspec;i++){
w=freq_start+i*freq_step;
printf("%d %f\n",spec[i],G/
sqrt((w0*w0-w*w)*(w0*w0-w*w)+q*q*w*w));
}
}
}
j++;
}
fclose(it);
}

int getint(FILE *it)

```

```

{
int i;
i=(signed char)getc(it)*0x1000000;
i+=(unsigned char)getc(it)*0x10000;
i+=(unsigned char)getc(it)*0x100;
i+=(unsigned char)getc(it);
return i;
}

int getshort(FILE *it)
{
int i;
i=(signed char)getc(it)*0x100;
i+=(unsigned char)getc(it);
return i;
}

double res(int *spec,int nspec,double *w0,double *q,double *g)
{
double u,d,sig2,w;
double dw0,ddw0,sigw0,w02;
double dG,ddG,sigG;
double dq,ddq,sigq;
int do_g,i,j;
int max,nmax;

max=spec[nmax=0];
for(i=0;i<nspec;i++)if(max<spec[i]){
max=spec[i];
nmax=i;
}
if(!*w0){
/* rough estimate of w0 */
*w0=freq_start+freq_step*(nmax+0.5);
#ifdef DEBUG
printf("nmax: %f\n",*w0);
#endif
}
if(!*q){
/* rough estimate of q */
*q=0.5;
for(i=0;i<nspec;i++)if(spec[i]*2>max)(*q)+=0.5;
#ifdef DEBUG
printf("fwhm: %f\n",*q);
#endif
*q*=freq_step;
}
}

```

```

if(*g)do_g=0;
else{
do_g=1;
*g=max*(*w0)*(*q);
}

for(j=0;j<50;j++){
#ifdef DEBUG
printf("%2d: w0=%f G=%f q=%f\n",j,*w0,*g,*q);
#endif
w02=(*w0)*(*w0);
sig2=0;
dG=0;
ddG=0;
dw0=0;
ddw0=0;
dq=0;
ddq=0;
for(i=0;i<nspec;i++){
w=freq_start+i*freq_step;
u=sqrt((w02-w*w)*(w02-w*w)+(*q)*(*q)*w*w);
d=spec[i]-(*g)/u;
sig2+=d*d;
dG+=-2*d/u;
ddG+=2/u/u;
dw0+=4*(*g)*(*w0)*(w02-w*w)*d/u/u/u;
ddw0+=4*(*g)*(w02*(w02-w*w)*(w02-w*w)*(2*(*g)/u-6*d)/u/u+
d*(3*w02-w*w))/u/u/u;
dq+=2*(*g)*(*q)*w*w*d/u/u/u;
ddq+=2*(*g)*w*w*(((*g)*(*q)*(*q)*w*w)/u/u/u+
d*(1+3*(*q)*(*q)*w*w/u/u))/u/u/u;
}
sigG=-dG/ddG;
sigw0=-dw0/ddw0;
sigq=-dq/ddq;
if(do_g && ddG>0)(*g)+=sigG/2;
if(ddq>0)(*q)+=sigq/2;
if(ddw0>0)(*w0)+=sigw0/2;
}
return sqrt(sig2);
}

```

## Appendix B: Subroutine for collecting frequency spectra.

```

;*****
;      Frequency Analysis Program
;      B. Gady 10/17/94
;
;      Take spectrum data and display measured and fitted
;      frequency data.
;
;
;*****
;      Take matrix of data fro schleef's analysis and
;      Note that you get the individual spectra by running
; spec -c #
;filename
;print=1
print=2

if (print EQ 1 ) Then Begin
set_plot, 'x'
endif

if (print EQ 2) Then Begin
set_plot, 'ps'
output_file=''
READ,'Enter output file name: ',output_file
evice,xsize=15.0,xoffset=3.0,yoffset=3.0,$
bits_per_pixel=8,ysize=18.0,filename=output_file
endif

;*****
;      Reading in data file
;*****
Read,'Files to be read: ',num
num=fix(num)
for p=1,num do begin
size=500
a=fltarr(2,size)
displacement=fltarr(size)
dhys=fltarr(size)

filename=''
READ,'Enter Filename: ',filename
filename1=filename
OPENR,1,filename1
readf,1,a
a=transpose(a)

```

```

measure=a(*,0)
fit=a(*,1)
CLOSE,1
;*****
;   PLOT AMPLITUDE VS. POSITION
;*****
h=[77.1]
b=[77.2]
d=[.9]
e=[.85]

minfreq=
maxfreq=

initfreq=

stepfreq=6.181

freq=findgen(size)*1*stepfreq+initfreq
freq=freq/1000.0

if (p eq 1) then begin
maxfit=max(fit)
maxmeasure=max(measure)
endif

fit=fit/maxfit
measure=measure/maxmeasure

if (p eq 1) then begin
plot,freq,fit,xrange=[minfreq,maxfreq],yrange=[0,max(fit)],$
xtitle='!17 Frequency (kHz)',$
ytitle='!17 Amplitude (Normalized Units)', charsize=2
oplot,freq,measure,psym=p+4

;oplot,h,d,psym=p+4
;xyouts,b,d,'!17z!Do!N=100 nm',charsize=1.4
endif

if (p gt 1) then begin
oplot,freq,fit
oplot,freq,measure,psym=p+2
;oplot,h,e,psym=p+2
;xyouts,b,e,'!17z!Do!N=10 nm',charsize=1.4
endif

endfor

```

```
if (print eq 2) Then begin  
device,/close  
endif  
end
```

## Appendix C: Analysis code written in IDL.

```

;*****
; B. Gady 1/31/94
;
; Program modified for use in April95 file. Calculate
; and plot
; force gradient data from freq. spectra.
;
;*****
; Take matrix of data from schleef's v.c program and
; analyze force gradients.

;print=1
print=2

!x.thick=5.
!y.thick=5.

if (print EQ 1 ) Then Begin
set_plot, 'x'
endif

if (print EQ 2) Then Begin
set_plot, 'ps'
output_file=''
READ,'Enter output file name: ',output_file
device,xsize=18.0,xoffset=3.0,yoffset=3.0,$
bits_per_pixel=8,ysize=18.0,filename=output_file
endif

;*****
; Reading in data file
;*****
Read,'Files to be read: ',num
num=fix(num)
for p=1,num do begin

;*****
; Insert data set to analyze
;*****

;insert data file here....

if (p eq 1) then begin
size=34

```

```
filename="i920"
jump=7.5+1.5
spring=2.6
gain=10.
endif
if (p eq 2) then begin
size=32
filename="j920"
jump=7.5+1.5
spring=2.6
gain=10.
endif
if (p eq 3) then begin
size=27
filename="k920"
jump=7.5+1.5
spring=2.6
gain=10.
endif
if (p eq 2) then begin
size=28
filename="l920"
jump=7.5+1.5
spring=2.6
gain=10.
endif

if (p eq 1) then begin
size=29
filename="d920"
jump=9.
spring=2.6
gain=10.
endif

a=fltarr(7,size)
displacement=fltarr(size)
  filename1=filename+".out"
  OPENR,1,filename1
  readf,1,a
  a=transpose(a)
  point=a(*,0)
  position=a(*,1)
  hys=a(*,2)
  sigma=a(*,3)
```

```

osc=a(*,4)
damping=a(*,5)
driving=a(*,6)
CLOSE,1

;*****
; Declaration of variables
;*****
;A          Data Matrix array(7,size)
;BEST       Linear fit call for 1st data set
;COUL Log10 for coulomb fit - Array
;COULOMB Coulomb force gradient fit - Array
;DAMPING    Damping terms - Array
;DISPLACEMENT Log10 of predicted location value
;DRIVING    Driving forces - Array
;F          Log10 for freq - Array
;FILENAME   STRING    = 'c1013'
;FILENAME1  STRING    = 'c1013.out'
;FIRST      Best Slope for fit of 1st data set
;FREQ       Measured force gradient 1st set - Array
;FVC        Log10 fvdwc - Array
;FVDWC      Hamaker model for Cylinder gradient - Array
;FVDWS      Hamaker model for Sphere gradient - Array
;FVS        Log10 fvdws - Array
;G POLY_FIT of location and hysteresis data
;GAIN       Voltage gain applied to sample tube
;H1         Hamaker constant
;H2 Hamaker constant
;HYSTERYSIS Hysteresis 1st set (1/10) - Array
;I          dummy variable
;LOCATION     Predicted location (nm) 1st set - Array
;NUM        Number of data files to analyze
;OSCMAX     Maximum resonance frequency
;P          dummy variable
;POINT      Index of matrix elements 1st set - Array
;POSITION   Location in step units 1st set - Array
;RESDIFF    Difference in the squares of w0 and w(z) - Array
;RAD        Tip radius
;RESFREQ    Log10 of r 1st set - Array
;SIGMA
;SIZE       File length 1st set
;VDWGRAD    Measured force gradient calculated from freq. data
;YFIT POLY_FIT line to hysteresis data and location
;ZERO       Intercept on hysteresis displacement 1st set

;***** Initialize arrays and constants *****

```

```

h=0.9e-19
rad=4500.e-9
PI=3.1415926

best=fltarr(size-1)
fvdwc=fltarr(size)
fvdws=fltarr(size)
coul=fltarr(size)
coul2=fltarr(size)
patch=fltarr(size)
coulomb=fltarr(size)
coulomb2=fltarr(size)
deviation=fltarr(size)
displacement2=fltarr(size)
displacement=fltarr(size)
force=fltarr(size)
freq=fltarr(size)
g=fltarr(size)
yfit=fltarr(size)
vdwgrad=fltarr(size)
histy=fltarr(size)
spacing=fltarr(size)
uniform=fltarr(size)
;*****
; Main Program
;*****

location=gain*float(position)*4.65*10./32768.
hysteresis=.1*hys
hysty=5*(max(hysteresis)-hysteresis)
g=POLY_FIT(location,hysteresis,1,yfit)

;temporary fix for the multiplot routine
;oscmx=max(osc)
oscmx=77740

resdiff=spring*(1-(osc/oscmx)^2)
for i=0,size-1,1 do begin
if (resdiff(i) lt 0) then resdiff(i)=.1;
endfor
f=log10(freq)
resfreq=log10(resdiff)
vdwgrad=log10(resdiff)

zero=best(0)

```

```

first=best(1)
for i=0,size-1,1 do begin
deviation(i)=max(location)-location(i) +jump
endfor
displacement=deviation
;*****
; Coulomb model
;*****
;charge = localized region of charge at contact.
;q = uniform charge distribution over sphere.

q=04000*1.602e-19

charge=0300*1.602e-19
charge2=0540*1.602e-19
radeff=75.e-9
;radeff2=85.e-9

sig_u=q/(4.*PI*rad^2)
sig_p=charge/(4.*PI*radeff^2)
;sig_p2=charge2/(4.*PI*radeff2^2)

;*****uniform distribution of entire sphere*****
uniform=.5*(sig_u*4*PI*rad^2)^2*9e9/(deviation*1e-9+rad)^3

;*****localized distribution*****
patch=.5*charge^2*9e9/(deviation*1e-9+radeff)^3
;patch2=.5*charge2^2*9e9/(deviation*1e-9+radeff2)^3

coul=log10(uniform)
deviation=log10(deviation)
patchy=log10(patch)
;*****

for i=0,size-1,1 do begin
fvdws(i)=h*rad^1/(3*((max(location)-location(i)+jump)*1e-9)^3)
endfor

combo=fltarr(size)
combo2=fltarr(size)
combo3=fltarr(size)

combo=fvdws+patch-uniform
combo2=fvdws+patch
;combo3=fvdws+patch2

```

```

combo=alog10(combo)
combo2=alog10(combo2)
;combo3=alog10(combo3)

weff=fltarr(size)
weff=oscmax*sqrt(1-fvdws)
fvs=alog10(fvdws)
fvc=alog10(fvdwc)

;
;display variables
;
aa=[-.5]
bb=[-.8]
cc=[1.5]

if (p eq 1) then begin
plot,deviation,vdwgrad,xrange=[0.5,3.0],yrange=[-4.0,-0.0],$
psym=p+0, charthick=5.,charsize=2.,$
xtitle='!17Log!D1!N!D0!N of Separation Distance (nm)',$
ytittle='!17Log!D1!N!D0!Nk(1-!7x!E2!N/!7x!Do!N!E2!N)'
oplot,deviation,fvs,linestyle=6,thick=5.
;oplot,deviation,combo,linestyle=3,thick=5.
;oplot,deviation,patchy,linestyle=4
oplot,deviation,combo2,linestyle=2,thick=5.
;oplot,deviation,combo3,linestyle=5
;oplot,deviation,fvc-3.0,linestyle=4

;oplot,cc,aa,psym=1
;oplot,cc,bb,psym=2

endif

if (p gt 1) then begin
oplot,deviation,vdwgrad,psym=p
endif

endifor

if (print eq 2) Then begin
device,/close
endif
end

```

VITA

## VITA

Barrett Lee Gady was born on December 9, 1968 in Nogales, Mexico, the son of Howard and May Gady. He was raised in Kaneohe, Hawaii, and in San Diego, California. He graduated from Rochester Institute of Technology with a B.S. in physics and minors in Science and Technology Policy and Mandarin. He entered the physics program at Purdue University in 1991 and obtained a M.S. in physics in 1993. While at Purdue he married Wendy (Hanshaw) Gady.